Nanna Berre

Cut finite element methods for modeling excitable cells

Master's thesis in Applied Physics and Mathematics
Supervisor: André Massing
Co-supervisor: Marie E. Rognes
June 2022

Master's thesis

NTNU
Norwegian University of Science and Technology
Faculty of Information Technology and Electrical Engineering
Department of Mathematical Sciences

NTNU
Norwegian University of
Science and Technology

Nanna Berre

Cut finite element methods for modeling excitable cells

Master’s thesis in Applied Physics and Mathematics
Supervisor: André Massing
Co-supervisor: Marie E. Rognes
June 2022

Norwegian University of Science and Technology
Faculty of Information Technology and Electrical Engineering
Department of Mathematical Sciences

NTNU
Norwegian University of
Science and Technology

Abstract

The EMI (Extracellular-Membrane-Intracellular) model describes electrical activity in brain cells, where the extracellular and intracellular spaces and cellular membrane are explicitly represented. The model couples a system of partial differential equations (PDEs) in the intracellular and extracellular spaces with a system of ordinary differential equations (ODEs) on the membrane to describe the propagation of electrical potentials in brain cells. The PDE-ODE system is highly non-trivial and must be solved with numerical methods such as the finite element method. A key challenge for the EMI model is the generation of high-quality meshes conforming to the complex geometries of brain cells. A possible way to overcome this challenge is the cut finite element method (CutFEM), which allows the geometry to be represented independently of the computational domain.

In this thesis, we develop both theoretically and practically a novel CutFEM based discretization to solve the EMI model numerically. Starting from a Godunov splitting scheme, the EMI model is split into separate PDE and ODE parts. The resulting PDE part is a non-standard elliptic interface problem, for which we propose two novel CutFEM formulations. The first formulation, called the single-dimensional primal formulation, computes the intracellular and extracellular potential. We prove that this formulation satisfies condition number estimates and optimal a priori error estimates which are geometrically robust, i.e., insensitive to how the cell membrane geometry is embedded into the computational domain. The second formulation, called the multi-dimensional primal formulation, includes the electrical current across the membrane in addition to the potentials, leading to a saddle point problem. We show that after adding suitable stabilization terms, the formulation satisfies a geometrically robust inf-sup condition allowing us to establish an a priori error estimate for the discretization error of the electric membrane current and the extra/intracellular potentials. Next, we introduce a new unfitted discretization for the ODE part, which is based on a stabilized mass matrix approach and allows us to solve the membrane bound ODEs even if the membrane interface is not fitted to the computational domain. Finally, we perform extensive numerical studies that corroborate the theoretical results and demonstrate that CutFEM is a promising approach to efficiently simulate electrical activity in brain cells.

Sammendrag

EMI (Ekstracellulær-Membran-Intracellulær) modellen beskriver elektrisk aktivitet i hjerneceller, og representerer både de ekstracellulære og intracellulære områdene og cellemembranen eksplisitt. Modellen kobler et system av partielle differensiallikninger (PDE) på de intracellulære og ekstracellulære områdene med et system av ordinære differensiallikninger (ODE) på membranen for å beskrive forplantningen av elektrisk potensial i hjerneceller. PDE-ODE systemet er ikke-trivielt og må bli løst ved hjelp av numeriske metoder som f.eks. elementmetoden. En stor utfordring for EMI modellen er generering av høykvalitetsnett som skal tilsvare de kompliserte geometriene til hjerneceller. En mulighet for å løse denne utfordringen er ikke-romlige tilpassede elementmetoder, som f.eks CutFEM, som tillater at geometriene er representert uavhengig av beregningsdomenet.

I denne oppgaven foreslår vi en ny CutFEM basert diskretisering for å løse EMI modellen numerisk. EMI modellen er splittet i separate ODE og PDE problem ved hjelp av Godunov splitting. Det resulterende PDE problemet er et ikke-standard elliptisk grenseflateproblem som vi foreslår to nye CutFEM formuleringer for. Den første formuleringen, kalt den likedimensjonale primale formuleringen, beregner de intracellulære og ekstracellulære potensialene. Vi beviser at denne formuleringen oppfyller både kondisjonstallestimat og optimale a priori feilestimat som er geometrisk robuste, som betyr at de ikke er sensitive til hvordan membrangeometrien er plassert i beregningsdomenet. Den andre formuleringen, kalt den flerdimensjonale primale formuleringen, inkluderer strøm over cellemembranen i tillegg til de elektriske potensialene som fører til at den har samme form som et sadelpunktsproblem. Vi beviser at ved å legge til passende stabilisering tilfredsstiller denne formuleringen en geometrisk robust inf-sup betingelse som tillater oss å vise ett a priori feilestimat for diskretiseringsfeilen for strømmen over membranen og de ekstra/intracellulære potensialene. Etterpå introduserer vi en ny ikke-romlig tilpasset diskretisering for ODE problemet, som tillater ODE systemer å bli løst på membrangrenseflaten uten å tilpasse nettet. Til slutt utfører vi omfattende numeriske studier som underbygger de teoretiske resultatene og demonstrerer at CutFEM er en lovende metode for effektiv simulering av elektrisk aktivitet i hjerneceller.

Preface

This thesis is the concluding work on my M.Sc. degree in Applied Physics and Mathematics with a specialization in Industrial Mathematics at the Norwegian University of Science and Technology.

First and foremost, I would like to express my sincere gratitude to my supervisor André Massing. His excellent guidance, detailed feedback, and words of encouragement have been invaluable for this thesis. I am also grateful for his help in preparing my presentation for the ECCOMAS conference, making it a good experience. Secondly, I want to thank my co-supervisor Marie Rognes for introducing me to this exciting problem, for helpful input and comments, and for including me in the weekly EMIx meetings.

I also want to thank the wonderful group of friends I have spent the last five years with for making my time as a student so enjoyable. A special thanks to my flatmates Johanna, Marte, and Jonas for good company in lockdown and for all the support in stressful times. Finally, I would like to thank my parents for always being there, for never having tried to lead me in any direction, and for always believing in me.

Nanna Berre
Trondheim, June 2022

Contents

Sections with (*) are adapted from the project thesis with only minor changes.

Chapter 1

Introduction

The complex inner workings of the human brain are one of our biggest mysteries. In Norway, over 30% of the population will be affected by a brain-related disease [36], such as Alzheimer's and Parkinson's diseases. Mathematical simulation is a powerful tool that can lead to new discoveries about both the healthy and diseased brain. One of the main advantages of simulations is the reduced need for laboratory work and experimental animals. However, a substantial effort is still required to develop the models needed. Also, due to their complexity, most models for physiological processes can only be solved with numerical methods.

The field of computational electrophysiology saw its beginning in 1952 with the Hodgkin-Huxley model [37], which describes the action potential of a squid axon. Another important model in the field is the cable equation [54] for modeling electrical signals in neurons. One of the shortcomings in the cable equation is that the extracellular potential, meaning the potential of the space surrounding the cell, is assumed to be constant. A model used to find both intracellular and extracellular potentials in excitable tissue is the Bidomain model [58]. However, the Bidomain model homogenizes the tissue and does not specifically distinguish between the intracellular and extracellular space.

Increasing computational resources has made it possible to look at more detailed models, which can describe aspects missing in more homogenized models. By explicitly representing each cell, factors such as geometry, ephaptic coupling, and positioning of ion channels can be investigated [60]. In the Extracellular-Membrane-Intracellular (EMI) model [2,40,60] the extracellular domain (E), the membrane (M) and the intracellular domain (I) are explicitly represented. The model consists of a system of linear partial differential equations (PDEs) in the extracellular and intracellular domains coupled with a system of non-linear ordinary differential equations (ODEs) on the membrane.

The EMI model has been used to simulate monolayers of cardiac cells [60], cardiac conduction [39], arrhythmias [38], and to study heterogeneous distribution of ion channels [60]. In [61] the EMI model was compared to the cable equation for computations of neural potential. The EMI model has also been extended to the KNP-EMI model [24], which also

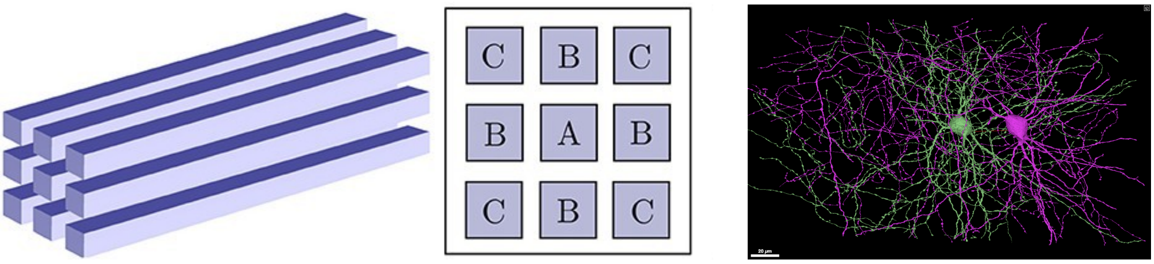

Figure 1: Illustration of the gap between available imaging techniques and geometries used for simulation. Rigth: Illustration of cellular domains used for ion dynamic simulations, figure from [24]. Left: Reconstructions of neural cells [59], figure from [46].

accounts for ion concentrations and electrodiffusion. One of the challenges for the model is the large need of computational resources, making simulations on organ scale a problematic task. All of the mentioned studies with the EMI model have used heavily idealized cell geometries, thus ignoring the possible effect the cell geometry can have on the solution. With imaging techniques able to create great reconstructions of neural cells [47, 59], a natural next step would be to solve the EMI model on more realistic domains. See Figure 1 for an example on the difference between geometries used in simulations and quality of reconstructions.

The finite element method (FEM) and the finite difference method (FDM) have been applied to solve the EMI model numerically [38, 39, 42, 60, 61], with FEM being preferred for complex geometries. However, a major challenge for FEM is creating high-quality 3D-meshes to represent complex domains. A way to overcome this challenge is the cut finite element method (CutFEM) [18], which allows the computational domain to be decoupled from the geometric representation of the physical domain. CutFEM has already successfully been applied to numerous problems, including elliptic interface problems [18], Stokes' problem [20], fluid interaction problems [44], and two-phase flow problems [52]. Recently, CutFEM has also been used to simulate astrocytic metabolism in realistic three-dimensional geometries [26, 27].

1.1 Contribution and outline

In this thesis, we will investigate the use of CutFEM to solve the EMI model. In [60], a Godunov splitting was applied to the EMI model, splitting the problem into separate PDE and ODE problems. For the PDE problem, four different finite element formulations were presented in [42], two referred to as the single-dimensional primal formulation and the multi-dimensional primal formulation. Based on these two, we propose both a novel CutFEM single-dimensional formulation and a novel CutFEM multi-dimensional formulation. The model's unfitted formulation leads to no nodes on the cell membrane, where the ODEs are defined. To overcome this problem, we introduce a new unfitted discretization of ODEs based on a stabilized mass matrix approach.

This thesis is organized as follows. In Chapter 2, the mathematical model is introduced. Next, Chapter 3 reviews Nitsche's method and CutFEM, with the Poisson boundary value problem and Poisson interface problem as model problems. Afterwards, Chapter 4 shows how the model is discretized in time by presenting the Godunov splitting for the EMI model, followed by time discretization for the PDE problem. Then, the unfitted discretization for the ODE system is developed by introducing an unfitted stabilized L^2-projection and utilizing this for the ODE system.

The time discretized PDE leads to a non-standard elliptic interface problem. In Chapter 5, we first review the classical single-dimensional primal formulation, which has intra- and extracellular potentials as unknowns. Then, we show well-posedness for the continuous formulation. Next, we propose the novel CutFEM single-dimensional formulation based on the classical formulation. Further, we derive optimal a priori error estimates for both formulations and show that the CutFEM formulation has geometrically robust condition numbers.

The multi-dimensional formulation was given by letting the electrical current over the membrane be an explicit unknown along with the electrical potentials. This formulation is reviewed in Chapter 6, where we show that it can be written as a penalized saddle point problem and use this to prove that the formulation is stable. Then, we propose the novel CutFEM multi-dimensional formulation, prove that it satisfies a discrete inf-sup condition, and establish an a priori error estimate.

Implementation and numerical studies are presented in Chapter 7. Here, we first corroborate the theoretical findings for the PDE formulation by numerical experiments on convergence and condition numbers. Next, we conduct numerical studies for the ODE step and the complete splitting scheme. Finally, Chapter 8 summarizes the final results along with directions for further work.

1.2 Relation to the project thesis

This master thesis is an expansion and continuation of the author's project thesis written in the fall of 2021. Chapters or sections that are taken from the project with only minor modifications are marked with an asterisk in both the title heading and the content list. In the project, the Godunov splitting with the CutFEM single-dimensional formulation and unfitted ODE discretization was presented. Section 2.2 and Chapters 3 and 4 are related to this and taken from the project. Chapter 5 contains the CutFEM single-dimensional formulation, which has been extended with analysis in this thesis. The experiments related to the ODE and the full splitting in Sections 7.5, 7.6, and 7.7 are from the project.

Chapter 2

Mathematical model

In this chapter, the EMI model is introduced. We begin by reviewing the derivation of the EMI model, before presenting the related membrane models we will use in this work. In addition, we give a short presentation of theoretical results for the model.

2.1 Derivation of the EMI model

In this section, we will give a derivation of the EMI model for a single cell, based on the presentations given in [40] and [1]. The derivation is based on two of Maxwell's equations, the Maxwell-Faraday equation

$$\nabla \times \mathbf{E} = \frac{\partial \mathbf{H}}{\partial t}, \tag{2.1}$$

and the Ampère-Maxwell law

$$\nabla \times \mathbf{H} = \mathbf{J} + \varepsilon \frac{\partial \mathbf{E}}{\partial t}, \tag{2.2}$$

where $\mathbf{E}$ is the electric field, $\mathbf{H}$ is the magnetic field, $\mathbf{J}$ is the density of free currents, and ε is the permittivity. It will be assumed that the following quasi-static approximation of (2.1) holds

$$\nabla \times \mathbf{E} = 0, \tag{2.3}$$

which is justified by the fact that the related magnetic parameters of the biological media make the influence of the magnetic field on the electric field negligible, as argued in [2]. Equation (2.3) gives that $\mathbf{E}$ is a conservative vector field, and can be written as

$$\mathbf{E} = -\nabla u, \tag{2.4}$$

where u is electrical potential.

2.1.1 Intracellular and extracellular domain

In the intracellular and extracellular domains, the derivation is based on the following quasi-static approximations also for (2.2)

$$\nabla \times \mathbf{H} = \mathbf{J}. \tag{2.5}$$

This approximation comes from the assumption that free unbalanced charges are instantly balanced, for more details see [2]. Recall that the divergence of the curl of any vector field is zero, $\nabla \cdot (\nabla \times \mathbf{H}) = 0$, which means that taking the divergence of (2.5) yields

$$\nabla \cdot \mathbf{J} = 0. \tag{2.6}$$

In addition, it is also assumed that Ohm's law

$$\mathbf{J} = \sigma \mathbf{E}, \tag{2.7}$$

holds in the extracellular and intracellular domain where σ is the conductivity of the considered medium. Now, combining (2.7) with (2.6) and (2.4) results in the Laplace equation,

$$\nabla \cdot \sigma \nabla u = 0.$$

Let σ_i, σ_e and u_i, u_e be the conductivity and electrical potentials for the intracellular(i) and extracellular(e) domain. Then, the following equations holds for each domain

$$\begin{aligned} -\nabla \cdot \sigma_i \nabla u_i &= 0 \quad \text{in } \Omega_i, \\ -\nabla \cdot \sigma_e \nabla u_e &= 0 \quad \text{in } \Omega_e. \end{aligned}$$

2.1.2 Membrane

On the membrane, the assumption that the free charges are balanced instantly is not valid, since charges may accumulate here. It is therefore necessary to work with (2.2), and not the quasi-static approximation. Taking the divergence of (2.2), yields

$$\nabla \cdot \mathbf{J} = -\nabla \cdot \varepsilon \frac{\partial \mathbf{E}}{\partial t}. \tag{2.8}$$

Next, consider a volume element B, and divide it into two parts, defined to be the intracellular and extracellular domains denoted as B_i and B_e, with the membrane separating the two parts denoted by Γ_B, as illustrated in Figure 2. Integrating (2.8) over B_i, and applying the divergence theorem yields

$$\int_{\partial B_i} \mathbf{J} \cdot \mathbf{n_{B_i}} \; \mathrm{d}S = -\int_{\partial B_i} \varepsilon \frac{\partial \mathbf{E}}{\partial t} \cdot \mathbf{n_{B_i}} \; \mathrm{d}S, \tag{2.9}$$

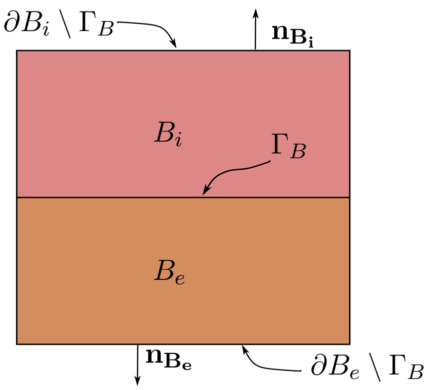

Figure 2: Illustration of the volume element, separated in the intracellular and extracllular part by the membrane, reconstructed from [40].

where $\mathbf{n_{B_i}}$ points outward from B_i. The boundary of the intracellular domain can now be split into two parts, the one coinciding with the boundary Γ_B and the remaining part $\partial B_i \setminus \Gamma_B$. Because of the quasi-static assumption in the intracellular domain, the right hand side of (2.9) can be written as

$$\int_{\partial B_i} \varepsilon \frac{\partial \mathbf{E}}{\partial t} \cdot \mathbf{n_{B_i}} \; \mathrm{d}S = \int_{\Gamma_B} \varepsilon_\Gamma \frac{\partial \mathbf{E}}{\partial t} \cdot \mathbf{n_{B_i}} \; \mathrm{d}S.$$

Further, the next assumption is that the membrane can be viewed as a capacitor consisting of two parallel plates separated by an insulator. The capacitance per area is given by $C_m = \varepsilon_T / d$, where d is the thickness of the membrane. Employing (2.4) yields that $\mathbf{E} \cdot \mathbf{n_{B_i}} = -\nabla u \cdot \mathbf{n_{B_i}}$. Now, defining the membrane potential

$$v = u_i - u_e,$$

together with the approximation $-\nabla u \cdot \mathbf{n_{B_i}} \approx v/d$, yields

$$\int_{\Gamma_B} \varepsilon_\Gamma \frac{\partial \mathbf{E}}{\partial t} \cdot \mathbf{n_{B_i}} \; \mathrm{d}S = \int_{\Gamma_B} C_m \frac{\partial v}{\partial t} \; \mathrm{d}S.$$

We now move on to the left hand side of (2.9). Define I_{ion} to be the flux of positive ions out the cell

$$\int_{\Gamma_B} \mathbf{J} \cdot \mathbf{n_{B_i}} \; \mathrm{d}S = \int_{\Gamma_B} I_{\text{ion}} \; \mathrm{d}S.$$

For the part of the boundary not coinciding with the cell membrane it has already been assumed that Ohm's law applies, meaning that

$$\int_{\partial B_i \setminus \Gamma_B} \mathbf{J} \cdot \mathbf{n_{B_i}} \; \mathrm{d}S = \int_{\partial B_i \setminus \Gamma_B} \sigma_i \mathbf{E} \cdot \mathbf{n_{B_i}} \; \mathrm{d}S.$$

Note that if the volume element being considered only consisted of the intracellular part, the equation would be the same. Assume therefore that we are considering only a volume element on the intracellular side shaped as a cylinder. As the height of the cylinder approaches zero, the boundary of the cylinder approaches the membrane. Therefore

$$\int_{\partial B_i \setminus \Gamma_B} \sigma_i \mathbf{E} \cdot \mathbf{n_{B_i}} \, dS. \approx \int_{\Gamma_B} \sigma_i \mathbf{E} \cdot \mathbf{n_{B_i}} \, \mathrm{d}S = -\int_{\Gamma_B} \sigma_i \nabla u_i \cdot \mathbf{n_{B_i}} \, \mathrm{d}S,$$

where in the last equality (2.4) was employed. Gathering, (2.9) can be written as

$$\int_{\Gamma_B} I_{\text{ion}} \, \mathrm{d}S - \int_{\Gamma_B} \sigma_i \nabla u_i \cdot \mathbf{n_{B_i}} \, \mathrm{d}S = -\int_{\Gamma_B} C_m \frac{\partial v}{\partial t} \, \mathrm{d}S.$$

Setting $\mathbf{n_{B_i}} = -\mathbf{n_i}$, and let $I_m = -\sigma_i \nabla u_i \cdot \mathbf{n_i}$ be the total current, the corresponding differential version is given by

$$I_m = C_m \frac{\partial v}{\partial t} + I_{\text{ion}}.$$

Repeating the same steps for the extracellular domain of the volume element gives

$$\int_{\Gamma_B} I_{\text{ion}} \, \mathrm{d}S + \int_{\Gamma_B} \sigma_e \nabla u_e \cdot \mathbf{n_{B_e}} \, \mathrm{d}S = \int_{\Gamma_B} C_m \frac{\partial v}{\partial t} \, \mathrm{d}S,$$

and by setting $\mathbf{n_i} = -\mathbf{n_e}$, we have that

$$\sigma_e \nabla u_e \cdot \mathbf{n_e} = C_m \frac{\partial v}{\partial t} + I_{\text{ion}}.$$

The last equation gives us the relation between the currents on the membrane,

$$\sigma_e \nabla u_e \cdot \mathbf{n_e} = -\sigma_i \nabla u_i \cdot \mathbf{n_i} = I_m.$$

2.1.3 The EMI model

In summary, the EMI model for a single cell, as illustrated in Figure 3, is given by the following equations,

$$\begin{aligned}
-\nabla \cdot \sigma_e \nabla u_e &= 0 && \text{in } \Omega_e, && (2.10a)\\
-\nabla \cdot \sigma_i \nabla u_i &= 0 && \text{in } \Omega_i, && (2.10b)\\
\sigma_e \nabla u_e \cdot \boldsymbol{n_e} &= -\sigma_i \nabla u_i \cdot \boldsymbol{n_i} \equiv I_m && \text{on } \Gamma, && (2.10c)\\
v &= u_i - u_e && \text{on } \Gamma, && (2.10d)\\
\frac{\partial v}{\partial t} &= \frac{1}{C_m}(I_m - I_{\text{ion}}) && \text{on } \Gamma. && (2.10e)
\end{aligned}$$

In addition, boundary conditions must be added. The model can also be extended to describe connected cells, see [40] for more information.

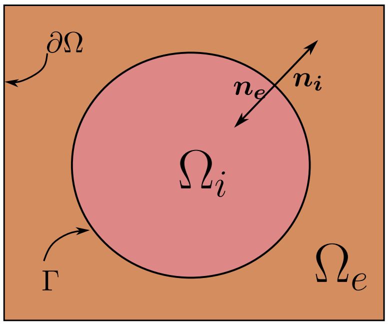

Figure 3: Illustration of the domains for a single cell EMI model.

2.2 Membrane models*

The ionic current density I_{ion} governs the membrane potential and is subject to further modeling. The change in the electrical potential corresponds to ions being transported in and out of the cell. Many mathematical models have been developed for modeling the membrane potential of excitable cells, and several hundred examples can be found in [23]. The simplest case to model is passive transportation of ions, which is only governed by concentration gradients and electrical fields. This is modeled with a passive model, driven only by potential differences between the intracellular and the extracellular domain. The passive membrane model is given by

$$I_{\text{ion}} = \frac{1}{R_m}(v - v_{rest}),$$

where R_m denotes the resistance, and v_{rest} denotes the resting potential of the membrane.

In more complicated models, change in the electrical potential also goes in the opposite direction of the electric fields. To consider such active models, replace equation (2.10e) with a system of the form

$$\begin{aligned} v_t &= \frac{1}{C_m}(I_m - I_{\text{ion}}(v, s)), \\ s_t &= F(v, s), \end{aligned}$$

where $v_t = \frac{\partial v}{\partial t}$. Here v is still the membrane potential, and s represent additional states, which can be ionic transportation or gating values. In this work, we will in addition to the passive model look at an active model known as the FitzHugh-Nagumo model [28]. In [55] a reparameterized version of the FitzHugh-Nagumo model is given as

$$v_t = \frac{c_1}{v_{amp}^2}(v - v_{rest})(v - v_{th})(v_{peak} - v) - \frac{c_2}{v_{amp}}(v - v_{rest})s + I_{app}, \tag{2.11a}$$

$$s_t = b(v - v_{rest} - c_3 s), \tag{2.11b}$$

Table 1: Parameters in the reparameterized FitzHugh-Nagumo model given in [55].

a	b	c_1	c_2	c_3
0.13	0.013	0.26	0.1	1

where the values for the parameters a, b, c_1, c_2, c_3 as described in [55] are listed in Table 1. Here, v_{rest} describes the resting potential, and v_{peak} describes the peak potential. Further the amplitude is given as $v_{amp} = v_{peak} - v_{rest}$, and the threshold potential is given as $v_{th} = v_{rest} + av_{amp}$. Finally, I_{app} describes applying a stimulus current. In this model, s describes a recovery variable without any physiological meaning.

2.3 Existence theory for the EMI model

Theoretical studies for EMI type of model can be found in [4,30,45,62]. In [4], well-posedness is discussed for an EMI system where the membrane model is assumed to be a function, i.e. $I_{\text{ion}}(v) = f(v)$. By assuming that $f \in W^{1,\infty}(\mathbb{R})$, $W^{s,p}$ being the standard Sobolev space, existence and uniqueness for a weak solution is proven. This is done first for f linear with results from abstract parabolic theory, before extending to a non-linear f by using a fixed-point technique.

In [45], another approach is taken to analyze the system with an ODE membrane model. They look at what is refereed to as the 3D cable model, which is similar to the EMI model only with Ω_e not bounded. A scaled version of the 3D cable model can be written as follows

$$\begin{aligned}
-\Delta v_e &= 0 && \text{in } \Omega_e, \\
-\Delta v_i &= 0 && \text{in } \Omega_i, \\
\sigma \nabla v_e \cdot \boldsymbol{n_e} &= -\nabla v_i \cdot \boldsymbol{n_i} \equiv I_m && \text{on } \Gamma, \\
v &= v_i - v_e && \text{on } \Gamma, \\
\frac{\partial v}{\partial t} &= (I_m - I_{\text{ion}}(v, s)) && \text{on } \Gamma, \\
\frac{\partial s}{\partial t} &= F(v, s) && \text{on } \Gamma, \\
v_e(x) &\to 0 && \text{as } |x| \to \infty.
\end{aligned} \tag{2.12}$$

The first step in [45] is to look at the following interface problem,

$$\begin{aligned}
-\Delta u_e &= 0 && \text{in } \Omega_e,\\
-\Delta u_i &= 0 && \text{in } \Omega_i,\\
\sigma\nabla u_e \cdot \boldsymbol{n_e} = -\nabla u_i \cdot \boldsymbol{n_i} &\equiv I_m && \text{on } \Gamma,\\
u &= u_i - u_e && \text{on } \Gamma,\\
u_e(x) &\to 0 && \text{as} |x| \to \infty,
\end{aligned}$$

and argue that a unique solution (u_i, u_e) exists for a reasonably regular u. Based on the interface problem, an operator Λ can be defined,

$$\Lambda_\sigma u \equiv \sigma\nabla u_e \cdot \boldsymbol{n_e} = -\nabla u_i \cdot \boldsymbol{n_i},$$

known as the Dirichlet-Neumann map for the domain Ω_i. With this operator, (2.12) can be expressed as a system of equations only on Γ,

$$\begin{aligned}
\frac{\partial v}{\partial t} &= (\Lambda_\sigma v - I_{\text{ion}}(v,s)) && \text{on } \Gamma,\\
\frac{\partial s}{\partial t} &= F(v,s) && \text{on } \Gamma.
\end{aligned}$$

An analysis based on semigroup properties then follows, and a global existence result for the model coupled with a FitzHugh-Nagumo type of system is proven.

Theorem 2.1 ([45], Corollary 6.8)**.** *The 3d cable model* (2.12) *coupled with a FitzHugh-Nagumo system has a global solution for any initial data* $U_0 \in X^2$*. For* $X = W^{s,p}(\Gamma), s > 2/p$*, the solution is classical. Moreover, there are positive constants* M_v *and* M_s *such that*

$$\|v(t)\|_{C(\Gamma)} \leqslant M_v, \quad \|s(t)\|_{C(\Gamma)} \leqslant M_s.$$

In the theorem above, $C(\Gamma)$ is the space of continuous functions on Γ. A similar result is also proven for Hodgkin-Huxley type systems in [45].

Chapter 3

Methods for spatial discretization of PDEs*

In this chapter, we review numerical methods for the discretization of PDEs in space. We start by introducing Nitsche's method for the Poisson boundary value problem and the Poisson interface problem. Nitsche's method is an optimally convergent method that incorporates Dirichlet boundary and interface conditions weakly into the bilinear and linear forms instead of strongly into the discrete function spaces. Next, we review the cut finite element method (CutFEM) and explain how the idea of weak imposition of boundary and interface conditions can be exploited to discretize the Poisson-type problems using meshes that do not fit the domain geometry.

3.1 Nitsche's method for the Poisson boundary value problem

In this section, we introduce Nitsche's method [49] for weak handling of boundary conditions. Following the presentation in [35], we use the Poisson problem with Dirichlet boundary conditions as a model problem. We start by giving a short recap of the standard weak formulation for the problem in order to introduce some notation and variables.

The strong form of the Poisson problem over a domain Ω is given as: find u such that

$$-\Delta u = f \qquad \text{in } \Omega, \tag{3.1a}$$

$$u = g \qquad \text{on } \Gamma, \tag{3.1b}$$

where $\Gamma = \partial\Omega$ denotes the boundary of the domain, and f and g are given functions. To derive the weak formulation of the problem, we begin by multiplying (3.1a) with a test function v in a suitable test space V and use integration by parts. This yields

$$(\nabla u, \nabla v)_\Omega - (\partial_n u, v)_\Gamma = (f, v)_\Omega, \tag{3.2}$$

where $(\cdot,\cdot)_\Omega$ denotes the L^2-inner product over the domain Ω, and $(\cdot,\cdot)_\Gamma$ denotes the L^2-inner product over a surface Γ. The L^2-norm will be denoted by $\|v\|_\Omega^2 := (v, v)_\Omega$. Let α

be a multi-index and let $D^\alpha v$ denote the weak derivative of order α. The Sobolev space $H^m(\Omega)$ is given as

$$H^m(\Omega) = \{v \in L(\Omega) : D^\alpha v \in L^2(\Omega) \text{ for } |\alpha| \leqslant m\},$$

and the corresponding Sobolev norm and seminorm will be denoted respectively by

$$\|v\|^2_{m,\Omega} = \|v\|^2_{H^m(\Omega)} = \sum_{\alpha \leqslant m} (D^\alpha v, D^\alpha v)_\Omega, \qquad |v|^2_{m,\Omega} = \sum_{\alpha = m} (D^\alpha v, D^\alpha v)_\Omega,$$

for integer $m \geqslant 1$. Define also the constrained space $H^m_g(\Omega) = \{v \in H^m(\Omega) : v = g \text{ on } \Gamma\}$. Now let the test space be $V_0 = H^1_0(\Omega)$, and the trial space be $V_g = H^1_g(\Omega)$. From this, the boundary conditions are incorporated in the definition of the trial space. The standard weak formulation is given as: find $u \in V_g$ such that

$$a(u, v) = l(v) \quad \forall v \in V_0,$$

where the bilinear form $a\colon V_g \times V_0 \to \mathbb{R}$, and the linear form $l\colon V_0 \to \mathbb{R}$ are given as

$$\begin{aligned} a(u, v) &= (\nabla u, \nabla v)_\Omega, \\ l(v) &= (f, v)_\Omega. \end{aligned}$$

Now we turn to present Nitsche's method as an alternative for incorporating Dirichlet boundary conditions by incorporating the boundary conditions through the weak formulation. Let both the test space and the solution space be $V = H^2(\Omega)$. Notice that we do not incorporate any restrictions on the solution through the function space. To discretize the problem, begin by letting $\mathcal{T}_h$ be a finite element partitioning of the domain Ω into simplex elements T. The diameter of an element T is denoted by $h_T = \operatorname{diam} T$, and define $h = \max_{T \in \mathcal{T}_h} h_T$. Let the space of polynomials of degree k on an element $T \in \mathcal{T}_h$ be denoted by $\mathbb{P}_k(T)$, and let $\mathbb{P}_k(\mathcal{T}_h) = \bigoplus_{T \in \mathcal{T}_h} \mathbb{P}_k(T)$. Further, let the space of piecewise continuous polynomials of degree k be denoted by

$$\mathbb{P}^c_k(\mathcal{T}_h) = \mathbb{P}_k(\mathcal{T}_h) \cap C^0(\Omega),$$

and define the discrete function space $V_h = \mathbb{P}^c_k(\mathcal{T}_h)$.

The weak formulation (3.2) is not a symmetric bilinear form, but can be symmetrized by adding the term $-(u - g, \partial_n v)_\Gamma$, yielding

$$(\nabla u, \nabla v)_\Omega - (\partial_n u, v)_\Gamma - (u, \partial_n v)_\Gamma = (f, v)_\Omega - (g, v)_\Gamma. \tag{3.3}$$

The formulation should also satisfy the Lax-Milgram lemma, and therefore needs to be coercive. This is obtained by adding a stabilization term, $\gamma h^{-1}(u - g, v)_\Gamma$, where γ is a positive parameter. The resulting bilinear form a_h and linear form l_h are then given as

$$a_h(u, v) = (\nabla u, \nabla v)_\Omega - (\partial_n u, v)_\Gamma - (u, \partial_n v)_\Gamma + (\gamma h^{-1} u, v)_\Gamma, \tag{3.4a}$$

$$l_h(v) = (f, v)_\Omega - (g, v)_\Gamma + (\gamma h^{-1} g, v)_\Gamma. \tag{3.4b}$$

The discrete weak formulation is given as: find $u_h \in V_h$ such that

$$a_h(u_h, v) = l_h(v) \quad \forall v \in V_h. \tag{3.5}$$

Notice that both of the added terms will vanish for the true solution, and therefore the formulation is consistent with the original problem (3.1).

To show that the variational formulation is coercive and bounded, the following two mesh dependent norms are needed

$$\begin{aligned} \|v\|_{a_h}^2 &:= \|\nabla v\|_\Omega^2 + \|h^{-\frac{1}{2}} v\|_\Gamma^2, \\ \|v\|_{a_h,*}^2 &:= \|v\|_{a_h}^2 + \|h^{\frac{1}{2}} \partial_n v\|_\Gamma^2. \end{aligned}$$

Also, let the notation $\alpha \lesssim \beta$ mean that there is some constant $C > 0$ such that $\alpha \leqslant C\beta$. The following stability results are given and proven in [35].

Proposition 3.1 (Discrete coercivity). *Let γ be positive and sufficiently large. Then the bilinear form a_h is discretely coercive, that is*

$$a_h(v, v) \gtrsim \|v\|_{a_h}^2 \quad \forall v \in V_h.$$

Proposition 3.2 (Boundedness). *For $u \in V_h \oplus V$ and $v \in V_h$ the bilinear form a_h satisfies*

$$a_h(u, v) \lesssim \|u\|_{a_h,*} \|v\|_{a_h}.$$

An important note about the discrete coercivity result is that the following inverse estimate is essential to the proof.

Proposition 3.3 (Inverse estimate). *There is a constant C independent of h such that*

$$\|h^{\frac{1}{2}} \partial_n v\|_{L^2(\Gamma)}^2 \leq C \|\nabla v\|_\Omega^2 \quad \textit{for all } v \in V_h. \tag{3.6}$$

The proof of the inverse estimate can be found in [57], where also the following a priori error estimate is given.

Theorem 3.4 (A priori error estimate). *Let $u \in H^s(\Omega)$, $s \geqslant 2$ be the solution of* (3.1) *and let $u_h \in V_h$ be the solution of* (3.5). *Then with $r = \min\{s, k+1\}$ the error $u - u_h$ satisfies*

$$\|u - u_h\|_{a_h} \lesssim h^{r-1} \|u\|_{r,\Omega},$$

and

$$\|u - u_h\|_\Omega \lesssim h^r \|u\|_{r,\Omega}.$$

Functions in the discrete finite element space V_h can be written as a linear combination, $v = \sum_{i=1}^N V_i \phi_i$ where $V = \{V_i\}_{i=1}^N \in \mathbb{R}^N$ are the coefficients and $\{\phi_i\}_{i=1}^N$ are the basis functions of V_h. The stiffness matrix $\mathcal{A}$ based on the discrete form a_h is defined by the relation

$$(\mathcal{A}V, W)_{\mathbb{R}^N} = a_h(v, w) \quad \forall v, w \in V_h.$$

The condition number of the stiffness matrix is defined by

$$\kappa(\mathcal{A}) = \|\mathcal{A}\|_{\mathbb{R}^N} \|\mathcal{A}^{-1}\|_{\mathbb{R}^N},$$

with the corresponding norm defined by

$$\|\mathcal{A}\|_{\mathbb{R}^N} = \sup_{v \in \mathbb{R}^n \setminus \mathbf{0}} \frac{\|\mathcal{A}V\|_{\mathbb{R}^N}}{\|V\|_{\mathbb{R}^N}}.$$

The estimate of how the condition number scales can now be given.

Theorem 3.5 (Condition number estimate)**.** *The condition number of the stiffness matrix associated with the bilinear form a_h* (3.4a) *satisfies the estimate*

$$\kappa(A) \lesssim h^{-2}.$$

The proof can be found in [35].

3.2 Nitsche's method for the Poisson interface problem

In this section, we present how Nitsche's method can be used to handle interface conditions, following the same procedure as in the previous section. Consider now the Poisson interface problem in a domain consisting of two non-overlapping subdomains Ω_1 and Ω_2, such that $\Omega = \Omega_1 \cup \Omega_2$. The subdomains are separated by an interface $\Gamma = \partial\Omega_1 \cap \partial\Omega_2$, and we consider a situation where Ω_1 is inside Ω_2, i.e. such that $\partial\Omega \cap \partial\Omega_1 = \emptyset$. A function v in Ω is now considered as a composition $v = (v_1, v_2)$ where $v_i = v|_{\Omega_i}$. The broken norm of v will be denoted as $\|v\|^2_{\Omega_1 \cup \Omega_2} = \|v_1\|^2_{\Omega_1} + \|v_2\|^2_{\Omega_2}$.

The strong form of the Poisson interface problem is given as: find u such that

$$\begin{aligned} -\nabla \cdot (\sigma \nabla u) &= f && \text{in } \Omega, && (3.7a)\\ u &= g && \text{on } \partial\Omega, && (3.7b)\\ [u] &= g_D && \text{on } \Gamma, && (3.7c)\\ [\sigma \partial_n u] &= g_N && \text{on } \Gamma. && (3.7d) \end{aligned}$$

We assume the diffusion coefficients σ_i to be constant for $i = 1, 2$, and the jumps across Γ are defined by

$$[u] = u_1|_\Gamma - u_2|_\Gamma \qquad [\sigma \partial_n u] = \sigma_1 \nabla u_1 \cdot \mathbf{n} - \sigma_2 \nabla u_2 \cdot \mathbf{n},$$

where we have defined the interface normal $\mathbf{n}$ as pointing outwards with respect to Ω_1. Also, the average is defined by

$$\{v\} = \frac{1}{2} v_1 + \frac{1}{2} v_2.$$

As in the previous section the weak formulation is derived by first multiplying (3.7a) with a test function $v \in V$ and using integration by parts, where $V = V_1 \times V_2$ and $V_1 = H^1(\Omega)$, $V_2 = \{v \in H^1(\Omega) : v|_{\partial\Omega} = g\}$. With the use of the identity $[ab] = \{a\}[b] + [a]\{b\}$, this yields

$$(\sigma \nabla u, \nabla v)_\Omega - ([v], \{\partial_n u\})_\Gamma = (f, v)_\Omega + (\{v\}, g_n)_\Gamma.$$

To discretize the problem, let $\mathcal{T}_h$ be a conformal mesh of Ω consisting of the two non-overlapping meshes $\mathcal{T}_{h,1}$ and $\mathcal{T}_{h,2}$, where $\mathcal{T}_{h,i}$ is defined as simplex-based triangulations of the domain Ω_i. Γ is formed by the facets in the interface between $\mathcal{T}_{h,1}$ and $\mathcal{T}_{h,2}$. The discrete functions spaces are given as

$$V_{h,1} = \mathbb{P}_k^c(\mathcal{T}_{h,1}), \quad V_{h,2} = \{v \in \mathbb{P}_k^c(\mathcal{T}_{h,2}) : v|_{\partial\Omega} = g)\},$$

and $V_h = V_{h,1} \times V_{h,2}$. Terms for symmetry and stabilization are added to arrive at the weak formulation for the Poisson interface problem: find $u_h \in V_h$ such that

$$a_h(u_h, v) = l_h(v) \quad \forall v \in V_h, \tag{3.8}$$

where the bilinear and linear forms are given as

$$a_h(u, v) = \sum_{i=1}^{2} (\sigma_i \nabla u_i, \nabla v_i)_{\Omega_i} - ([v], \{\partial_n u\})_\Gamma - ([u], \{\partial_n v\})_\Gamma + \gamma h^{-1}([u], [v])_\Gamma, \tag{3.9}$$

$$l_h(v) = \sum_{i=1}^{2} (f, v_i)_{\Omega_i} + (\{v\}, g_n)_\Gamma - (g_D, \{\partial_n v\})_\Gamma + \gamma h^{-1}(g_D, [v])_\Gamma. \tag{3.10}$$

As in the previous section, define mesh dependent norms

$$\|v\|_{a_h}^2 := \|\nabla v\|_{\Omega_1 \cup \Omega_2}^2 + \|h^{-\frac{1}{2}}[v]\|_\Gamma^2,$$
$$\|v\|_{a_h,*}^2 := \|v\|_{a_h}^2 + \|h^{\frac{1}{2}}[\partial_n v]\|_\Gamma^2.$$

We can now state a coercivity result and an a priori error estimate from [9].

Proposition 3.6 (Discrete coercivity). *Let γ be positive and sufficiently large. Then we have*

$$a_h(v, v) \gtrsim \|v\|_{a_h}^2 \quad \forall v \in V_h.$$

Theorem 3.7. *Let γ be positive and sufficiently large. Let $u \in H^s(\Omega_1) \times H^s(\Omega_2)$, $s \geqslant 2$ be the solution of* (3.7) *and let $u_h \in V_h$ be the solution of* (3.8). *Then with $r = \min\{s, k+1\}$ the error $u - u_h$ satisfies*

$$\|u - u_h\|_{a_h,*} \lesssim h^{r-1} \|u\|_{r,\Omega_1 \cup \Omega_2}.$$

Both proofs can be found in [9].

3.3 Cut finite element formulation of the Poisson boundary problem

In this section, we present the cut finite element (CutFEM) formulation of the Poisson boundary problem, following the presentation given in [33]. We build on the weak formulation stated in Section 3.1 using Nitsche's method. With Nitsche's method, we needed the mesh to be fitted to the domain of the problem. CutFEM allows us to have a mesh that is not consistent with the domain, a so-called unfitted mesh.

We begin by describing the discretization of Ω. Let $\widetilde{\mathcal{T}}_h$ be a background mesh covering $\bar{\Omega}$. Then, let the active background mesh $\mathcal{T}_h$ be defined by those elements $T \in \widetilde{\mathcal{T}}_h$ which intersect the interior $\Omega^o = \Omega \setminus \Gamma$,

$$\mathcal{T}_h = \{T \in \widetilde{\mathcal{T}}_h | T \cap \Omega^o \neq \emptyset\}.$$

The set of interior faces is defined by

$$\mathcal{F}_h = \{F = T^+ \cap T^- | T^+, T^- \in \mathcal{T}_h\}.$$

Also, the set of ghost penalty faces $\mathcal{F}_h^g$, is defined as the set of interior faces in the active mesh belonging to elements which are intersected by the boundary Γ,

$$\mathcal{F}_h^g = \{F \in \mathcal{F}_h : T^+ \cap \Gamma \neq \emptyset \vee T^- \cap \Gamma \neq \emptyset\}.$$

The ghost penalty faces are shown in dashed lines in Figure 4 (middle). The jump across an interior face $F \in \mathcal{F}_h$ is defined by

$$[w]|_F = w_F^+ - w_F^-,$$

where $w(x)^{\pm} = \lim_{t\to 0} w(x + t\mathbf{n})$ for some chosen unit norm on the face F. The discrete function space is now defined on the whole active mesh as the broken polynomial space of order k as $V_h = \mathbb{P}_k^c(\mathcal{T}_h)$.

Remember the linear and bilinear forms (3.4), derived with Nitsche's method. Recall that to prove that the bilinear form was coercive, the inverse estimate (3.6) was needed. In the unfitted case, the same estimate can not be given, as the constant C would depend on how the boundary cuts the elements. To remedy this, adding a stabilization parameter g_h, referred to as the ghost penalty was proposed in [16]. Adding the ghost penalty yields the CutFEM formulation for the problem: find $u_h \in V_h$ such that

$$A_h(u_h, v) := a_h(u_h, v) + g_h(u_h, v) = l_h(v) \quad \forall v \in V_h. \tag{3.11}$$

3.4 The role of the ghost penalty

As stated above, there is no inverse estimate to help show coercivity in norms defined on only the physical mesh. Instead, [33] introduces mesh dependent discrete norms, which are defined over the whole active mesh. For $v \in V_h$ define

$$\begin{aligned} \|v\|_{a_h}^2 &= \|\nabla v\|_\Omega^2 + \|h^{-\frac{1}{2}} v\|_\Gamma^2, \\ |v|_{g_h}^2 &= g_h(v, v), \\ \|v\|_{A_h}^2 &= \|v\|_{a_h}^2 + |v|_{g_h}^2. \end{aligned}$$

For $v \in H^2(\mathcal{T}_h) + V_h$ define

$$\|v\|_{a_h,*}^2 = \|v\|_{a_h}^2 + \|h^{\frac{1}{2}} \partial_n v\|_\Gamma^2.$$

By adding the ghost penalty, the bilinear form is augmented such that the discrete norms on the entire background mesh can be controlled. A common realization for the ghost penalty is to penalize the facet jump for all order derivatives over the ghost penalty facets [33]. This facet jump ghost penalty is for a set of positive parameters $\{\gamma_j\}_{j=0}^k$ given as

$$g_h(v, w) = \sum_{j=0}^{k} \sum_{F \in \mathcal{F}_h^g} \gamma_j h_F^{2j-1} ([\partial_n^j v], [\partial_n^j w])_F. \tag{3.12}$$

We now summarize results from [33] which shows that the CutFEM formulation (3.11) is stable and establishes an a priori estimate.

Proposition 3.8 (Discrete coercivity and stability [33])**.** *The discrete form A_h is coercive and stable with respect to the discrete energy norm $\|\cdot\|_{A_h}$, that is*

$$\begin{aligned} A_h(v, v) &\gtrsim \|v\|_{A_h}^2 & &\forall v \in V_h, \\ A_h(u, v) &\lesssim \|u\|_{A_h} \|v\|_{A_h} & &\forall u, v \in V_h, \end{aligned}$$

whenever γ is chosen large enough. Moreover, for $v \in H^2(\mathcal{T}_h) + V_h$ and $w \in V_h$, the discrete form a_h satisfies

$$a_h(u, v) \lesssim \|u\|_{a_h,*} \|v\|_{A_h}.$$

All the hidden constants depend only on the dimension d, the polynomial order k, the shape regularity of $\mathcal{T}_h$, and the curvature of Γ, but not on the particular cut configurations.

Theorem 3.9 (A Priori Error Estimate [33]). *Let $u \in H^s(\Omega)$, $s \geqslant 2$ be the solution to* (3.1) *and let $u_h \in V_h$ be the solution to the discrete formulation* (3.11). *Then with $r = \min\{s, k+1\}$ the error $u - u_h$ satisfies*

$$\begin{aligned} \|u - u_h\|_{a_h,*} &\lesssim h^{r-1}\|u\|_{r.\Omega}, \\ \|u - u_h\|_{\Omega} &\lesssim h^r\|u\|_{r,\Omega}. \end{aligned}$$

Another result in [33], shows that the CutFEM formulation has geometrically robust condition numbers, meaning that the condition number is not affected by how the boundary cuts the elements.

Theorem 3.10 (Condition number estimate [33]). *The condition number of the stiffness matrix associated with the bilinear form A_h* (3.11) *satisfies the estimate*

$$\kappa(A) \lesssim h^{-2},$$

where the hidden constant depends only on the dimension d, the polynomial order k, and the quasi-uniformity of $\mathcal{T}_h$ but not on the particular cut formulation.

3.5 Cut finite element formulation of the Poisson interface problem

We now formulate a CutFEM formulation for the interface Poisson problem (3.7). As with the Poisson boundary problem, assume that Ω is covered by a background mesh $\widetilde{\mathcal{T}}_h$. Define an active background mesh for each of the two subdomains

$$\mathcal{T}_{h,i} = \{T \in \widetilde{\mathcal{T}}_h | T \cap \Omega_i^{\circ} \neq \emptyset\},$$

and let $\mathcal{F}_{h,i}$ be the faces belonging to $\mathcal{T}_{h,i}$. The computational domains and meshes are shown in Figure 4, notice that these are now overlapping. The test spaces are defined by

$$V_{h,1} = \mathbb{P}_k^c(\mathcal{T}_{h,1}), \quad V_{h,2} = \{v \in \mathbb{P}_k^c(\mathcal{T}_{h,2}) : v|_{\partial\Omega} = g\},$$

and the total approximation space as $V_h = V_{h,1} \times V_{h,2}$. Recall the bilinear form a_h (3.9) and linear form l_h (3.10) from using Nitsche's method. An interface CutFEM formulation for the problem can be defined as: find $u_h = (u_{h,1}, u_{h,2}) \in V_h$ such that

$$A_h(u_h, v) := a_h(u_h, v) + g_h(u_h, v) = l_h(v), \tag{3.13}$$

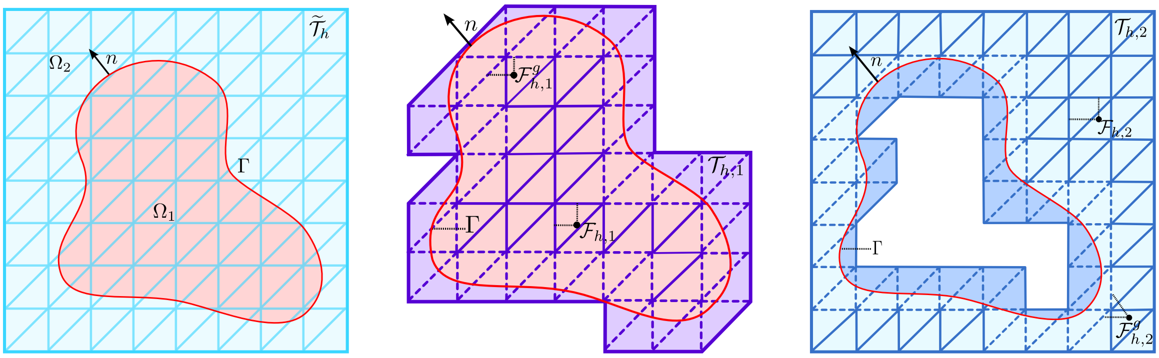

Figure 4: Illustration of the computational domain for the interface problem, taken from [33] with permission from the authors. (Left) Background mesh covering Ω. (Middle) The active mesh $\mathcal{T}_{h,1}$ for Ω_1 with internal faces $\mathcal{F}_{h,1}$ and ghost penalty faces $\mathcal{F}^g_{h,1}$ in dotted lines. (Right) Corresponding mesh and faces for Ω_2.

for all $v = (v_1, v_2) \in V_h$. Corresponding discrete norms are now defined for $v \in V_h$ as

$$\begin{aligned}\|v\|^2_{a_h} &= \|\nabla v\|^2_{\mathcal{T}_h} + \|h^{-\frac{1}{2}}[v]\|^2_{\Gamma},\\ \|v\|^2_{A_h} &= \|v\|^2_{a_h} + |v|^2_{g_h}.\end{aligned}$$

Let the ghost penalty for $u_h, v_h \in V_h$ be

$$g_h(u_h, v_h) = \sum_{i=1}^{2} g_{h,i}(u_{h,i}, v_{h,i}).$$

By again letting $g_{h,1}$ and $g_{h,2}$ be the facet jump ghost penalty as defined in (3.12), discrete coercivity and a priori estimate can be established, see e.g. [33], which we summarize next.

Proposition 3.11 (Discrete coercivity [33]). *It holds that*

$$\|v\|^2_{A_h} \lesssim A_h(v, v) \quad \forall v \in V_h.$$

Theorem 3.12 (A priori error estimate [33]). *Let $u \in H^s(\Omega_1) \times H^s(\Omega_2)$, $s \geqslant 2$ be the solution to the interface problem* (3.7). *Furthermore, let $u_h \in V_h$ be the solution to the CutFEM formulation* (3.13). *Then with $r = \min\{s, k+1\}$ the error $u - u_h$ satisfies*

$$\|u - u_h\|_{a_h} \lesssim \sigma^{\frac{1}{2}} h^{r-1} \|u\|_{r,\Omega_1 \cup \Omega_2}.$$

Chapter 4

Temporal discretization for the EMI model*

The EMI model consists of a PDE system coupled with an ODE system. Operator splitting is a method for solving this by breaking the problem into subproblems. Each subproblem can then be solved with solution methods dedicated to the specific subproblem. In this chapter, we first briefly review an operator splitting known as Godunov splitting and show how it leads to a first-order scheme when applied to general linear problems. Subsequently, we introduce a Godunov splitting scheme for the EMI problem, decoupling the membrane confined ODE system from the PDE system.

Next, we introduce the discretization of the ODE system on the membrane surface. In [60], where the EMI model was solved on a fitted mesh, the ODE system of the EMI model was solved in the surface mesh nodes. In the unfitted formulation of the EMI model, a different approach must be taken since the membrane surface is not given as a sub mesh of the background mesh. Instead, we use an approach based on the weak formulation, similar to a finite element based discretization in time of parabolic PDEs. We first introduce the weak formulation for solving a L^2-projection problem on a surface. Then, we discretize the surface ODE system in time by utilizing the L^2-projection.

4.1 Godunov splitting for linear problems

We follow the presentation of operator splitting methods presented in [55] and consider an initial value problem of the form

$$\frac{\mathrm{d}v}{\mathrm{d}t} = (L_1 + L_2)v, \tag{4.1a}$$

$$v(0) = v_0, \tag{4.1b}$$

where L_1 and L_2 are linear operators acting on v, and v_0 is a given initial condition. The initial value problem can be split into two subproblems, where the first subproblem has the form

$$\frac{\mathrm{d}v^*}{\mathrm{d}t} = L_1(v^*), \tag{4.2a}$$

$$v^*(0) = v_0, \tag{4.2b}$$

and should be solved on the interval $t \in [0, \Delta t]$. The second subproblem has the form

$$\frac{\mathrm{d}w}{\mathrm{d}t} = L_2(w), \tag{4.3a}$$

$$w(0) = v^*(\Delta t), \tag{4.3b}$$

also to be solved on the interval $t \in [0, \Delta t]$. Notice here that the solution from the first subproblem is used as an initial value in the second subproblem.

To analyze the accuracy of the splitting scheme, assume that L_1 and L_2 are linear and not dependent on t, in order to compute

$$\frac{\mathrm{d}^2v}{\mathrm{d}t^2} = (L_1 + L_2)(L_1 + L_2)v = (L_1 + L_2)^2v, \tag{4.4}$$

where the notation in the last step means that the operator $L_1 + L_2$ is applied twice to v. A Taylor expansion for the original solution of v at time Δt, inserted with (4.4) yields

$$v(\Delta t) = v_0 + \Delta t(L_1 + L_2)v_0 + \Delta t^2(L_1 + L_2)^2v_0 + \mathcal{O}(\Delta t^3).$$

The next step is to Taylor expand the solutions to each of the subproblems (4.2) and (4.3), assuming they are smooth enough. This yields

$$w(\Delta t) = v_0 + \Delta t(L_1 + L_2)v_0 + \frac{\Delta t^2}{2}(L_1^2 + L_1L_2 + L_2^2)^2v_0 + \mathcal{O}(\Delta t^3).$$

The difference between the solution from the operator splitting and the exact solution to the original problem is then

$$w(\Delta t) - v(\Delta t) = \frac{\Delta t^2}{2}(L_1L_2 - L_2L_1)v_0 + \mathcal{O}(\Delta t^3).$$

The splitting error is thus $\mathcal{O}(\Delta t^2)$ for each time step Δt and is expected to accumulate to $\mathcal{O}(\Delta t)$ after $T/\Delta t$ timesteps to reach some fixed time T. Hence the Godunov splitting scheme is of first order.

The computations above assumed that the subproblems can be solved analytically, which is often not the case. However, as long as we solve each of the problems with first-order methods, the splitting scheme would still be of first order. Higher-order methods for the subproblems would not be very beneficial as the order of the overall splitting scheme would still be first-order. The Godunov splitting scheme can with small modifications be made into a second-order scheme known as Strang splitting, see e.g. [55].

4.2 Godunov splitting for the EMI model

The Godunov splitting scheme is now applied on the EMI model with an active membrane model, presented in [60]. This yields the following splitting scheme:
Given initial values v^0, s^0, for each time step $m = 1, 2, \dots, M$

1. (ODE-step) Compute v^*, s^m by solving

$$
\begin{aligned}
v_t^* &= -\frac{1}{C_m} I_{\text{ion}}(v^*, s^m) && \text{on } \Gamma, && (4.5a)\\
s_t^m &= F(v^*, s^m) && \text{on } \Gamma, && (4.5b)
\end{aligned}
$$

   with v^{m-1} and s^{m-1} as initial values.

2. (PDE-step) Compute u_i^m, u_e^m,v^m by solving

$$
\begin{aligned}
-\nabla \cdot \sigma_e \nabla u_e^m &= 0 && \text{in } \Omega_e, && (4.6a)\\
-\nabla \cdot \sigma_i \nabla u_i^m &= 0 && \text{in } \Omega_i, && (4.6b)\\
\sigma_e \nabla u_e^m \cdot \boldsymbol{n_e} &= -\sigma_i \nabla u_i^m \cdot \boldsymbol{n_i} \equiv I_m^m && \text{on } \Gamma, && (4.6c)\\
v^m &= u_i^m - u_e^m && \text{on } \Gamma, && (4.6d)\\
v_t^m &= \frac{1}{C_m} I_m^m && \text{on } \Gamma, && (4.6e)
\end{aligned}
$$

   with v^* as initial value.

The next step is now to discretize both steps in time.

4.3 Time discretization for the PDE step

In to discretize the PDE-step in time we use Implicit Euler on (4.6e), yielding

$$
v^m = v^{m-1} + \frac{\Delta t}{C_m} I_m^m,
$$

where Δt is the size of the time step. We will in the two following chapters discretize the PDE step in space with two different unfitted formulations. In order to be able to also solve the ODE system on the unfitted mesh, we now introduce an unfitted approach to solve a L^2-projection problem.

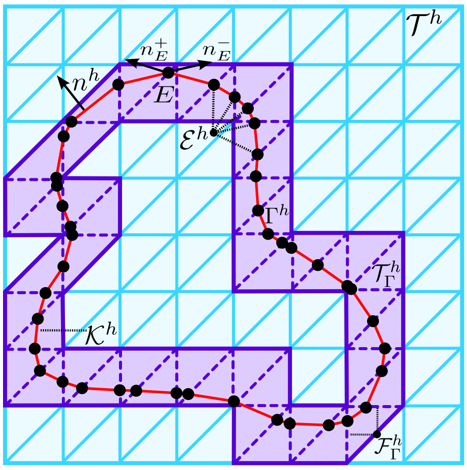

Figure 5: Computational domain for the surface problem, taken from [21] with permission from the authors, with the background mesh $\mathcal{T}^h$, the active mesh $\mathcal{T}_\Gamma^h$ in purple and internal faces $\mathcal{F}_\Gamma^h$ in dotted lines

4.4 A stabilized L^2-projection on unfitted surfaces

Let $f \in L^2(\Gamma)$ be some given function on the surface Γ. Let $\mathcal{T}^h$ be the background mesh and define the active mesh associated with Γ by

$$\mathcal{T}_\Gamma^h = \{T \in T_h | T \cap \Gamma \neq \emptyset\}.$$

Define the corresponding set of interior faces by

$$\mathcal{F}_\Gamma^h = \{F = T^+ \cap T^- | T^+, T^- \in \mathcal{T}_\Gamma^h\}.$$

Figure 5 shows $\mathcal{T}_\Gamma^h$ in purple and the interior faces in dotted lines. Define the discrete function space $V_h = \mathbb{P}_1^c(\mathcal{T}_\Gamma^h)$ to be the space of piecewise linear continuous functions on $\mathcal{T}_\Gamma^h$. The simple and natural formulation to define the L^2-projection would be: find $u_h \in V_h$ such that

$$m_h(u_h, w) = (f, w)_\Gamma \quad \forall w \in V_h, \tag{4.7}$$

where $m_h(u_h, w) = (u_h, w)_\Gamma$. However, the discrete formulation (4.7) suffers from similar issues as the unstabilized unfitted finite element formulation of the Poisson problem discussed earlier. Let $\mathcal{M}$ be the mass matrix associated with m_h such that $\mathcal{M}_{ij} = m(\phi_i, \phi_j)$ where $\{\phi_i\}_{i=1}^N$ is the basis functions of V_h. In Chapter 3, it was stated that to bound the condition number of the stiffness matrix associated with the Poisson problem, a stabilization term was needed. A similar challenge arises for the mass matrix associated with (4.7). As a remedy, a stabilization term s_h can be added. The resulting stabilized L^2-projection is given by: find $u_h \in V_h$ such that

$$M_h(u_h, v) = (f, w)_\Gamma \quad \forall w \in V_h, \tag{4.8}$$

where

$$M_h(u_h, v) := (u_h, w)_\Gamma + s_h(u, w).$$

As realization for the stabilization term, we use a face based stabilization proposed in [21]

$$s_h(v, w) = \sum_{F \in \mathcal{F}_\Gamma^h} \gamma_b h_F^2 ([\partial_n v], [\partial_n w])_F, \tag{4.9}$$

where γ_b is some positive parameter. Note that (4.9) resembles the stabilization discussed in Section 3.4. An important note about this stabilization term is that it is only suitable for first-order elements. For higher-order elements a normal gradient based stabilization was proposed in [21], where also the following a priori estimate was proven.

Theorem 4.1 (A priori estimate)**.** *Let $f \in H^2(\Gamma)$ and assume that $u_h \in V_h$ solves the stabilized weak formulation* (4.8)*. Then we have that*

$$\|f - u_h\|_\Gamma \lesssim h^2 \|f\|_{2,\Gamma}.$$

4.5 Discretization of ODEs on an unfitted surface

Now, we can use the stabilized L^2-projection to solve the ODE system on an unfitted surface. We consider the ODE system from the first step in the operator splitting scheme in Section 4.2. First, we discretize pointwise in time, using an explicit Euler step to pass from t^n to $t^{n+1} = t^n + \tau$, yielding

$$v^{n+1}(x) - v^n(x) = -\tau\big(I_{\text{ion}}(v^n(x), s^n(x))\big), \tag{4.10a}$$

$$s^{n+1}(x) - s^n(x) = \tau\big(F(v^n(x), s^n(x))\big). \tag{4.10b}$$

Next, we discretize in space, letting the background mesh $\mathcal{T}^h$ and the active mesh $\mathcal{T}_\Gamma^h$ be as in Section 4.4. A weak formulation is obtained by multiplying with tests functions $w_1, w_2 \in \mathcal{T}_\Gamma^h$, yielding

$$\begin{aligned}(v^{n+1} - v^n, w_1)_\Gamma &= -\tau\big(I_{\text{ion}}(v^n, s^n), w_1\big)_\Gamma,\\ (s^{n+1} - s^n, w_2)_\Gamma &= \tau\big(F(v^n, s^n), w_2\big)_\Gamma.\end{aligned}$$

Adding the same stabilization as for the L^2-projection problem, we arrive at the following system of equations to be solved for each time step $n = 1, \dots, N$,

$$\begin{aligned}M_h(v^{n+1}, w_1) &= m_h\big(v^n - \tau I_{\text{ion}}(v^n, s^n), w_1\big),\\ M_h(s^{n+1}, w_2) &= m_h\big(s^n + \tau F(v^n, s^n), w_2\big).\end{aligned}$$

The initial conditions v^0 and s^0 also needs to be specified. An approach could be to use the stabilized L^2-projection of the initial value such that

$$\begin{aligned} M_h(v^0, w_1) &= \tau m_h(v(t_0)), \\ M_h(s^0, w_2) &= \tau m_h(s(t_0)). \end{aligned}$$

Another way of setting the initial value conditions is to use interpolation. We will use the latter approach in our numerical implementations.

Chapter 5

A single-dimensional formulation of the EMI PDEs and its discretization

The time discretized EMI PDEs lead to an elliptic interface problem with unusual interface conditions. In this chapter, we review a single-dimensional weak formulation of the EMI PDEs and show well-posedness. Next, we formulate discrete FEM and CutFEM formulations. We prove that both formulations give optimal a priori error estimates and establish that the CutFEM formulation has geometrically robust condition numbers, meaning that they are insensitive to how the interface cuts the computational domain.

5.1 Weak formulation

The time discretized EMI model as presented in Section 4.3 can be written as a coupling of two Poisson problems with a Robin-type interface condition,

$$
\begin{aligned}
-\nabla \cdot \sigma_e \nabla u_e &= 0 && \text{in } \Omega_e, && (5.1\text{a})\\
-\nabla \cdot \sigma_i \nabla u_i &= 0 && \text{in } \Omega_i, && (5.1\text{b})\\
\sigma_e \nabla u_e \cdot \boldsymbol{n_e} &= -\sigma_i \nabla u_i \cdot \boldsymbol{n_i} \equiv I_m && \text{on } \Gamma, && (5.1\text{c})\\
u_i - u_e &= C_m^{-1} \Delta t I_m + f && \text{on } \Gamma, && (5.1\text{d})\\
u_e &= 0 && \text{on } \partial\Omega, && (5.1\text{e})
\end{aligned}
$$

where we have written $v_0 = f$. Further, we have also added a Dirichlet condition on the outer boundary of the domain. We will in assume that Γ is of class C^2. Following the presentation in [42], a weak formulation of the spatial EMI problem can be derived as follows. Define the function spaces

$$
V_i = H^1(\Omega_i), \quad V_e = H_0^1(\Omega_e),
$$

and let $V = V_i \times V_e$. Multiply (5.1b) with a test function $v_i \in V_i$ and integrate over Ω_i, and multiply (5.1a) with a test function $v_e \in V_e$ and integrate over Ω_e. Integration by parts gives the weak formulation: find $u \in V$ such that

$$\int_{\Omega_e} \sigma_e \nabla u_e \cdot \nabla v_e \, \mathrm{d}x - \int_{\Gamma} \sigma_e \nabla u_e \cdot \boldsymbol{n_e} v_e \, \mathrm{d}s = 0, \tag{5.2a}$$

$$\int_{\Omega_i} \sigma_i \nabla u_i \cdot \nabla v_i \, \mathrm{d}x - \int_{\Gamma} \sigma_i \nabla u_i \cdot \boldsymbol{n_i} v_i \, \mathrm{d}s = 0, \tag{5.2b}$$

for all $v \in V$. By using (5.1c), (5.1d) can be inserted into (5.2) to arrive at the classical weak formulation: find $u \in V$ such that

$$a(u, v) = l(v) \quad \forall v \in V, \tag{5.3}$$

where the bilinear form a is given as

$$a(u, v) = \int_{\Omega_e} \sigma_i \nabla u_i \cdot \nabla v_i \, \mathrm{d}x + \int_{\Omega_i} \sigma_e \nabla u_e \cdot \nabla v_e \, \mathrm{d}x + \frac{C_m}{\Delta t} \int_{\Gamma} (u_e - u_i)(v_e - v_i) \, \mathrm{d}s, \tag{5.4}$$

and the linear form l as

$$l(v) = \frac{C_m}{\Delta t} \int_{\Gamma} f(v_i - v_e) \, \mathrm{d}s. \tag{5.5}$$

5.2 Well-posedness of the weak formulation

In this section we will show that the weak formulation is well-posed. First, notice that the bilinear form (5.4) induces the following energy norm for $v = (v_i, v_e) \in V = V_i \times V_e$,

$$\|v\|_a^2 := \sigma_e \|\nabla v_e\|_{L^2(\Omega_e)}^2 + \sigma_i \|\nabla v_i\|_{L^2(\Omega_i)}^2 + \frac{C_m}{\Delta t} \|v_e - v_i\|_{\Gamma}^2. \tag{5.6}$$

We now argue that $\|\cdot\|_a^2$ is a norm. It is clear from construction that both homogeneity and triangle inequality are satisfied. To show that $\|\cdot\|_a$ it is positive definite, notice that obviously $v = 0 \implies \|v\|_a = 0$. For the other direction, assume that $\|v\|_a = 0$. This implies that $\|\nabla v_e\|_{L^2(\Omega_e)} = \|\nabla v_i\|_{L^2(\Omega_i)} = \|v_e - v_i\|_{\Gamma} = 0$. Recall that the constant function v_e is zero on the outer boundary, hence $v_e = 0$ on Ω_e. This, combined with $\|v_e - v_i\|_{\Gamma} = 0$, means that the constant function v_i is zero on Γ. We can therefore conclude that $\|v\|_a = 0 \iff v = 0$.

To prove that there exists a solution to the classical weak formulation of the EMI problem, we apply the Lax-Milgram Theorem.

Theorem 5.1 (Lax-Milgram [15]). *Let H be a Hilbert space with norm $\|\cdot\|_H$. Assume that we have a symmetric bilinear form $a : H \times H \to \mathbb{R}$, and a linear form $l : H \to \mathbb{R}$ where the following is satisfied* *(i) The bilinear form $a(\cdot,\cdot)$ is coercive and continuous, i.e. there exists $\alpha_1 > 0$ and $\alpha_2 >$ such that*

$$\begin{aligned} a(u,u) &\geqslant \alpha_1 \|u\|_H^2 && \forall u \in H, \\ a(u,v) &\leqslant \alpha_2 \|u\|_H \|v\|_H && \forall u, v \in H. \end{aligned}$$

(ii) The linear form $l(\cdot)$ is bounded, i.e. there exists $\beta > 0$ such that

$$l(v) \leqslant \beta \|v\|_H \quad \forall v \in H.$$

Then, there exists a unique element $u \in H$ such that

$$a(u,v) = l(v) \quad \forall v \in H.$$

In addition, it holds that

$$\|u\|_H \leqslant \frac{1}{\alpha_1} \|l\|_{H'}.$$

Theorem 5.2. *The bilinear form $a(\cdot,\cdot)$ as defined in* (5.4) *is coercive and continuous, that is*

$$\begin{aligned} a(v,v) &= \|v\|_a^2 && \forall u \in V, && (5.7) \\ a(u,v) &\leqslant 3\|u\|_a \|v\|_a && \forall u, v \in V. && (5.8) \end{aligned}$$

Assuming $f \in L^2(\Gamma)$, the linear form defined in (5.5) *is bounded*

$$l(v) \leqslant \|f\|_\Gamma \|v\|_a. \tag{5.9}$$

Moreover, there exists a unique solution u to equation (5.3) *which satisfies*

$$\|u\|_a \leqslant \|l\|_{a'}.$$

Proof. The coercivity result (5.7) follows directly from the definition of the energy norm. To show (5.8), applying the Cauchy-Schwarz inequality together with the definition of the energy norm yields,

$$\begin{aligned} a(u,v) &\leqslant \sigma_i \|\nabla u_i\|_{\Omega_i} \|\nabla v_i\|_{\Omega_i} + \sigma_e \|\nabla u_e\|_{\Omega_e} \|\nabla v_e\|_{\Omega_e} + \frac{C_m}{\Delta t} \|u_e - u_i\|_\Gamma \|v_e - v_i\|_\Gamma \\ &\leqslant 3\|u\|_a \|v\|_a. \end{aligned}$$

The boundedness of the linear form (5.9) follows from applying Cauchy-Schwarz,

$$l(v) = \frac{C_m}{\Delta t} \int_\Gamma f(v_i - v_e) \, \mathrm{d}s \leqslant \frac{C_m}{\Delta t} \|v_i - v_e\|_\Gamma \|f\|_\Gamma \leqslant \|f\|_\Gamma \|v\|_a.$$

The existence of a unique solution then follows directly from the Lax-Milgram Theorem. □

5.3 A classical finite element discretization

In this section, we will describe the discretization of the fitted version of the spatial EMI problem before we derive a priori error estimates. Suppose that for each of the subdomains Ω_i and Ω_e we have finite element partitionings into the quasi-uniform submeshes $\mathcal{T}_{h,i}$ and $\mathcal{T}_{h,e}$ such that they are non-overlapping, and that the faces in the interface between $\mathcal{T}_{h,i}$ and $\mathcal{T}_{h,e}$ form Γ. Define then $\mathcal{T}_h$ to be a mesh of Ω consisting of the two submeshes. See an illustration for a circular cell in Figure 6. Next, we define the finite element spaces

$$V_{h,i} = \mathbb{P}_k^c(\mathcal{T}_{h,i}), \quad V_{h,e} = \{v \in \mathbb{P}_k^c(\mathcal{T}_{h,e}) : v|_{\partial\Omega} = 0\},$$

where $k \in \mathbb{N}$ and let $V_h = V_{h,i} \times V_{h,e}$. The single-dimensional formulation is: find $u_h \in V_h$ such that

$$a(u_h, v) = l(v) \quad \forall v \in V_h. \tag{5.10}$$

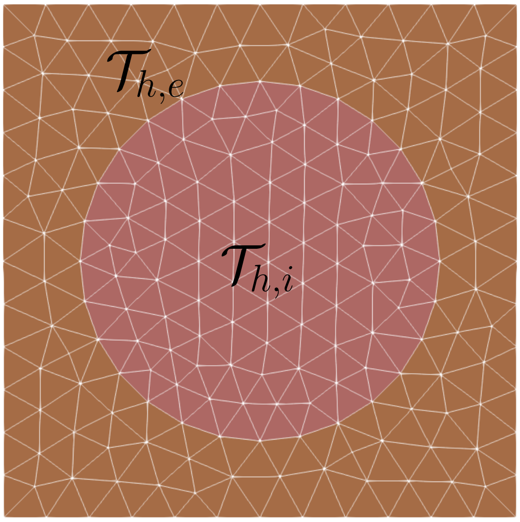

Figure 6: Illustration of fitted discretization for the EMI model with a circular cell.

5.3.1 Error estimates for the fitted discretization

To derive a priori error estimates, we define an interpolation operator. For an element T where $\{\phi_i\}_{i=1}^n$ is the Lagrangian basis of $\mathbb{P}_k^c(T)$, the local interpolation operator $\mathcal{I}_h^T : H^s(T) \to \mathbb{P}_k^c(T)$ for a function v on T is defined by

$$\mathcal{I}_h^T v(x) = \sum_i^n v(x_i)\phi_i(x).$$

Next, the global interpolation operator $\mathcal{I}_{h,j} : H^s(\Omega_j) \to V_{h,i}$ for $j = i, e$ is defined by

$$\mathcal{I}_{h,j} v_j \mid_T = \mathcal{I}_h^T v_j,$$

for $v_j \in V_j$ and $T \in \mathcal{T}_{h,j}$. The interpolation operator on the total space $\Omega = \Omega_i \cup \Omega_e$ is then defined by

$$\mathcal{I}_h u = (\mathcal{I}_{h,i} u_i, \mathcal{I}_{h,e} u_e).$$

Proof of the following estimate for the interpolant can be found in [15, 34].

Theorem 5.3 (Local interpolation error)**.** *Let* $v \in H^s(T)$, $s \geqslant 1$ *and assume* $V_j = \mathbb{P}_k^c(\mathcal{T}_{h,j})$. *With* $r = \min\{s, k+1\}$, *the local interpolation error satisfies the following,*

$$|v - \mathcal{I}_{h,j} v|_{r,T} \lesssim h_T^{s-r} |v|_{s,T}, \tag{5.11}$$

$$|v - \mathcal{I}_{h,j} v|_{r,F} \lesssim h_T^{s-r-1/2} |v|_{s,T}. \tag{5.12}$$

Also, for the interpolation error on Ω_j *it holds that*

$$\|v - \mathcal{I}_{h,j} v\|_{r,\Omega_j} \lesssim h^{s-r} |v|_{s,\Omega_j}, \tag{5.13}$$

$$\|v - \mathcal{I}_{h,j} v\|_{r,\mathcal{F}_h} \lesssim h^{s-r-1/2} |v|_{s,\Omega_j}, \tag{5.14}$$

$$\|v - \mathcal{I}_{h,j} v\|_{r,\Gamma} \lesssim h^{s-r-1/2} |v|_{s,\Omega_j}, \tag{5.15}$$

for all $v \in H^s(\Omega_j)$.

With the interpolation estimates, we can estimate the global interpolation error in the $\|\cdot\|_a$-norm.

Corollary 5.4 (Global interpolation error)**.** *Assume* $u = (u_i, u_e) \in H^s(\Omega_i) \times H^s(\Omega_e)$ *and* $V_h = \mathbb{P}_k^c(\mathcal{T}_{h,i}) \times \mathbb{P}_k^c(\mathcal{T}_{h,e})$. *With* $r = \min\{s, k+1\}$ *the global interpolation error satisfies*

$$\|u - \mathcal{I}_h u\|_a \lesssim h^{r-1} \left(\sigma_i \|u_i\|_{r,\Omega_i}^2 + \sigma_e \|u_e\|_{r,\Omega_e}^2 + C_m \frac{h}{\Delta t} \|u\|_{r,\Omega_i \cup \Omega_e}^2 \right)^{\frac{1}{2}}. \tag{5.16}$$

Proof. Taking the $\|\cdot\|_a$-norm of $u - \mathcal{I}_h u$, and applying (5.13) and (5.15) yields,

$$\begin{aligned}
\|u - \mathcal{I}_h u\|_a^2 &= \sigma_i \|\nabla(u_i - \mathcal{I}_{h,i} u_i)\|_{\Omega_i}^2 + \sigma_e \|\nabla(u_e - \mathcal{I}_{h,e} u_e)\|_{\Omega_e}^2 \\
&\quad + \frac{C_m}{\Delta t} \|u_e - \mathcal{I}_{h,e} u_e - (u_i - \mathcal{I}_{h,i} u_i)\|_\Gamma^2 \\
&\leqslant h^{2(r-1)} (\sigma_i \|u_i\|_{r,\Omega_i}^2 + \sigma_e \|u_e\|_{r,\Omega_e}^2) + \frac{2C_m}{\Delta t} (\|u_i - \mathcal{I}_h u_i\|_\Gamma^2 + \|u_e - \mathcal{I}_h u_e\|_\Gamma^2) \\
&\lesssim h^{2(r-1)} \Big(\sigma_i \|u_i\|_{r,\Omega_i}^2 + \sigma_e \|u_e\|_{r,\Omega_e}^2 + C_m \frac{h}{\Delta t} \|u\|_{r,\Omega_i \cup \Omega_e}^2 \Big).
\end{aligned}$$

□

Next, we demonstrate that the weak formulation has the Galerkin orthogonality property.

Lemma 5.5 (Galerkin orthogonality)**.** *Let $u \in H^s(\Omega_i) \times H^s(\Omega_e)$ be the solution to the spatial EMI problem* (5.1)*, and let let $u_h \in V_h$ be the solution to the finite element formulation* (5.10)*. Then*

$$a(u - u_h, v) = 0 \quad \forall v \in V_h. \tag{5.17}$$

We now have all ingredients needed to derive the following a priori error estimate in the energy norm.

Theorem 5.6 (A priori error estimate)**.** *Let $u \in H^s(\Omega_i) \times H^s(\Omega_e)$ be the solution to the spatial EMI problem* (5.1)*, and let $u_h \in V_h$ be the solution to the finite element formulation* (5.10)*. With $r = \min\{s, k+1\}$ the error $u - u_h$ satisfies*

$$\|u - u_h\|_a \lesssim h^{r-1} \left(\sigma_i \|u_i\|^2_{r,\Omega_i} + \sigma_e \|u_e\|^2_{r,\Omega_e} + C_m \frac{h}{\Delta t} \|u\|^2_{r,\Omega_i \cup \Omega_e} \right)^{\frac{1}{2}}. \tag{5.18}$$

Proof. The coercivity result (5.7) combined with the Galerkin orthogonality (5.17) and the boundedness (5.8) yields,

$$\begin{aligned} \|u - u_h\|_a^2 &= a(u - u_h, u - u_h) \\ &= a(u - u_h, u - u_h) + a(u - u_h, u_h - I_h u) \\ &= a(u - u_h, u - I_h u) \\ &\lesssim \|u - u_h\|_a \|u - I_h u\|_a. \end{aligned}$$

Now dividing by $\|u - u_h\|_a$, and applying (5.16) gives the desired estimate. □

With the above estimate we can also derive an estimate for the error in the L^2-norm, using the Aubin-Nitsche trick.

Remark 5.7. To use the Aubin-Nitsche trick, we typically need an elliptic regularity result. At the moment it is not clear if this exists for the adjoint problem of the EMI PDEs,

$$-\nabla \cdot \sigma_e \nabla \phi_e = e_e \qquad \text{in } \Omega_e, \tag{5.19a}$$
$$-\nabla \cdot \sigma_i \nabla \phi_i = e_i \qquad \text{in } \Omega_i, \tag{5.19b}$$
$$\sigma_e \nabla \phi_e \cdot \boldsymbol{n_e} = -\sigma_i \nabla \phi_i \cdot \boldsymbol{n_i} \equiv I_m \qquad \text{on } \Gamma, \tag{5.19c}$$
$$\phi_i - \phi_e = C_m^{-1} \Delta t I_m \qquad \text{on } \Gamma, \tag{5.19d}$$
$$\phi_e = 0 \qquad \text{on } \partial\Omega. \tag{5.19e}$$

This is subject to further investigation. For a standard Poisson interface problem, we can find elliptic regularity results shown in [51] and [14]. In addition, Grisvard discusses regularity for a standard Poisson problem with Robin boundary condition in [32]. For now we will assume that under suitable assumptions on the domain Ω and interface Γ with $e = (e_i, e_e) \in L^2(\Omega_i) \cup L^2(\Omega_e)$, there exists a solution ϕ to (5.19) such that $\|\phi\|_{2,\Omega_i\cup\Omega_e} \leqslant \|e\|_{\Omega_i\cup\Omega_e}$.

Theorem 5.8 (A priori error estimate in the L^2-norm)**.** *Let $u \in H^s(\Omega_i) \times H^s(\Omega_e)$, $s \geqslant 2$ be the solution to the spatial EMI problem* (5.1)*, and let let $u_h \in V_h$ be the solution to the finite element formulation* (5.10)*. With $r = \min\{s, k+1\}$ the error $u - u_h$ satisfies*

$$\|u - u_h\|_{\Omega_i\cup\Omega_e} \lesssim h^r \left(\max\{\sigma_i, \sigma_e\} + C_m \frac{h}{\Delta t}\right) \|u\|_{r,\Omega_i\cup\Omega_e}, \tag{5.20}$$

assuming the elliptic regularity conjecture in Remark 5.7 holds.

Proof. Note first that estimate (5.18) can be given as

$$\|u - u_h\|_a \lesssim h^{r-1} \left(\max\{\sigma_i, \sigma_e\} + C_m \frac{h}{\Delta t}\right)^{\frac{1}{2}} \|u\|_{r,\Omega_i\cup\Omega_e}. \tag{5.21}$$

We apply the standard Aubin-Nitsche duality trick. Let $e = (e_i, e_e) = u - u_h = (u_i - u_{h,i}, u_e - u_{h,e})$ and consider the adjoint problem given in (5.19). Since $e \in L^2(\Omega_i \cup \Omega_e)$ we have by assumption $\|\phi\|_{2,\Omega_i\cup\Omega_e} \leqslant \|e\|_{\Omega_i\cup\Omega_e}$. Integration by parts gives that

$$(e, v)_{\Omega_i\cup\Omega_e} = a(\phi, v).$$

By applying the Galerkin orthogonality we have that,

$$\begin{aligned}
\|e\|^2_{\Omega_i\cup\Omega_e} &= a(e, \phi) \\
&= a(e, \phi - \mathcal{I}_h\phi) \\
&\lesssim \|\phi - \mathcal{I}_h\phi\|_a \|u - u_h\|_a \\
&\lesssim h^r \left(\max\{\sigma_i, \sigma_e\} + C_m \frac{h}{\Delta t}\right) \|\phi\|_{2,\Omega_i\cup\Omega_e} \|u\|_{r,\Omega_i\cup\Omega_e} \\
&\lesssim h^r \left(\max\{\sigma_i, \sigma_e\} + C_m \frac{h}{\Delta t}\right) \|e\|_{\Omega_i\cup\Omega_e} \|u\|_{r,\Omega_i\cup\Omega_e},
\end{aligned}$$

where in the last three steps the boundedness for $\|\cdot\|_a$ was combined with estimate (5.21) and the interpolation error (5.16) for the energy norm. Now, dividing by $\|e\|_{\Omega_i\cup\Omega_e}$ gives the desired estimate. □

Remark 5.9. Notice that the error estimates are optimal as long as we have $h \lesssim \Delta t$. This means that to have optimal convergence in space the spatial refinement has to be the same or of a higher order than the temporal refinement.

5.4 A cut finite element formulation

Next, we turn to discretize the EMI model on an unfitted mesh using CutFEM. In this section, we describe the discretization, derive an a priori error estimate similar to those for the fitted version above, and give a condition number estimate. Let the two active background meshes $\mathcal{T}_{h,i}$ and $\mathcal{T}_{h,e}$ be defined as in the case for the Poisson interface problem in Section 3.5. Define the finite element spaces

$$V_{h,i} = \mathbb{P}_k^c(\mathcal{T}_{h,i}), \quad V_{h,e} = \{v \in \mathbb{P}_k^c(\mathcal{T}_{h,e}) : v|_{\partial\Omega} = 0\},$$

and the resulting total finite element space $V_h = V_{h,i} \times V_{h,e}$. Remember that the boundary condition on $\partial\Omega$ is strongly imposed, and therefore the boundary of $\mathcal{T}_{h,e}$ needs to be fitted to $\partial\Omega$. We show the analysis for triangular elements, but point out that it is also valid for rectangular elements.

Since we have natural induced interface conditions for the spatial EMI model we can show optimal convergence order without any stabilization, unlike the Poisson problems in Chapter 3 where a ghost penalty was required. However, to have geometrically robust condition numbers a ghost penalty is still needed, which will be clear when we later show estimates for the condition number of our stiffness matrix. Let the ghost penalty used for the CutFEM EMI formulation be defined by

$$g_h(v, w) = g_{h,i}(v_i, w_i) + g_{h,e}(v_e, w_e), \tag{5.22}$$

where

$$g_{h,j}(v_j, w_j) = \sum_{m=0}^{k} \sum_{F \in \mathcal{F}_{h,j}^g} \gamma_m h_F^{2m+1}([\partial_n^m v_j], [\partial_n^m w_j])_F.$$

Notice that the scaling of the ghost penalty is different than in Chapter 3, since we now only need the ghost penalty for stabilizing the condition numbers. The stabilized CutFEM single-dimensional formulation for the spatial EMI problem is then: find $u_h = (u_{h,i}, u_{h,e}) \in V_h$ such that

$$A_h(u_h, v) := a(u_h, v) + g_h(u_h, v) = l(v), \tag{5.23}$$

for all $v = (v_i, v_e) \in V_h$.

5.4.1 A priori error analysis of the CutFEM formulation

We will now derive a priori error estimates, following the idea and presentation in [33], modified to fit our problem. The ghost penalty defined for the CutFEM formulation induces the following semi-norm,

$$|v|_{g_{h,j}}^2 = g_{h,j}(v, v). \tag{5.24}$$

From the stabilized weak formulation the following discrete norm is induced for $v \in V_h$,

$$\|v\|_{A_h}^2 = \|v\|_a^2 + |v|_{g_h}^2,$$

where the last term consist of two parts,

$$|v|_{g_h}^2 = |v|_{g_{h,i}}^2 + |v|_{g_{h,e}}^2.$$

We now state that the discrete form A_h is coercive and bounded, which is a trivial extension from the fitted case.

Lemma 5.10. *The discrete form A_h is coercive and bounded, that is,*

$$\begin{aligned} A_h(v,v) &= \|v\|_{A_h}^2 \qquad \forall v \in V_h, \\ A_h(u,v) &\lesssim \|u\|_{A_h}\|v\|_{A_h} \ \forall u,v \in V_h. \end{aligned}$$

We therefore have that the weak formulation satisfies the Lax-Milgram Theorem. Note that because the bilinear form is discrete, we are now considering discrete functions already at this point, in contrast to previously where we began with continuous functions.

Next, we state local trace inverse inequalities from [34] that will be needed later.

Lemma 5.11 (Local trace inequalities)**.** *For $v \in H^1(\mathcal{T}_h)$ it holds that*

$$\|v\|_{\partial T}^2 \lesssim h_T^{-1}\|v\|_T^2 + h_T\|\nabla v\|_T^2 \quad \forall\, T \in \mathcal{T}_h, \tag{5.25}$$

$$\|v\|_{\Gamma\cap T}^2 \lesssim h_T^{-1}\|v\|_T^2 + h_T\|\nabla v\|_T^2 \quad \forall\, T \in \mathcal{T}_h. \tag{5.26}$$

Lemma 5.12 (Inverse inequalitities)**.** *For $v \in P_k(T)$ and $F \in \mathcal{F}_T$ it holds that*

$$\|\nabla v\|_{T\cap\Omega} \lesssim \|h^{-1}v\|_T, \quad \|v\|_{\Gamma\cap\Omega} \lesssim \|h^{-1/2}v\|_T, \quad \|v\|_{F\cap\Omega} \lesssim \|h^{-1/2}v\|_T. \tag{5.27}$$

$$\|\partial_n^j v\|_F \lesssim h^{r-j-1/2}\|D^r v\|_T. \tag{5.28}$$

To define a suitable interpolation operator, we first recall that there exists a bounded extension operator for Sobolev spaces,

$$(\cdot)^e : H^m(\Omega_j) \to H^m(\mathbb{R}^n),$$

such that

$$\|v^e\|_{m,\mathbb{R}^n} \lesssim \|v\|_{m,\Omega_j}.$$

This means that an approximation operator $\pi_{h,j}^e : H^m(\mathcal{T}_{h,j}) \to V_j$ can be defined by

$$\pi_{h,j}^e v := \pi_{h,j} v^e, \tag{5.29}$$

where $\pi_{h,j}$ is some suitable interpolation operator satisfying the following estimates, for example the Scott-Zhang or the Clément operator [22, 53].

Lemma 5.13. *For $v = (v_i, v_e) \in H^s(\Omega_i) \times H^s(\Omega_e)$ it holds that*

$$\|v - \pi^e_{h,j} v\|_{r,\mathcal{T}_{h,j}} \lesssim h^{s-r} |v|_{s,\Omega_j}, \tag{5.30}$$

$$\|v - \pi^e_{h,j} v\|_{r,\Gamma} \lesssim h^{s-r-1/2} |v|_{s,\Omega_j}, \tag{5.31}$$

$$\|v - \pi^e_{h} v\|_{r,\mathcal{F}_{h,j}} \lesssim h^{s-r-1/2} |v|_{s,\Omega}, \tag{5.32}$$

for $0 \leqslant r \leqslant s - 1/2$.

Proof. We prove (5.32), and note that the others can be proved in the similar manner. Combining the local trace inequality (5.25) with (5.13) gives the estimate for the approximation operator,

$$\begin{aligned}\|v - \pi^e_{h,j} v\|^2_{r,\mathcal{F}_{h,j}} &\lesssim h^{-1} \|v - \pi^e_{h,j} v\|^2_{r,T_{h,j}} + h \|\nabla(v - \pi^e_{h,j} v)\|^2_{r,T_{h,j}} \\ &\lesssim h^{2(s-r-1/2)} \|v\|^2_{s,\mathcal{T}_{h,j}} \\ &\lesssim h^{2(s-r-1/2)} \|v\|^2_{s,\Omega_j}. \end{aligned}$$

□

As in the previous section we define the total interpolation operator $\pi^e_h u = (\pi^e_{h,i} u, \pi^e_{h,e} u)$. A similar result to Corollary 5.4 for the global interpolation error can then be derived by making use of (5.30) and (5.31) where we earlier used (5.13) and (5.15).

Corollary 5.14 (Global interpolation error)**.** *Let $u \in H^s(\Omega_i) \times H^s(\Omega_e)$ and assume that $V_h = \mathbb{P}^c_k(\mathcal{T}_{h,i}) \times \mathbb{P}^c_k(\mathcal{T}_{h,e})$. With $r = \min\{s, k+1\}$ the global interpolation error satisfies*

$$\|u - \pi^e_h u\|_a \lesssim h^{r-1} \left(\max\{\sigma_i, \sigma_e\} + C_m \frac{h}{\Delta t} \right)^{\frac{1}{2}} \|u\|_{r,\Omega_i \cup \Omega_e}. \tag{5.33}$$

The Galerkin orthogonality is for the stabilized formulation replaced by a weak Galerkin orthogonality.

Lemma 5.15 (Weak Galerkin orthogonality)**.** *Let $u \in H^2(\Omega_i) \times H^2(\Omega_e)$ be the solution to the spatial EMI problem* (5.1)*, and let let $u_h \in V_h$ be the solution to the CutFEM formulation* (5.23)*. Then*

$$a(u - u_h, v) = g_h(u_h, v) \quad \forall v \in V_h. \tag{5.34}$$

Proof. Observe that $a(u, v) = l(v)$ $\forall v \in V_h$, and that $A(u_h, v) = l(v)$ $\forall v \in V_h$. Now inserting the first into the latter gives the property. □

Along with the weak Galerkin orthogonality we also need to show a bound of the approximation in the seminorm $|\cdot|_{g_h}$. Arguing as in [33], we only show this for the case of penalty parameters $\gamma_0 = \cdots = \gamma_k = 1$, since all choices of the parameters will lead to discrete norms that are equivalent.

Lemma 5.16 (Weak consistency for the ghost penalty)**.** *For* $v \in H^s(\Omega_i) \times H^s(\Omega_e)$ *with* $r = \min\{s, k+1\}$ *the seminorm* $|\cdot|_{g_h}$ *satisfies*

$$|\pi_h^e v|_{g_h} \lesssim h^r \|v\|_{r,\Omega_i \cup \Omega_e}. \tag{5.35}$$

Proof. We only show the case for one component, $v_i \in H^s(\Omega_i)$. Let $r = \min\{s, k+1\}$, and remember the definition of the seminorm,

$$|\pi_{h,i}^e v_i|_{g_{h,i}}^2 = \sum_{j=0}^{k} h^{2j+1} \|[\partial_n^j \pi_{h,i}^e v_i]\|_{\mathcal{F}_{h,i}^g}^2. \tag{5.36}$$

Note first that from the Sobolev embedding theorem $[\partial_n^j v]_F = 0$ for $0 \leqslant j \leqslant r-1$. To make use of this the sum is split into two parts:

$$\sum_{j=0}^{k} h^{2j+1} \|[\partial_n^j \pi_{h,i}^e v_i]\|_{\mathcal{F}_{h,i}^g}^2 = \sum_{j=0}^{r-1} h^{2j+1} \|[\partial_n^j (\pi_{h,i}^e v_i - v_i^e)]\|_{\mathcal{F}_{h,i}^g}^2 + \sum_{j=r}^{k} h^{2j+1} \|[\partial_n^j \pi_{h,i}^e v_i]\|_{\mathcal{F}_{h,i}^g}^2.$$

For the first sum we apply (5.32),

$$\sum_{j=0}^{r-1} h^{2j+1} \|[\partial_n^j (\pi_{h,i}^e v_i - v_i^e)]\|_{\mathcal{F}_{h,i}^g}^2 \lesssim h^{2r} \|v_i\|_{r,\Omega_i}^2.$$

For the second sum we employ the inverse estimate (5.28), together with the stability of $\pi_{h,i}$, and the bound of the Sobolev extension operator, yielding

$$\sum_{j=r}^{k} h^{2j+1} \|[\partial_n^j \pi_{h,i}^e v_i]\|_{\mathcal{F}_{h,i}^g}^2 \lesssim h^{2r} \|D^r \pi_{h,i}^e v_i\|_{\mathcal{T}_{h,i}}^2 \lesssim h^{2r} \|\pi_{h,i}^e v_i\|_{r,\mathcal{T}_{h,i}}^2 \lesssim h^{2r} \|v_i\|_{r,\Omega_i}^2. \qquad \square$$

With these results, we have all ingredients to state the a priori error estimates.

Theorem 5.17 (A priori error estimates)**.** *Let* $u \in H^s(\Omega_i) \times H^s(\Omega_e)$*,* $s \geqslant 2$ *be the solution to the spatial EMI problem* (5.1)*, and let let* $u_h \in V_h$ *be the solution to the CutFEM formulation* (5.23)*. With* $r = \min\{s, k+1\}$ *the error* $u - u_h$ *satisfies*

$$\|u - u_h\|_a \lesssim h^{r-1}\left(h + \sqrt{\alpha}\right) \|u\|_{r,\Omega_i \cup \Omega_e}, \tag{5.37}$$

$$\|u - u_h\|_{\Omega_i \cup \Omega_e} \lesssim h^r \left(\alpha + h\sqrt{\alpha} + h^2\right) \|u\|_{r,\Omega_i \cup \Omega_e}. \tag{5.38}$$

where $\alpha = \max\{\sigma_i, \sigma_e\} + C_m h(\Delta t)^{-1}$*, and* (5.38) *holds assuming the elliptic regularity conjecture in Remark* (5.7) *holds.*

Proof. The proofs are mainly the same as for Theorem 5.6 and Theorem 5.8, except that we now only have the weak Galerkin orthogonality. Let $\alpha = \max\{\sigma_i, \sigma_e\} + C_m h(\Delta t)^{-1}$.

For (5.37) we divide the error into two parts,

$$\|u - u_h\|_a \leqslant \|u - \pi_h^e u\|_a + \|\pi_h^e u - u_h\|_a \leqslant \|u - \pi_h^e u\|_a + \|\pi_h^e u - u_h\|_{A_h}. \tag{5.39}$$

For the second part we apply the weak Galerkin orthogonality together with estimate (5.33).

$$\begin{aligned}
\|\pi_h^e u - u_h\|_{A_h}^2 &\lesssim a(\pi_h^e u - u_h, \pi_h^e u - u_h) + g_h(\pi_h^e u - u_h, \pi_h^e u - u_h) \\
&= a(\pi_h^e u - u, \pi_h^e u - u_h) + g_h(\pi_h^e u, \pi_h^e u - u_h) \\
&\lesssim \|\pi_h^e u - u\|_a \|\pi_h^e u - u_h\|_a + |\pi_h^e u|_{g_h} |\pi_h^e u - u_h|_{g_h} \\
&\lesssim h^{r-1}\sqrt{\alpha}\|u\|_{r,\Omega_i\cup\Omega_e} \|\pi_h^e u - u_h\|_{A_h} + h^r \|u\|_{r,\Omega_i\cup\Omega_e} \|\pi_h^e u - u_h\|_{A_h}.
\end{aligned}$$

Dividing by $\|\pi_h^e u - u_h\|_{A_h}$ gives

$$\|\pi_h^e u - u_h\|_{A_h} \lesssim h^{r-1}\sqrt{\alpha}\|u\|_{r,\Omega_i\cup\Omega_e} + h^r \|u\|_{r,\Omega_i\cup\Omega_e}. \tag{5.40}$$

Inserting this into (5.39) and applying (5.33) on the first term gives the estimate.

For (5.38) we again use the adjoint problem (5.19). The weak Galerkin orthogonality, estimate (5.33) and (5.40) yields

$$\begin{aligned}
\|e\|_{\Omega_i\cup\Omega_e}^2 &= a(e, \phi) \\
&= a(e, \phi - \pi_h^e \phi) + g_h(u_h, \pi_h^e \phi) \\
&= a(e, \phi - \pi_h^e \phi) + g_h(u_h - \pi_h^e u, \pi_h^e \phi) + g_h(\pi_h^e u, \pi_h^e \phi) \\
&\lesssim \|\phi - \pi_h^e \phi\|_a \|u - u_h\|_a + \|u_h - \pi_h^e u\|_{A_h} |\pi_h^e \phi|_{g_h} + |\pi_h^e u|_{g_h} |\pi_h^e \phi|_{g_h} \\
&\lesssim (\alpha h^r + \sqrt{\alpha}\ h^{r+1} + h^{r+2}) \|\phi\|_{2,\Omega_i\cup\Omega_e} \|u\|_{r,\Omega_i\cup\Omega_e} \\
&\lesssim (\alpha h^r + \sqrt{\alpha}\ h^{r+1} + h^{r+2}) \|e\|_{\Omega_i\cup\Omega_e} \|u\|_{r,\Omega_i\cup\Omega_e},
\end{aligned}$$

dividing by $\|e\|_{\Omega_i\cup\Omega_e}$ gives the estimate. □

5.4.2 Condition number scaling

The last part of the theoretical analysis consists of showing how the ghost penalty gives robust condition numbers of the stiffness matrix. Let us begin by recalling from Chapter 3 that we define the stiffness matrix corresponding to the weak formulation as

$$(\mathcal{A}V, W)_{\mathbb{R}^N} = A_h(v, w) \quad \forall v, w \in V_h, \tag{5.41}$$

where V, W are the vectors of coefficients related to v and w. An ill-conditioned stiffness matrix could give trouble with error propagation when using a direct solver, and increase the number of iterations for an iterative solver. As the next step we give two properties of the ghost penalty which will be needed later. First, with the ghost penalty the L^2-norm can be extended from the physical domain to the entire mesh $\mathcal{T}_h$, which was proven in [33].

Lemma 5.18 (L^2-norm extension property)**.** *For all $v \in V_h$ we have that,*

$$\|v\|_{\mathcal{T}_{h,i} \cup \mathcal{T}_{h,e}} \lesssim \|v\|_{\Omega_i \cup \Omega_e} + |v|_{g_h}. \tag{5.42}$$

The second property is that the ghost penalty satisfies an inverse inequality.

Lemma 5.19 (Inverse inequality for the ghost penalty)**.** *For $v \in V_h$ we have that*

$$|v|_{g_h} \lesssim \|v\|_{\mathcal{T}_{h,i} \cup \mathcal{T}_{h,e}}. \tag{5.43}$$

Proof. Follows from applying (5.28), here shown for one component v_i,

$$|v_i|^2_{g_{h,i}} = \sum_{j=0}^{k} h^{2j+1} \|[\partial_n^j v_i]\|^2_{\mathcal{F}^g_{h,i}} \lesssim \|v_i\|^2_{\mathcal{T}_{h,i}}. \qquad \square$$

Now we state a lemma which we will use to pass between the continuous L^2-norm and the discrete l^2-norm of the corresponding coefficient vectors. A proof can be found in [50].

Lemma 5.20. *For $v \in V_h$ it holds that*

$$h^{d/2} \|V\|_{\mathbb{R}^N} \lesssim \|v\|_{L^2(\mathcal{T}_{h,i} \cup \mathcal{T}_{h,e})} \lesssim h^{d/2} \|V\|_{\mathbb{R}^N}. \tag{5.44}$$

Along with Lemma 5.20, we need two other main ingredients to estimate the condition number an inverse estimate for $\|\cdot\|_{A_h}$ and after that a discrete Poincare inequality.

Proposition 5.21 (Inverse estimate for $\|\cdot\|_{A_h}$)**.** *For $v \in V_h$ it holds that*

$$\|v\|_{A_h} \lesssim h^{-1} \Big(\max\{\sigma_i, \sigma_e\} + C_m \frac{h}{\Delta t} + h^2 \Big)^{\frac{1}{2}} \|v\|_{\mathcal{T}_{h,i} \cup \mathcal{T}_{h,e}}. \tag{5.45}$$

Proof. Combining the inverse inequalities (5.27) and the inverse inequality for the ghost penalty yields

$$\begin{aligned} \|v\|^2_{A_h} &= \sigma_e \|\nabla v_e\|^2_{L^2(\Omega_e)} + \sigma_i \|\nabla v_i\|^2_{L^2(\Omega_i)} + \frac{C_m}{\Delta t} \|v_e - v_i\|^2_\Gamma + |v|^2_{g_h} & (5.46) \\ &\lesssim \Big(h^{-2} \max\{\sigma_i, \sigma_e\} + h^{-1} \frac{C_m}{\Delta t} + 1 \Big) \|v\|^2_{\mathcal{T}_{h,i} \cup \mathcal{T}_{h,e}}. & (5.47) \end{aligned}$$

$\square$

Proposition 5.22 (Discrete Poincare inequality). *For $v \in V_h$ it holds that*

$$\|v\|_{\mathcal{T}_{h,i} \cup \mathcal{T}_{h,e}} \lesssim \max\{\sigma_i^{-1}, \sigma_e^{-1}, \Delta t (C_m)^{-1}, 1\} \|v\|_a. \tag{5.48}$$

Proof. Since Lemma 5.18 gives that $\|v\|_{\mathcal{T}_{h,i} \cup \mathcal{T}_{h,e}} \lesssim \|v\|_{\Omega_i \cup \Omega_e} + |v|_{g_h}$, the main problem is showing a bound for $\|v\|_{\Omega_i \cup \Omega_e}$. Let us first define

$$\|v\|_{a,1}^2 := \|\nabla v_e\|_{L^2(\Omega_e)}^2 + \|\nabla v_i\|_{L^2(\Omega_i)}^2 + \|v_e - v_i\|_\Gamma^2, \tag{5.49}$$

which is the same as the $\|\cdot\|_a$ norm with all constants set to 1. We now want to prove that

$$\|v\|_{\Omega_i \cup \Omega_e} \leqslant C \|v\|_{a,1}, \tag{5.50}$$

where C only depends on the space dimension and $\Omega_i \cup \Omega_e$. This will be done following how Poincaré's inequality is proven in [25], arguing by contradiction. If the estimate was false there would for each integer $k = 1, \dots$ exist a function $u^k \in H^1(\Omega)$ such that,

$$\|u^k\|_{\Omega_i \cup \Omega_e} \geqslant k \|u^k\|_{a,1}. \tag{5.51}$$

These functions can be normalized, such that

$$v^k = \frac{u^k}{\|u^k\|_{\Omega_i \cup \Omega_e}},$$

which gives $\|v_k\|_{\Omega_i \cup \Omega_e} = 1$. Further, thanks to (5.51) the following inequality must also hold,

$$\|v^k\|_{a,1} \leqslant \frac{1}{k}. \tag{5.52}$$

From the Rellich-Kondrachov compactness Theorem [25] there must exists a subsequence $\{v^{k_j}\}_{j=0}^\infty$ and a function $v \in L^2(\Omega_i \cup \Omega_e)$ such that

$$v^{k_j} \to v \quad \text{in } L^2(\Omega_i \cup \Omega_e).$$

Clearly (5.52) now gives that $\|v\|_{a,1} = 0$. As argued earlier when we in Section 5.2 showed that $\|\cdot\|_a$ is a norm, this must imply that $v = 0$. This is a contradiction, since by construction $\|v\|_{\Omega_i \cup \Omega_e} = 1$. Therefore

$$\|v\|_{\Omega_i \cup \Omega_e} \lesssim \|v\|_{a,1} \lesssim \max\{\sigma_i^{-1}, \sigma_e^{-1}, \Delta t (C_m)^{-1}\} \|v\|_a. \qquad \square$$

We now give an estimate for the condition number of the stiffness matrix defined by the relation to the discrete form, as described in Section 3.1.

Theorem 5.23 (Condition number estimate). *The condition number of the stiffness matrix satisfies*

$$\kappa(\mathcal{A}) \lesssim h^{-2} \beta^2 (\alpha + h^2), \tag{5.53}$$

where $\alpha = \max\{\sigma_i, \sigma_e\} + C_m \frac{h}{\Delta t}$, *and* $\beta = \max\{\sigma_i^{-1}, \sigma_e^{-1}, \Delta t (C_m)^{-1}, 1\}$.

Proof. Let $\alpha = \max\{\sigma_i, \sigma_e\} + C_m \frac{h}{\Delta t}$, and $\beta = \max\{\sigma_i^{-1}, \sigma_e^{-1}, \Delta t (C_m)^{-1}, 1\}$. Now combining this with the inverse estimate (5.45) yields,

$$\|w\|_{A_h} \lesssim h^{-1}\sqrt{\alpha + h^2}\|w\|_{\mathcal{T}_{h,i}\cup\mathcal{T}_{h,e}} \lesssim h^{(d-2)/2}(\sqrt{\alpha + h^2})\|W\|_{\mathbb{R}^N}.$$

This gives the following estimate,

$$\begin{aligned}
\|\mathcal{A}V\|_{\mathbb{R}^N} &= \sup_{W\in\mathbb{R}^N\setminus\{0\}} \frac{(\mathcal{AV}, \mathcal{W})_{R^N}}{\|W\|_{\mathbb{R}^N}} \\
&= \sup_{w\in V_h\setminus\{0\}} \frac{A_h(v,w)}{\|w\|_{A_h}} \frac{\|w\|_{A_h}}{\|W\|_{\mathbb{R}^N}} \\
&\lesssim \frac{\|v\|_{A_h}\|w\|_{A_h}}{\|w\|_{A_h}} h^{(d-2)/2}\sqrt{\alpha + h^2} \\
&= h^{(d-2)/2}\sqrt{\alpha + h^2}\|v\|_{A_h} \\
&\lesssim h^{d-2}(\alpha + h^2)\|V\|_{\mathbb{R}^N}.
\end{aligned}$$

So then by the definition of the operator norm $\|A\|_{\mathbb{R}^N} \lesssim h^{d-2}(\alpha + h^2)$. Next, combine (5.44) with the discrete Poincare inequality (5.48),

$$\begin{aligned}
\|V\|^2_{\mathbb{R}^N} &\lesssim h^{-d}\|v\|^2_{\mathcal{T}_h} \\
&\lesssim h^{-d}\beta^2 A_h(v,v) \\
&= h^{-d}\beta^2 (V, \mathcal{A}V)_{R^N} \\
&\lesssim h^{-d}\beta^2 \|V\|_{R^N}\|\mathcal{A}V\|_{R^N},
\end{aligned}$$

which gives that $\|V\|_{R^N} \lesssim h^{-d}\beta^2\|\mathcal{A}V\|_{R^N}$. We set $V = \mathcal{A}^{-1}W$ to end up with $\|A^{-1}\|_{\mathbb{R}^N} \lesssim h^{-d}\beta^2$. Combining the estimates for $\|A\|_{\mathbb{R}^N}$ and $\|A^{-1}\|_{\mathbb{R}^N}$ give the final estimate. □

Chapter 6

A multi-dimensional formulation of the EMI PDEs and its discretization

The previous chapter introduced a weak formulation for the EMI PDEs with only the electric potentials as unknown fields. By letting the current across the membrane also be an explicit unknown, a multi-dimensional weak formulation of the EMI PDEs can be derived. Along with the possible advantage that the current is computed directly, this formulation is also more flexible for connecting several cells.

In this chapter, a derivation of the multi-dimensional primal formulation of the EMI PDEs will be given. Before establishing that a continuous inf-sup condition is satisfied, we first review some theory on saddle point problems and penalized saddle point problems. Next, we propose a new discretization based on unfitted meshes and prove that it satisfies an inf-sup condition in a suitable norm. Finally, we derive an a priori error estimate.

6.1 Weak formulation

We now review how the EMI PDEs (5.1) can be formulated in the same form as an extended saddle point problem, a formulation also known as the multi-dimensional primal formulation for the EMI PDEs [42]. First, define the function spaces,

$$V_i := H^1(\Omega_i)/\mathbb{R}, \quad V_e = H^1_0(\Omega_e), \quad V = V_i \times V_e.$$

where

$$H^1(\Omega_i)/\mathbb{R} = \Big\{ v_i \in H^1(\Omega_i) : \int_{\Omega_i} v_i \ \mathrm{d}s = 0 \Big\}.$$

The reason for defining V_i differently than in the last chapter is related to how the multi-dimensional formulation will be different than the single-dimensional formulation. Next, multiply (5.1a) and (5.1b) with test functions from V_e and V_i and use integration by parts to obtain

$$\int_{\Omega_e} \sigma_e \nabla u_e \cdot \nabla v_e \; \mathrm{d}x - \int_\Gamma v_e I_m \; \mathrm{d}s = 0,$$
$$\int_{\Omega_i} \sigma_i \nabla u_i \cdot \nabla v_i \; \mathrm{d}x + \int_\Gamma v_i I_m \; \mathrm{d}s = 0.$$

In contrast to the single-dimensional formulation, I_m is now left as a separate unknown field. Define the additional function spaces

$$Q = H^{-\frac{1}{2}}(\Gamma) \quad Q_c = H^{-\frac{1}{2}}(\Gamma) \cap \sqrt{\frac{\Delta t}{C_m}} L^2(\Gamma),$$

and let $I_m \in Q_c$. Here Q_c is a coupled space dependent on $\frac{\Delta t}{C_m}$, for more information see [10]. Multiply (5.1d) by $j_m \in Q_c$ to obtain the last equation,

$$\int_\Gamma (u_i - u_e) j_m \; \mathrm{d}s - \frac{\Delta t}{C_m} \int_\Gamma I_m j_m \; \mathrm{d}s = \int_\Gamma f j_m \; \mathrm{d}s.$$

The multi-dimensional primal formulation is then: find $u_i \in V_i$, $u_e \in V_e$, $I_m \in Q_c$ such that

$$\int_{\Omega_e} \sigma_e \nabla u_e \cdot \nabla v_e \; \mathrm{d}x - \int_\Gamma v_e I_m \; \mathrm{d}s = 0, \tag{6.1a}$$
$$\int_{\Omega_i} \sigma_i \nabla u_i \cdot \nabla v_i \; \mathrm{d}x + \int_\Gamma v_i I_m \; \mathrm{d}s = 0, \tag{6.1b}$$
$$\int_\Gamma (u_i - u_e) j_m \; \mathrm{d}s - \frac{\Delta t}{C_m} \int_\Gamma I_m j_m \; \mathrm{d}s = \int_\Gamma f j_m \; \mathrm{d}s, \tag{6.1c}$$

for all $v_i \in V_i$, $v_e \in V_e$ and $j_m \in Q_c$.

Remark 6.1. Based on standard conventions, a natural name for this formulation would be the mixed-dimensional primal formulation. However, in [42] the term mixed is used for two other formulations of the EMI PDEs, which use the current densities as explicit unknowns. To avoid confusion, we will refer to formulation (6.1) as the multi-dimensional primal formulation.

Formulation (6.1) can be interpreted as a so-called penalized saddle point formulation. In the next section, we give a short review of some theory for saddle point problems before we continue with analyzing the multi-dimensional EMI formulation.

6.2 Saddle point problems

The following presentation of saddle point problems is compiled from [13]. Let V and Q be Hilbert spaces and assume that we have symmetric bilinear forms $a : V \times V \to \mathbb{R}$ and

$b : V \times Q \to \mathbb{R}$ and linear forms $f_1 : V \to \mathbb{R}$ and $f_2 : Q \to \mathbb{R}$. Consider the following minimization problem: find the minimum over V of

$$J(u) = \frac{1}{2}a(u,u) - f_1(u), \tag{6.2a}$$

such that

$$b(u,\mu) = f_2(\mu) \quad \forall \mu \in Q. \tag{6.2b}$$

The associated Lagrange function is given by

$$\mathcal{L}(u,\lambda) := J(u) + b(u,\lambda) - f_2(\lambda)$$

and the resulting saddle point formulation of (6.2) reads,

$$\inf_{v \in V} \sup_{\mu \in Q} \mathcal{L}(v,\mu). \tag{6.3}$$

A solution (u,λ) to the problem (6.3) must satisfy the saddle point property,

$$\mathcal{L}(u,\mu) \leqslant \mathcal{L}(u,\lambda) \leqslant \mathcal{L}(v,\lambda) \quad \forall (v,\mu) \in V \times Q. \tag{6.4}$$

Further, the optimality conditions leads to the following saddle point problem: find $(u,\lambda) \in V \times Q$ such that

$$a(u,v) + b(v,\lambda) = f_1(v) \quad \forall v \in V, \tag{6.5a}$$

$$b(u,\mu) = f_2(\mu) \quad \forall \mu \in Q. \tag{6.5b}$$

Any solutions of the saddle point problem will satisfy the saddle point property (6.4). For the saddle point problem to be well-posed we have the following requirements.

Theorem 6.2 (Brezzi's splitting theorem [13]). *Let V and Q be Hilbert spaces with norms $\|\cdot\|_V$ and $\|\cdot\|_Q$, and assume we have two continuous bilinear forms $a : V \times V \to \mathbb{R}$ symmetric, $b : V \times Q \to \mathbb{R}$, and two continuous linear forms $f_1 : V \to \mathbb{R}$ and $f_2 : Q \to \mathbb{R}$. Then the saddle point problem* (6.5) *has a unique solution* (u,λ) *if the following is satisfied*

(i) The bilinear form $a(\cdot,\cdot)$ is coercive on the kernel of b, i.e. there exists $\alpha > 0$ such that

$$a(v,v) \geqslant \alpha \|v\|_V^2 \qquad \forall v \in K,$$

where $K := \{v \in V : b(v,\mu) = 0 \ \forall \mu \in Q\}$.

(ii) The bilinear form $b(\cdot,\cdot)$ satisfies an inf-sup condition, i.e there exists $\beta > 0$ such that

$$\sup_{v \in V} \frac{b(v,\mu)}{\|v\|_V} \geqslant \beta \|\mu\|_Q \quad \forall \mu \in Q.$$

Furthermore, the following a priori estimates holds,

$$\begin{aligned}\|u\|_V &\leqslant c_1\|f_1\|_{V'} + c_2\|f_2\|_{Q'}\\ \|\lambda\|_M &\leqslant c_3\|f_1\|_{V'} + c_4\|f_2\|_{Q'}\end{aligned}$$

for some constants $c_1, c_2, c_3, c_4 \geqslant 0$*.*

Condition (ii) is also known as the Ladyzhenskaya-Babuška-Brezzi condition (LBB condition) or the Brezzi condition.

6.2.1 Penalized saddle point problems

Suppose now that there is an additional symmetric positive bilinear form $c : Q_c \times Q_c \to \mathbb{R}$, where Q_c is a dense subset of Q. A penalized saddle point problem can then be written as: find $(u, \lambda) \in V \times Q_c$ such that

$$a(u, v) + b(v, \lambda) = f_1(v) \quad \forall v \in V, \tag{6.6a}$$

$$b(u, \mu) - t^2 c(\lambda, \mu) = f_2(\mu) \quad \forall \mu \in M_c, \tag{6.6b}$$

where t is a small real-valued parameter. This problem is also known as a saddle point problem with a singular perturbation. The bilinear form c introduces a semi-norm on Q_c,

$$|\mu|_c^2 := c(\mu, \mu).$$

Q_c will be assumed to be a complete space space endowed with the norm $\|\cdot\|_Q + t|\mu|_c$. The total bilinear form can be written as

$$A(u, \lambda; v, \mu) = a(u, v) + b(v, \lambda) + b(u, \mu) - t^2 c(\lambda, \mu),$$

and induces the norm

$$|||(v, \mu)||| := \|v\|_V + \|\mu\|_Q + t|\mu|_c.$$

By requiring that a is coercive on the whole space V, the extended saddle point problem can be shown to satisfy an inf-sup condition.

Theorem 6.3 (Penalized saddle point problem [12,13])**.** *Suppose the requirements of Theorem 6.2 are satisfied, and that a is elliptic on* X*. Then the extended saddle point problem* (6.6) *satisfies the inf-sup condition*

$$\inf_{(u,\mu)\in X\times Q_c} \sup_{(v,\mu)\in X\times Q_c} \frac{A(u, \mu; v, \mu)}{|||(u, \mu)||| \cdot |||(v, \mu)|||} \geqslant \gamma > 0,$$

for all $0 \leqslant t \leqslant 1$*, where* γ *is independent of* t*.*

Consider the linear mapping $L_A : V \times Q_c \to V' \times Q_c'$ defined by (6.6). If Theorem 6.3 is satisfied this means that L_A is injective, and that $L_A^{-1} : \text{range}(L_A) \to V \times Q_c$ is bounded. For the problem to be well-posed, the mapping also need to be surjective.

6.3 Stability of the weak formulation

To derive an inf-sup condition for the multidimensional EMI formulation, we now apply the theory we have presented for penalized saddle point problems. We first write formulation (6.7) as a penalized saddle point problem, where we also change the notation for the EMI problem into more standard notation: find $(u, \lambda) \in V \times Q_c$ such that

$$a(u, v) + b(v, \lambda) = 0 \tag{6.7a}$$

$$b(u, \mu) - \frac{\Delta t}{C_m} c(\lambda, \mu) = f(\mu). \tag{6.7b}$$

holds $\forall (v, \mu) \in V \times Q_c$. The bilinear forms a, b and c, and linear form f are defined as follows,

$$\begin{aligned} a(u, v) &= \sigma_e (\nabla u_e, \nabla v_e)_{\Omega_e} + \sigma_i (\nabla u_i, \nabla v_i)_{\Omega_i}, \\ b(v, \lambda) &= (v_i - v_e, \lambda)_\Gamma, \\ c(\lambda, \mu) &= (\lambda, \mu)_\Gamma, \\ f(\lambda) &= (f, \lambda)_\Gamma. \end{aligned}$$

In addition, the associated total bilinear form is defined,

$$A(u, \lambda; v, \mu) := a(u, v) + b(u, \mu) + b(v, \lambda) - \frac{\Delta t}{C_m} c(\lambda, \mu).$$

We now utilize the theory from the previous section to show that formulation (6.7) is stable and injective. First we define the following norms,

$$\begin{aligned} \|u\|_V^2 &= \sigma_e \|\nabla u_e\|_{\Omega_e}^2 + \sigma_i \|\nabla u_i\|_{\Omega_i}^2, \\ \|\mu\|_{-1/2,\Gamma} &:= \sup_{v \in H^{1/2}(\Gamma)} \frac{(v, \mu)_\Gamma}{\|v\|_{1/2,\Gamma}}, \\ \|\mu\|_Q^2 &:= \|\mu\|_{-1/2,\Gamma}^2 \\ \|\mu\|_{Q_c}^2 &:= \|\mu\|_{-1/2,\Gamma}^2 + \frac{\Delta t}{C_m} \|\mu\|_\Gamma^2, \\ |||(v, \mu)|||^2 &:= \|v\|_V^2 + \|\mu\|_{Q_c}^2. \end{aligned}$$

Theorem 6.4. *Suppose that* $\Delta t \leqslant C_m$. *Then the saddle point formulation of the EMI problem* (6.7) *is stable, i.e.*

$$\inf_{(u,\mu) \in V \times Q_c} \sup_{(v,\mu) \in V \times Q_c} \frac{A(u, \lambda; v, \mu)}{|||(u, \mu)||| \cdot |||(v, \mu)|||} \geqslant \gamma,$$

with $\gamma > 0$ *is independent of* Δt *and* C_m.

Proof. We need to prove that the requirements in Theorem 6.3 are satisfied. Continuity and coercivity for the bilinear form a follows immediately from the definition of the bilinear form and the space V,

$$\begin{aligned} a(u, v) &= \sigma_e(\nabla u_e, \nabla v_e)_{\Omega_e} + \sigma_i(\nabla u_i, \nabla v_i)_{\Omega_i} \lesssim \|u\|_V \|v\|_V, \\ a(v, v) &= \sigma_e(\nabla v_e, \nabla v_e)_{\Omega_e} + \sigma_i(\nabla v_i, \nabla v_i)_{\Omega_i} = \|v\|_V^2. \end{aligned}$$

Employing the Cauchy–Schwarz inequality we can show continuity for b,

$$\begin{aligned} b(v, \mu) &= (v_i - v_e, \mu)_\Gamma \\ &\leqslant \|v_i\|_{1/2,\Gamma} \|\mu\|_{-1/2,\Gamma} + \|v_e\|_{1/2,\Gamma} \|\mu\|_{-1/2,\Gamma} \\ &\leqslant \|v\|_V \|\mu\|_Q. \end{aligned}$$

Last part is to show that the inf-sup condition for the bilinear form b is satisfied. This term is the same as for e.g. the mortar finite element formulation for the interface Poisson problem presented in [43]. With modification we follow the proof in [43]. Note first that for a function $v \in H^{1/2}(\Gamma)$ there exists an extension operator $E^* : H^{1/2}(\Gamma) \to H^1(\Omega_i)$ such that $E^* v = v$ on Γ and $\|E^* v\|_{1,\Omega_i} \lesssim \|v\|_{1/2,\Gamma}$ [6]. To construct a function in V_i, take first a function $v^\dagger \in H_0^1$ and define

$$\tilde{v} = \frac{-\int_{\Omega_i} E^* v \,\mathrm{d}x}{\int_{\Omega_i} v^\dagger \,\mathrm{d}x} v^\dagger.$$

From Cauchy-Schwarz, the following estimate for $\tilde{v}$ follows,

$$\begin{aligned} \|\tilde{v}\|_{1,\Omega_i} &= \frac{|\int_{\Omega_i} E^* v \,\mathrm{d}x|}{|\int_{\Omega_i} \nabla v^\dagger \,\mathrm{d}x|} \|v^\dagger\|_{1,\Omega_i} \\ &\lesssim \frac{\|v^\dagger\|_{1,\Omega_i}}{|\int_{\Omega_i} v^\dagger \,\mathrm{d}x|} |\mathrm{diam}\Omega_i|^{\frac{1}{2}} \|E^* v\|_{\Omega_i} \\ &\lesssim \frac{\|v^\dagger\|_{1,\Omega_i}}{|\int_{\Omega_i} v^\dagger \,\mathrm{d}x|} |\mathrm{diam}\Omega_i|^{\frac{1}{2}} \|v\|_{1/2,\Gamma}. \end{aligned}$$

Now, $E^* v + \tilde{v}$ is in V_i, and by defining $E_0^* v$ to be $E^* v + \tilde{v}$ extended by zero on Ω_e, we have the following estimate,

$$\|E_0^* v\|_{1,\Omega_e \cup \Omega_i} \lesssim \|v\|_{1/2,\Gamma}. \tag{6.8}$$

The inf-sup condition can now be shown from the definition of the Q-norm and (6.8),

$$\begin{aligned} \|\mu\|_{-1/2,\Gamma} &= \sup_{v \in H^{1/2}(\Gamma)} \frac{(v, \mu)_\Gamma}{\|v\|_{1/2,\Gamma}} \\ &= \sup_{v \in H^{1/2}(\Gamma)} \frac{b(E_0^* v, \mu)}{\|v\|_{1/2,\Gamma}} \\ &\leqslant \sup_{v \in V} \frac{b(v, \mu)}{\|v\|_{1,\Omega_e \cup \Omega_i}} \\ &\lesssim \sup_{v \in V} \frac{b(v, \mu)}{\|v\|_V}, \end{aligned}$$

where (6.8) was utilized in the third line. □

6.4 A cut finite element formulation

Formulation (6.7) is now discretized on an unfitted mesh. Define as in Section 3.5 two active background meshes $\mathcal{T}_{h,i}$ and $\mathcal{T}_{h,e}$. In contrast to the single-dimensional formulation we now also have an unknown I_m defined on Γ. In order to discretize I_m we define the mesh consisting of the elements that are cut by Γ,

$$\mathcal{T}_{h,\Gamma} = \{T \in \mathcal{T}_{h,i} \cup \mathcal{T}_{h,e} | T \cap \Gamma \neq \emptyset\},$$

which is the same as we did to discretize the ODE system in Section 4.5. Define the corresponding set of the interior faces by

$$\mathcal{F}_{h,\Gamma} = \{F = T^+ \cap T^- | T^+, T^- \in \mathcal{T}_{h,\Gamma}\}.$$

Figure 7 illustrates the different domains.

As finite element spaces we employ first-order continuous piecewise linear elements for the potentials and constant linear elements for the current,

$$V_{h,i} = \mathbb{P}_1^c(\mathcal{T}_{h,i}), \quad V_{h,e} = \{v \in \mathbb{P}_1^c(\mathcal{T}_{h,e}) : v|_{\partial\Omega} = 0\}, \quad Q_h = \mathbb{P}_0(\mathcal{T}_{h,\Gamma}),$$

and let $V_h = V_{h,i} \times V_{h,e}$. Notice here that the finite element space for the current is defined on the whole $\mathcal{T}_{h,\Gamma}$. Also, we do not have the same average zero requirement for the intracellular space as we had for the continuous version. The coercivity problem will instead be taken care of by the definition of the norm which will be given later. The unfitted multi-dimensional

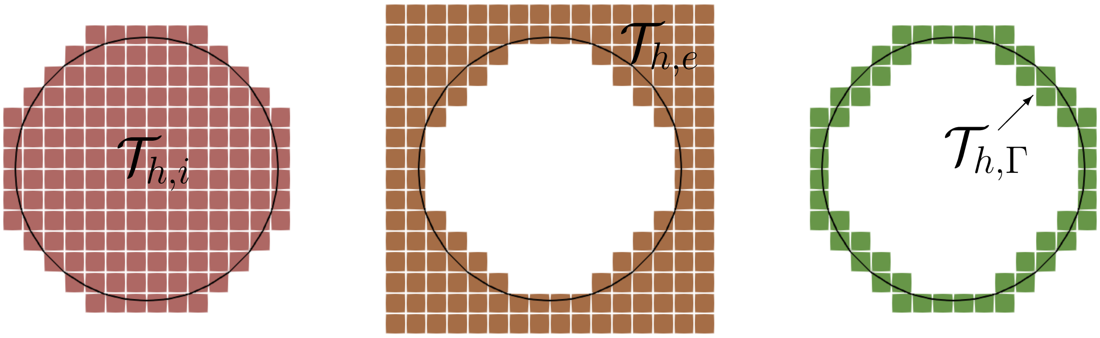

Figure 7: Illustration of the computational domains for the multi-dimensional discretization with the (left) intracellular, (middle) extracellular and (right) interface computational domains.

finite element formulation of the EMI PDEs is then: find $(u_h, \lambda_h) \in V_h \times Q_h$ such that

$$a(u_h, v_h) + b(v_h, \lambda_h) = 0, \qquad \forall v_h \in V_h, \tag{6.9a}$$

$$b(u_h, \mu_h) - \frac{\Delta t}{C_m} c(\lambda_h, \mu_h) = g(\mu_h), \quad \forall \mu \in Q_h, \tag{6.9b}$$

with total bilinear form

$$A(u_h, \lambda_h; v_h, \mu_h) = a(u_h, v_h) + b(v_h, \lambda_h) + b(u_h, \mu_h) - \frac{\Delta t}{C_m} c(\lambda_h, \mu_h).$$

We now add two stabilization terms, the first is the same ghost penalty as in Chapter 5, $g_h(\cdot, \cdot)$ defined in (5.22), and the second is a stabilization term for the multipliers defined by

$$s_h(\lambda_h, \mu_h) = \phi \sum_{F \in \mathcal{F}_{h,\Gamma}} ([\lambda_h], [\mu_h])_F,$$

where

$$\phi = \max\left\{\frac{\Delta t}{C_m}, h\right\},$$

and the corresponding semi-norm is defined by

$$|\mu_h|_{s_h}^2 = s_h(\mu_h, \mu_h).$$

The CutFEM multi-dimensional CutFEM formulation is defined by: find $(u_h, \lambda_h) \in V_h \times Q_h$ such that

$$A_h(u_h, \lambda_h, v_h, \mu_h) := A(u_h, \lambda_h, v_h, \mu_h) + g_h(u_h, v_h) - s_h(\lambda_h, \mu_h) = f(\mu_h), \tag{6.10}$$

for all $(v_h, \mu_h) \in V_h \times Q_h$. For (6.10), the ghost penalty term g_h is as in the single-dimensional case, only needed to stabilized the associated condition number. The role of the stabilization term for the multipliers s_h, depends on the relationship between Δt and h. In the case $\frac{\Delta t}{C_m} \leqslant h$, s_h is needed in order to have an inf-sup stable discrete formulation, which we will show later. In the case $\frac{\Delta t}{C_m} \geqslant h$, s_h is only needed to stabilize the condition numbers.

For the further analysis, we define the discrete norms,

$$\begin{aligned} |||(v_h, \mu_h)|||_\phi^2 &= \sigma_e \|\nabla v_{h,e}\|_{\Omega_e}^2 + \sigma_i \|\nabla v_{h,i}\|_{\Omega_i}^2 + \phi^{-1} \|v_{h,i} - v_{h,e}\|_\Gamma^2 + \phi \|\mu_h\|_\Gamma^2, \\ |||(v_h, \mu_h)|||_{A_h}^2 &= |||(v_h, \mu_h)|||_\phi^2 + |v_h|_{g_h}^2 + |\mu_h|_{s_h}^2. \end{aligned}$$

An application of Cauchy-Schwarz immediately shows that the total bilinear form is bounded.

Lemma 6.5 (Boundedness in discrete norm)**.** *For $u, v \in V$ and $\mu, \lambda \in Q$ it holds that*

$$A(u, \lambda; v, \mu) \lesssim |||(u, \lambda)|||_{\phi} |||(v, \mu)|||_{\phi}.$$

In the rest of this section, we will show that the discrete formulation satisfies a discrete inf-sup condition, and derive an a priori error estimate. We will follow the presentation in [19], which analyses an unfitted stabilized formulation of the Poisson boundary value problem with Lagrange multipliers. Before analyzing the discrete formulation, we first define a patchwise projection which will play an important role in proving the inf-sup condition.

6.4.1 Creation of a patchwise projection

This presentation of how we define the patches and patchwise projection is based on [19] and [17]. Define

$$W_{\Gamma,j} = \{T \in \mathcal{T}_{h,j} : T \cap \mathcal{T}_{h,\Gamma} \neq \emptyset\},$$

for $j = i, e$. $W_{\Gamma,j}$ then consists of all elements that are cut by Γ and all elements sharing a face or a vertex with the elements that are cut. The elements of each $W_{\Gamma,j}$ are now divided into n patches $\{\mathcal{P}_k^j\}_{k=1}^n$. Let each patch contain basis functions such that a patch function $0 \leqslant \phi_k^j \leqslant 1$ is zero on the interior patch boundary $\partial\mathcal{P}_k^j \setminus \partial W_{\Gamma,j}$, and take the value 1 on at least one face cut by Γ, can be constructed. Each $\mathcal{P}_k^j$ with h_p : diam$(\mathcal{P}_k^j)$ can be constructed such that

- $\exists c_1, c_2 > 0$ such that $c_1 h \leqslant h_{\mathcal{P}} \leqslant c_2 h$.
- $\exists c_1, c_2 > 0$ such that $c_1 h \leqslant \int_{\Gamma\cap\mathcal{P}_k^j} \phi_k^j \ \mathrm{d}s \leqslant c_2 h$.
- $\exists c_1, c_2 > 0$ such that $c_1 h^{-1} \leqslant \nabla\phi_k \ \mathrm{d}s \leqslant c_2 h^{-1}$.

Define on the patches a space of piecewise constant function on Γ,

$$X_h^j = \{\lambda_h : \lambda_h \mid_{\mathcal{P}_k^j} \in \mathbb{P}_0(\mathcal{P}_k^j)\}.$$

The patchwise projection $\pi_{\mathcal{P}}^j u_h \in X_h^j$ is then constructed by

$$\pi_{\mathcal{P}}^j u_{h,j} \mid_{\mathcal{P}_k^j} = \frac{1}{|\Gamma \cap P_k^j|} \int_{\Gamma\cap P_k^j} u_{h,j} \ \mathrm{d}s.$$

The following trace inequality for the projection is proven in [17].

Lemma 6.6. *For $u_k \in H^1(\mathcal{P}_k^j)$, the following holds*

$$\|u_k - \pi_{\mathcal{P}}^j u_k\|_{\Gamma\cap\mathcal{P}_k^j} \lesssim h^{\frac{1}{2}} \|\nabla u_k\|_{\mathcal{P}_k^j}.$$

We can now show the following results for the projection.

Lemma 6.7. *For $u_h \in V_h$ it holds that*

$$\|u_{h,i} - u_{h,e}\|_\Gamma^2 \leqslant \|\pi_\mathcal{P}^i u_{h,i} - \pi_\mathcal{P}^e u_{h,e}\|_\Gamma^2 + Ch(\|\nabla u_{h,e}\|_{\Omega_e}^2 + \|\nabla u_{h,i}\|_{\Omega_i}^2), \tag{6.11}$$

$$\|\pi_\mathcal{P}^i u_{h,i} - \pi_\mathcal{P}^e u_{h,e}\|_\Gamma^2 \lesssim h(\|\nabla u_{h,e}\|_{\Omega_e}^2 + \|\nabla u_{h,i}\|_{\Omega_i}^2) + \|u_{h,i} - u_{h,e}\|_\Gamma^2. \tag{6.12}$$

Proof. Combining the triangle inequality and Lemma 6.6 yields,

$$\begin{aligned}\|u_{h,i} - u_{h,e}\|_\Gamma^2 &\leqslant \sum_{k=1}^n \Big(\|u_{h,i} - \pi_\mathcal{P}^j u_{h,i}\|_{\Gamma\cap\mathcal{P}_k^i}^2 + \|u_{h,e} - \pi_\mathcal{P}^j u_{h,e}\|_{\Gamma\cap\mathcal{P}_k^e}^2\Big) + \|\pi_\mathcal{P}^i u_{h,i} - \pi_\mathcal{P}^e u_{h,e}\|_\Gamma^2 \\ &\leqslant C\sum_{k=1}^n \Big(h\|\nabla u_{h,i}\|_{\mathcal{P}_k^i} + h\|\nabla u_{h,e}\|_{\mathcal{P}_k^e}\Big) + \|\pi_\mathcal{P}^i u_{h,i} - \pi_\mathcal{P}^e u_{h,e}\|_\Gamma^2.\end{aligned}$$

Inequality (6.11) then follows since there are only a bounded number of macro patches $\mathcal{P}_k^j$. In a similar manner (6.12) can be proven. □

From the construction of the patches the following approximation results from [19] holds.

Lemma 6.8 ([19], p.2682)**.** *For $\lambda_h \in Q_h$ it holds that*

$$\inf_{c_h \in X_h^j} h\|(\lambda_h - c_h)\|_{\Gamma\cap\mathcal{P}_k^j}^2 \lesssim s_h(\lambda_h, \lambda_h).$$

Lemma 6.9 ([19], p.2683)**.** *For $u_h \in V_h$ it holds that*

$$\|\pi_\mathcal{P}^i u_{h,i} - \pi_\mathcal{P}^e u_{h,e}\|_{s_h}^2 \lesssim \phi\|\pi_\mathcal{P}^i u_{h,i} - \pi_\mathcal{P}^e u_{h,e}\|_\Gamma^2.$$

6.4.2 The discrete inf-sup condition

With the projection defined, we are ready to show that the formulation satisfies a discrete inf-sup condition, one of the main results of Chapter 6.

Theorem 6.10 (Discrete inf-sup condition)**.** *For all $(u_h, \lambda_h) \in V_h \times Q_h$ there holds*

$$|||(u_h, \lambda_h)|||_{A_h} \lesssim \sup_{(v_h,\mu_h)\in V_h\times Q_h} \frac{A_h(u_h, \lambda_h; v_h, \mu_h)}{|||(v_h, \mu_h)|||_{A_h}}.$$

Proof. In order to prove the Theorem, we need to construct a test function (z, η) such that

$$A_h(u_h, \lambda_h; z, \eta) \gtrsim |||(u_h, \lambda_h)|||_{A_h} |||(z, \eta)|||_{A_h}.$$

The first step is to test with the following

$$A(u_h, \lambda_h; u_h, -\lambda_h) = \sigma_e \|\nabla u_{h,e}\|^2_{\Omega_e} + \sigma_i \|\nabla u_{h,i}\|^2_{\Omega_i} + \frac{\Delta t}{C_m} \|\lambda_h\|^2_{\Gamma}. \tag{6.13}$$

Next, we need construct the part which controls $u_{h,i} - u_{h,e}$. Inserting $\bar{\mu} = \frac{1}{\phi}(\pi^i_{\mathcal{P}} u_{h,i} - \pi^e_{\mathcal{P}} u_{h,e})$ as a test function in the stabilized bilinear form gives three terms,

$$A_h(u_h, \lambda_h; 0, \bar{\mu}) = (u_{h,i} - u_{h,e}, \bar{\mu})_\Gamma - \frac{\Delta t}{C_m}(\lambda_h, \bar{\mu})_\Gamma - s_h(\lambda, \bar{\mu}). \tag{6.14}$$

Since $\pi^j_{\mathcal{P}}$ is a projection the first term can be written as

$$(u_{h,i} - u_{h,e}, \bar{\mu})_\Gamma = \frac{1}{\phi} \|\pi^i_{\mathcal{P}} u_{h,i} - \pi^e_{\mathcal{P}} u_{h,e}\|^2_\Gamma. \tag{6.15}$$

For the second term, we employ Cauchy-Schwarz and Young's Inequality,

$$\frac{\Delta t}{C_m}(\lambda_h, \bar{\mu})_\Gamma \leqslant \|\lambda_h\|_\Gamma \|\pi^i_{\mathcal{P}} u_{h,i} - \pi^e_{\mathcal{P}} u_{h,e}\|_\Gamma \leqslant 2\phi \|\lambda_h\|^2_\Gamma - \frac{1}{2\phi} \|\pi^i_{\mathcal{P}} u_{h,i} - \pi^e_{\mathcal{P}} u_{h,e}\|^2_\Gamma. \tag{6.16}$$

By applying an ϵ-scaled Young's Inequality and Lemma 6.9 the third term can be bounded.

$$\begin{aligned} s_h(\lambda, \bar{\mu}) &\leqslant s_h(\lambda_h, \lambda_h)^{1/2} s_h(\bar{\mu}, \bar{\mu})^{1/2} \leqslant \frac{1}{\epsilon} s_h(\lambda_h, \lambda_h) + \frac{\epsilon}{4} s_h(\bar{\mu}, \bar{\mu}) && (6.17) \\ &\leqslant \frac{1}{\epsilon} s_h(\lambda_h, \lambda_h) + \frac{c_1 \epsilon}{4\phi} \|\pi^i_{\mathcal{P}} u_{h,i} - \pi^e_{\mathcal{P}} u_{h,e}\|^2_\Gamma. && (6.18) \end{aligned}$$

Now, inserting (6.15), (6.16) and (6.18) into (6.14) and applying Lemma 6.7 gives

$$\begin{aligned} &A_h(u_h, \lambda_h; 0, \bar{\mu}) = (u_{h,i} - u_{h,e}, \bar{\mu})_\Gamma - \frac{\Delta t}{C_m}(\lambda_h, \bar{\mu})_\Gamma - s_h(\lambda, \bar{\mu}) \\ &\geqslant \frac{1}{\phi}\left(\frac{1}{2} - \frac{c_1\epsilon}{4}\right) \|\pi^i_{\mathcal{P}} u_{h,i} - \pi^e_{\mathcal{P}} u_{h,e}\|^2_\Gamma - 2\phi\|\lambda_h\|^2_\Gamma - \frac{1}{\epsilon} s_h(\lambda, \lambda) \\ &\geqslant \frac{1}{\phi}\left(\frac{1}{2} - \frac{c_1\epsilon}{4}\right)\left(\|u_{h,i} - u_{h,e}\|^2_\Gamma - c_2 h \|\nabla u_{h,e}\|^2_{\Omega_e} - c_2 h \|\nabla u_{h,i}\|^2_{\Omega_i}\right) - 2\phi\|\lambda_h\|^2_\Gamma - \frac{1}{\epsilon} s_h(\lambda, \lambda) \\ &\geqslant \left(\frac{1}{2} - \frac{c_1\epsilon}{4}\right)\left(\frac{1}{\phi}\|u_{h,i} - u_{h,e}\|^2_\Gamma - c_2 \|\nabla u_{h,e}\|^2_{\Omega_e} - c_2 \|\nabla u_{h,i}\|^2_{\Omega_i}\right) - 2\phi\|\lambda_h\|^2_\Gamma - \frac{1}{\epsilon} s_h(\lambda, \lambda). \end{aligned}$$

For the case $\frac{\Delta t}{C_m} \geqslant h$, we have now performed the two steps needed to construct the test function. However for the case $\frac{\Delta t}{C_m} \leqslant h$ a third step is needed. We therefore look at the two cases separately from here.

Case $\frac{\Delta t}{C_m} \geqslant h$. Let $(z,\eta) = (u_h, -\lambda_h + \delta\bar{\mu})$. By a suitable choice of $\delta > 0$, which depends on σ_e and σ_i, it follows that

$$\begin{aligned} A_h(u_h,\lambda_h;z,\eta) &= A(u_h,\lambda_h;u_h,\lambda_h) + g_h(u_h,u_h) + s_h(\lambda_h,\lambda_h) + \delta A_h(u_h,\lambda_h;0,\bar{\mu}) \\ &\gtrsim |||(u_h,\lambda_h)|||_{A_h}^2. \end{aligned}$$

The remaining part is show that

$$|||(u_h,\lambda_h)|||_{A_h} \gtrsim |||(z,\eta)|||_{A_h},$$

which follows from the definition of the $|||(\cdot,\cdot)|||_{A_h}$-norm, and a combination of the triangle inequality, Lemma 6.7 and (6.18).

$$\begin{aligned} |||(z,\eta)|||_{A_h}^2 &\lesssim |||(u_h,\lambda_h)|||_{A_h}^2 + \frac{\Delta t}{C_m}\|-\lambda_h + \delta\bar{\mu}\|_\Gamma^2 + |-\lambda_h + \delta\bar{\mu}|_{s_h}^2 \\ &\lesssim |||(u_h,\lambda_h)|||_{A_h}^2 + \frac{\Delta t}{C_m}\|\lambda_h\|_\Gamma^2 + \delta\left(\frac{C_m}{2\Delta t}\|\pi_{\mathcal{P}}^i u_{h,i} - \pi_{\mathcal{P}}^e u_{h,e}\|_\Gamma^2 + 2|\lambda_h|_{s_h}^2\right) \\ &\lesssim |||(u_h,\lambda_h)|||_{A_h}^2 + \frac{\delta h C_m}{2\Delta t}(\|\nabla u_{h,e}\|_{\Omega_e}^2 + \|\nabla u_{h,i}\|_{\Omega_i}^2) + \frac{C_m}{2\Delta t}\|u_{h,i} - u_{h,e}\|_\Gamma^2 \\ &\lesssim |||(u_h,\lambda_h)|||_{A_h}^2. \end{aligned}$$

Case $\frac{\Delta t}{C_m} \leqslant h$. Unlike from the first case, (6.13) is now not enough to control the norm for λ_h. We therefore need a third part to construct the test function. This will follow [17], and is based on the patches $\mathcal{P}_k^i$. Define first $\xi_h^i \in V_{h,i}$ such that

- $\xi_h^i\,|_{\Omega\setminus W_{\Gamma,i}} = 0$
- $\int_{\Gamma\cap\mathcal{P}_k^i} \xi_h^i \,\mathrm{d}s = \int_{\Gamma\cap\mathcal{P}_k^i} h_{\mathcal{P}}\lambda_h \,\mathrm{d}s$
- $\xi_h^i\,|_{T_c} = 0$ where T_c denotes an element containing only a corner of $W_{\Gamma,i}$.

Now, define $\xi_h = (\xi_h^i, 0)$. From construction ξ_i is zero on the boundary of $W_{\Gamma,i}$, leading to

$$\|\nabla\xi_h\|_{W_{\Gamma,i}}^2 \lesssim \frac{1}{h}\|\xi_h\|_\Gamma^2 \lesssim h\|\lambda_h\|_\Gamma^2. \tag{6.19}$$

With ξ_h as a test function we have the following for the bilinear form b by using Cauchy-Schwarz, an ϵ-scaled Young's inequality, inequality (6.19) and Lemma 6.8,

$$\begin{aligned} b(\xi_h,\lambda_h) &= (\xi_h^i,\lambda_h)_\Gamma \\ &= (\xi_h^i, \lambda_h - \pi_{\mathcal{P}}^i\lambda_h) + (\xi_h^i, \pi_{\mathcal{P}}^i\lambda_h) \\ &\geqslant -\|\xi_h^i\|_\Gamma\|\lambda_h - \pi_{\mathcal{P}}^i\lambda_h\|_\Gamma + c_1 h\|\pi_{\mathcal{P}}^i\lambda_h\|_\Gamma^2 \\ &\geqslant -\frac{\epsilon}{4h}\|\xi_h^i\|_\Gamma^2 - \frac{h}{\epsilon}\|\lambda_h - \pi_{\mathcal{P}}^i\lambda_h\|_\Gamma^2 + c_1 h\|\lambda_h\|_\Gamma^2 \\ &\geqslant h(c_1 - \frac{c_2\epsilon}{4})\|\lambda_h\|_\Gamma^2 - \frac{c_3}{\epsilon}s_h(\lambda_h,\lambda_h). \end{aligned}$$

For the bilinear form a, Cauchy-Schwarz, an ϵ-scaled Young's inequality, and (6.19) gives

$$\begin{aligned} a(u_h, \xi_h) &\geqslant -\sigma_i \|\nabla u_{h,i}\|_{\Omega_i} \|\nabla \xi_h\|_{\Omega_i}. \\ &\geqslant -\frac{\sigma_i}{\epsilon}\|\nabla u_{h,i}\|^2_{\Omega_i} - \frac{\epsilon}{4}\|\nabla \xi_h\|^2_{W^i_\Gamma}. \\ &\geqslant -\frac{\sigma_i}{\epsilon}\|\nabla u_{h,i}\|^2_{\Omega_i} - \frac{c_4\epsilon}{4} h \|\lambda_h\|^2_\Gamma. \end{aligned}$$

Now, let $(z_2, \eta_2) = (u_h + \delta_1 \xi_h, -\lambda_h + \delta_2 \bar{\mu})$. For a suitable choice of δ_1 and δ_2 we have that

$$A_h(u_h, \lambda_h; z_2, \eta_2) \gtrsim |||(u_h, \lambda_h)|||^2_{A_h}.$$

Finally, the last part is to show that

$$|||(u_h, \lambda_h)|||_{A_h} \gtrsim |||(z_2, \eta_2)|||_{A_h}.$$

which is established with the $|||(\cdot, \cdot)|||_{A_h}$-norm combined with the following estimate for the ghost penalty, shown with the use of inequality (6.19),

$$|\xi_h|_{g_h} = \gamma_m h^3 \|[\partial_n \xi_h]\|^2_{\mathcal{F}_{h,i}} \lesssim h^2 \|\nabla \xi_h\|^2_{W_{h,\Gamma}} \lesssim h^3 \|\lambda\|^2_\Gamma,$$

the triangle inequality, Lemma 6.7, and inequality (6.19),

$$\begin{aligned} |||(z_2, \eta_2)|||^2_{A_h} &\leqslant |||(u_h, \lambda_h)|||^2_{A_h} + \delta_1 \sigma_i \|\nabla \xi^i_h\|^2_{W^i_\Gamma} + \frac{\delta_1}{h}\|\xi^i_h\|^2_\Gamma + \delta_1 |\xi_h|^2_{g_h} + h\delta_2 \|\bar{\mu}\|^2_\Gamma + \delta_2 |\bar{\mu}|^2_{s_h} \\ &\lesssim |||(u_h, \lambda_h)|||^2_{A_h} + h\delta_1(\sigma_i + C)\|\lambda_h\|^2_\Gamma + \frac{\delta_2}{2h}\|\pi^i_{\mathcal{P}} u_{h,i} - \pi^e_{\mathcal{P}} u_{h,e}\|^2_\Gamma \\ &\lesssim |||(u_h, \lambda_h)|||^2_{A_h} + \delta_2(\|\nabla u_{h,e}\|^2_{\Omega_e} + \|\nabla u_{h,i}\|^2_{\Omega_i}) + \frac{\delta_2}{h}\|u_{h,i} - u_{h,e}\|^2_\Gamma \\ &\lesssim |||(u_h, \lambda_h)|||^2_{A_h}. \end{aligned}$$

□

6.4.3 A priori error estimate

With the inf-sup condition in place, we want to show that we an a priori error estimate. First, we state that the weak formulation satisfies a weak Galerkin orthogonality.

Lemma 6.11 (Weak Galerkin orthogonality)**.** *Let $u \in H^s(\Omega_i) \times H^s(\Omega_e)$, $s \geqslant 2$ be the solution to the spatial EMI problem* (5.1)*, set $\lambda = \sigma_e \nabla u_e \cdot \boldsymbol{n_e}$, and let $(u_h, \lambda_h) \in V_h \times Q_h$ be the solution to the multi-dimensional finite element formulation* (6.9)*. Then*

$$A(u - u_h, \lambda - \lambda_h; v_h, \mu_h) = g_h(u_h, v_h) - s_h(\lambda_h, \mu_h) \quad \forall (v_h, \mu_h) \in V_h \times Q_h.$$

Next, we can show that the discrete solution satisfy a quasi-best approximation property.

Theorem 6.12. *Let $u \in H^s(\Omega_i) \times H^s(\Omega_e)$, $s \geqslant 2$ be the solution to the spatial EMI problem* (5.1)*, $\lambda = \sigma_e \nabla u_e \cdot \boldsymbol{n_e}$, and let $(u_h, \lambda_h) \in V_h \times Q_h$ be the solution to the multi-dimensional finite element formulation* (6.9)*. Then the error $(u - u_h, \lambda - \lambda_h)$ satisfies*

$$|||(u - u_h, \lambda - \lambda_h)|||_{A_h} \lesssim \sup_{(v_h,\mu_h) \in V_h \times Q_h} \Big(|||(u - v_h, \lambda - \mu_h)|||_\phi + g_h(v_h, v_h)^{\frac{1}{2}} + s_h(\mu_h, \mu_h)^{\frac{1}{2}} \Big).$$

Proof. First, divide the error into the interpolation error and the discrete error by employing the triangle inequality,

$$|||(u - u_h, \lambda - \lambda_h)|||_{A_h} \leqslant |||(u - v_h, \lambda - \mu_h)|||_{A_h} + |||(u_h - v_h, \lambda_h - \mu_h)|||_{A_h}. \tag{6.20}$$

The discrete error can then be bounded by applying the inf-sup condition 6.10 and the weak Galerkin orthogonality 6.11,

$$\begin{aligned} &|||(v_h - u_h, \lambda_h - \mu_h)|||_{A_h} \\ &\lesssim \sup_{(\rho_h,\nu_h) \in V_h \times Q_h} \frac{A_h(v_h - u_h, \lambda_h - \mu_h; \rho_h, \nu_h)}{|||(\rho_h, \nu_h)|||_{A_h}} \\ &= \sup_{(\rho_h,\nu_h) \in V_h \times Q_h} \frac{A(v_h - u, \lambda_h - \mu_h; \rho_h, \mu_h) + g_h(v_h, \rho_h) - s_h(\mu_h, \nu_h)}{|||(\rho_h, \nu_h)|||_{A_h}}. \end{aligned}$$

The result now follows from the boundedness of bilinear form 6.5. □

In order to show an a priori estimate in the energy norm, we follow [19] and first consider a related problem to prove a bound for an approximation operator operating on λ. First, immerse the mesh $\mathcal{T}_{h,i}$ in a larger subdomain Ω_T, such that $\text{dist}(\partial\Omega_T, \Gamma) = \mathcal{O}(1)$. Then consider the problem, find $w \in H_0^1(\Omega_T)$, $\mu \in H^{-\frac{1}{2}}(\Gamma)$ such that

$$(\nabla w, \nabla v)_{\Omega_T} + (\mu, v)_\Gamma = 0, \tag{6.21a}$$

$$(w, \lambda)_\Gamma = (\lambda, y)_\Gamma, \tag{6.21b}$$

for all $v \in H_0^1(\Omega_T)$, $y \in H^{-\frac{1}{2}}(\Gamma)$, where $\lambda \in H^{\frac{1}{2}}(\Gamma)$. Thanks to Theorem 6.2 this problem is well-posed, and the solution satisfies the a priori bound

$$\|\nabla w\|_{\Omega_T} + \|\mu\|_{-\frac{1}{2},\Gamma} \lesssim \|\lambda\|_{\frac{1}{2},\Gamma}. \tag{6.22}$$

Next, we define a local projection $\pi_L : L^2(\mathcal{T}_{h,\Gamma}) \to \mathbb{P}_0(\mathcal{T}_{h,\Gamma})$ on piecewise constants satisfying

$$\int_T \pi_L w \,|_T \ \mathrm{d}x = \int_T w \ \mathrm{d}x,$$

for all $T \in \mathcal{T}_{h,\Gamma}$. Then we can prove the following approximation properties.

Lemma 6.13. *Assume w solves* (6.21)*. Then we have that*

$$\|\lambda - \pi_L w\|_\Gamma \lesssim h^{\frac{1}{2}} \|\lambda\|_{\frac{1}{2},\Gamma}, \tag{6.23}$$

$$s_h(\pi_L w, \pi_L w)^{\frac{1}{2}} \lesssim h^{\frac{1}{2}} \phi^{\frac{1}{2}} \|\lambda\|_{\frac{1}{2},\Gamma}. \tag{6.24}$$

Proof. For (6.23), we begin by noting that thanks to (6.21b), $w = \lambda$ on Γ, and utilize the local trace inequality (5.26) to obtain

$$\begin{aligned} \|\lambda - \pi_L w\|_\Gamma^2 &= \|w - \pi_L w\|_\Gamma^2 \\ &\lesssim \sum_{T \in T_h^\Gamma} h^{-1}\|w - \pi_L w\|_T^2 + h\|\nabla w\|_T^2 \\ &\lesssim h\|\nabla w\|^2_{\mathcal{T}_{h,\Gamma}}, \end{aligned}$$

where the last line follows from $\|w - \pi_L w\|_T \lesssim h\|\nabla w\|_T$, see [19]. Inequality (6.23) then follows directly from (6.22). To prove (6.24), notice that since $w \in H^1(\Omega_i)$, $s_h(w, w) = 0$. We can therefore write

$$s_h(\pi_L w, \pi_L w) = s_h(w - \pi_L w, w - \pi_L w),$$

and the estimate follows similarly to (6.23),

$$\begin{aligned} s_h(w - \pi_L w, w - \pi_L w) &= \phi\|[w - \pi_L w]\|^2_{\mathcal{F}_{h,\Gamma}} \\ &\lesssim \phi \sum_{T \in \mathcal{T}_{h,\Gamma}} h^{-1}\|w - \pi_L w\|_T^2 + h\|\nabla w\|_T^2 \\ &\lesssim \phi h\|\nabla w\|^2_{\mathcal{T}_{h,\Gamma}} \lesssim \phi h\|\lambda\|^2_{\frac{1}{2},\Gamma}. \qquad \square \end{aligned}$$

Next, we define approximation operator for u, $\pi_h^e u$, to be as (5.29).

Lemma 6.14. *Assume that* $u \in H^s(\Omega_i) \times H^s(\Omega_e)$, $s \geqslant 2$, *that* w *solves problem* (6.21), *and set* $\lambda = \sigma_e \nabla u_e \cdot \boldsymbol{n_e}$. *Then the following interpolation estimate holds*

$$|||(u - \pi_h^e u, \lambda - \pi_L w)|||_\phi \lesssim h\big(\max\{\sigma_i, \sigma_e\} + h\phi^{-1} + h^{-1}\phi\big)^{\frac{1}{2}}\|u\|_{2,\Omega_i \cup \Omega_e}.$$

Proof. First, we look at the part of $|||(u - \pi_h^e u, \lambda - \pi_L w)|||_\phi$ related to the first argument, which can be bounded with a ϕ scaled version of the approximation result in (5.33),

$$\|\nabla(u - \pi_h^e u)\|^2_{\Omega_i \cup \Omega_e} + \phi^{-1}\|[u - \pi_h^e]\|_\Gamma^2 \lesssim h^2\big(\max\{\sigma_i, \sigma_e\} + h\phi^{-1}\big)\|u\|^2_{2,\Omega_i \cup \Omega_e}.$$

For the part related to the second argument, we apply Lemma 6.13 and that $\|\lambda\|_\Gamma \lesssim \|u\|_{2,\Omega_i \cup \Omega_e}$, yielding

$$\phi\|\lambda - \pi_L w\|_\Gamma^2 \lesssim h\phi\|\lambda\|_\Gamma^2 \lesssim h\phi\|u\|_{2,\Omega_i \cup \Omega_e}. \qquad \square$$

If we now choose $v_h = \pi_h^e u$ and $\mu_h = \pi_L w$ in Theorem 6.12, and combine the results in Lemmas 6.14, 6.13, and 5.16, we end up with an a priori error estimate in the energy norm.

Theorem 6.15 (A priori error estimate in energy norm)**.** *Let* $u \in H^s(\Omega_i) \times H^s(\Omega_e)$*,* $s \geqslant 2$ *be the solution to the spatial EMI problem* (5.1)*, set* $\lambda = \sigma_e \nabla u_e \cdot \boldsymbol{n_e}$*, and let* $(u_h, \lambda_h) \in V_h \times Q_h$ *be the solution to the multi-dimensional finite element formulation* (6.9)*. Then, the error* $(u - u_h, \lambda - \lambda_h)$ *satisfies*

$$|||(u - u_h, \lambda - \lambda_h)|||_{A_h} \lesssim h\big(\max\{\sigma_i, \sigma_e\} + h\phi^{-1} + h^{-1}\phi + 1\big)^{\frac{1}{2}} \|u\|_{2,\Omega_i \cup \Omega_e}.$$

We see from the Theorem above that we have an optimal error estimate only in the case where $\frac{\Delta t}{C_m} \leqslant h$. This is opposite than what was the situation for the single-dimensional formulation in Chapter 5.

Chapter 7

Implementation and numerical experiments

The operator splitting scheme introduced in Section 4.2 divided the EMI problem into a PDE and an ODE step. In this chapter, we first present the implementation of the single-dimensional and multi-dimensional discretized formulations for the PDE step. Next, we conduct numerical experiments to corroborate the theoretical results concerning convergence order and condition numbers derived in Chapters 5 and 6. Afterwards, we solve the EMI PDEs on more realistic geometries, which are only represented by a lower-dimensional surface mesh.

We also present numerical experiments for the unfitted ODE solver presented in Section 4.5 before considering the complete EMI model. In the first series of experiments, we consider the passive membrane model where only the PDE step is needed. With this model, both a convergence study and a simulation are conducted. Finally, an active membrane model is considered where both steps of the splitting scheme needs to be solved. For the active model, two convergence studies are performed, before we conclude with a simulation with the FitzHugh-Nagumo membrane model.

7.1 Implementation

All proposed numerical methods in this work are implemented using the Julia [11] based finite element framework Gridap [8]. In addition, the extension package GridapEmbedded is used which provides all CutFEM related functionality on top of Gridap. Visualizations are made using the visualization software ParaView [3]. Before we turn to the numerical experiments we first explain how the CutFEM single-dimensional formulation is implemented and how this can be extended to the multi-dimensional formulation.

The first part consists of defining the total background mesh. Here, we define a computational mesh consisting of $N \times N$ squares in the total domain $\Omega = [-1, 1]^2$:

```
domain = (-1,1,-1,1)
partition = (N,N)
model = CartesianDiscreteModel(domain,partition)
```

The total domain is defined as an union of the intracellular and the extracellular domains. To define each domain we define a level set function φ and let the domains be

$$\Omega_i = \{(x, y) \in R^2 \mid \varphi(x, y) < 0\}, \quad \Omega_e = \Omega \setminus \Omega_i.$$

In Gridap we can define the level set function as below, and let this function cut the total computational domain.

```
φ = AnalyticalGeometry(x->x[1]^2+x[2]^2-0.8^2)
cutgeo = cut(model,φ)
```

Note that some geometries such as the circle we have defined here, are already predefined in GridapEmbedded. However, since we are also going to use more complex geometries, we write the expression for the geometry manually using the more flexible analytical geometry constructor.

In order to define test and trial spaces, the active meshes corresponding to $\mathcal{T}_{h,i}$ and $\mathcal{T}_{h,e}$ in Section 5.4 are needed. The commands "ACTIVE_IN" and "ACTIVE_OUT" give the mesh corresponding to the inside and outside of the cut made by φ.

```
Ωe_act = Triangulation(cutgeo,ACTIVE_OUT)
Ωi_act = Triangulation(cutgeo,ACTIVE_IN)
```

Figure 7 shows both of the active background meshes. Next, we define the integration meshes, which should represent the geometries of the intracellular and extracellular domains. The commands "PHYSICAL_IN" and "PHYSICAL_OUT" let us define intracellular as the inside of the cut between φ and the total background mesh, and the extracellular as the outside of the cut.

```
Ωe = Triangulation(cutgeo,PHYSICAL_OUT)
Ωi =  Triangulation(cutgeo,PHYSICAL_IN)
```

Figure 8 illustrates the difference between the active mesh and the integration mesh for the intracellular domain. The interpolation mesh can consist of highly intracellular elements, but these are only used with quadrature rules for integration.

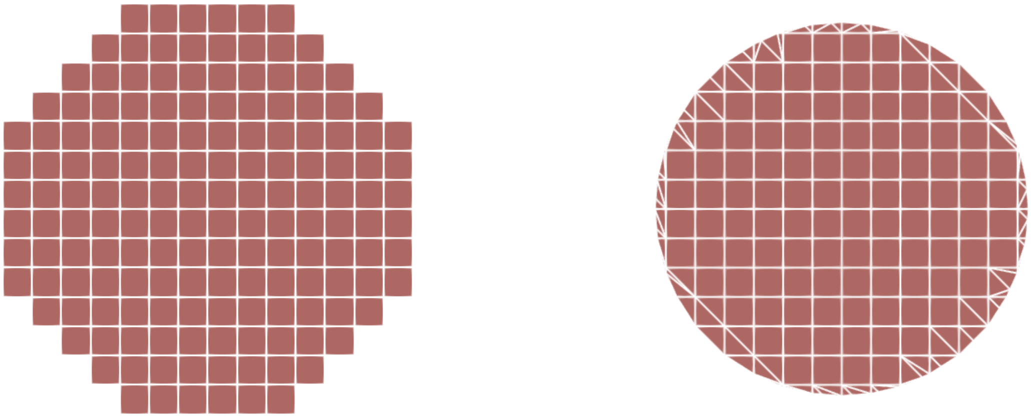

Figure 8: The active mesh (left) and the integration mesh (right) for the intracellular domain.

The next step is to let Γ be defined as the boundary between the domains, also represented as an integration mesh. In addition we define the corresponding Lebesgue measure for the integration meshes, with the degree parameter giving the order of the quadrature role.

```
Γ = EmbeddedBoundary(cutgeo)
dΩi = Measure(Ωi,degree)
dΩe = Measure(Ωe,degree)
dΓ = Measure(Γ,degree)
```

Now, we define the ghost facets that will be we needed to define the stabilized weak formulation, by using GridapEmbedded's GhostSkeleton function, and the corresponding normal vectors and measures.

```
Γgi = GhostSkeleton(cutgeo,CUT_IN)
Γge = GhostSkeleton(cutgeo,CUT_OUT)
n_Γge = get_normal_vector(Γge)
n_Γgi = get_normal_vector(Γgi)
dΓge = Measure(Γge,degree)
dΓgi = Measure(Γgi,degree)
```

Figure 9 shows each of the domains Ω_i and Ω_e together with the corresponding ghost faces. To define the finite element spaces, we start with the test spaces:

```
Ve = TestFESpace(Ωe_act,ReferenceFE(lagrangian,Float64,order),conformity=:H1,
     dirichlet_tags="boundary")
Vi = TestFESpace(Ωi_act,ReferenceFE(lagrangian,Float64,order),conformity=:H1)
```

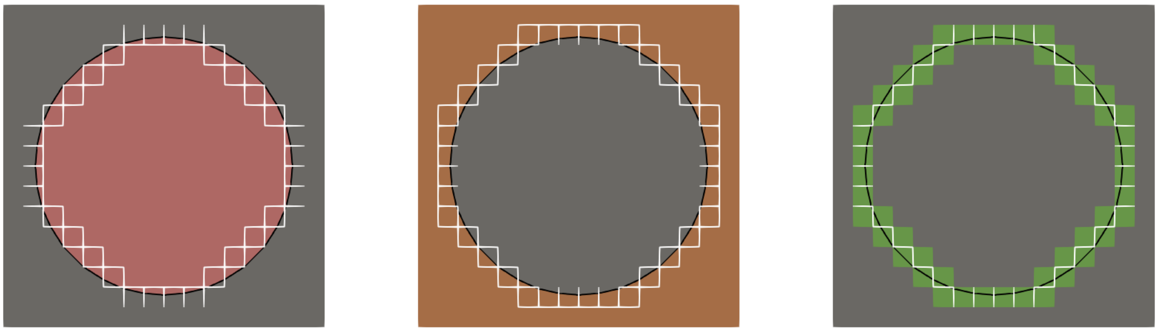

Figure 9: The integration domains and ghost facets for the intracellular domain (left), the extracellular domain (middle), and the domain cut by Γ (right).

Here the ”ReferenceFE” says that we employ a Lagrangian reference element of the given order. For V_e we have defined a Dirichlet boundary on the outer boundary, where the degrees of freedom associated with the boundary are automatically tagged ”boundary” in Gridap. Based on the test spaces, the trial spaces with the corresponding Dirichlet condition for the extracellular domain are defined as follows.

```
Ue = TrialFESpace(Ve,bc)
Ui = TrialFESpace(Vi)
```

The last part consists of combining the two trial and test function spaces.

```
U=MultiFieldFESpace([Ue,Ui])
V=MultiFieldFESpace([Ve,Vi])
```

The next step in implementing the single-dimensional weak formulation (5.23) is now to define the corresponding bilinear form and linear form. The ghost penalty term for the bilinear form is here only implemented for first order elements.

```
a((ue,ui),(ve,vi)) = a_ie((ue,ui),(ve,vi)) + g_h((ue,ui),(ve,vi))
a_ie((ue,ui),(ve,vi)) = (σ_e*∫(∇(ue)⋅∇(ve))dΩe + σ_i*∫(∇(ui)⋅∇(vi))dΩi
                + Cm*Δt ^(-1)*∫((ui-ue)*(vi-ve))dΓ)
g_h((ue,ui),(ve,vi)) = (
    ∫((γ*h^3)*jump(n_Γge⋅∇(ve))*jump(n_Γge⋅∇(ue)))dΓge
    +∫((γ*h^3)*jump(n_Γgi⋅∇(vi))*jump(n_Γgi⋅∇(ui)))dΓgi)
l((ve,vi)) = ∫(g_i*vi)dΩi + ∫(g_e*ve)dΩe + Cm*Δt^(-1)*∫(f*(vi-ve))dΓ
```

Now, we can build the finite element problem, by passing the bilinear form, the linear form, the test, and the trial space to the ”AffineFEOperator” function.

```
op = AffineFEOperator(a,l,U,V)
```

The AffineFEOperator function builds a matrix corresponding to the bilinear form and a vector corresponding to the linear form. Finally, we can solve for a numerical solution, where the default is a LU solver.

```
uhe, uhi = solve(op)
```

An important difference for implementing the multi-dimensional formulation is that we also need to define the space of the cells being cut, $\mathcal{T}_{h,\Gamma}$, and the corresponding faces that are cut.

```
Ωc = Triangulation(cutgeo,CUT,φ)
dΩc = Measure(Ωc,degree)
Γgc = GhostSkeleton(cutgeo,CUT,φ)
dΓgc = Measure(Γgc,degree)
```

$\mathcal{T}_{h,\Gamma}$ is shown in Figure 7 and the corresponding faces are illustrated in Figure 9. The corresponding test and trial space can now be defined based on the cut domain.

```
Vc = TestFESpace(Ωc,ReferenceFE(lagrangian,Float64,0),conformity=:L2)
Uc = TrialFESpace(Vc)
U=MultiFieldFESpace([Ue,Ui,Uc])
V=MultiFieldFESpace([Ve,Vi,Vc])
```

The multi-dimensional (6.10) weak formulation can then be defined.

```
a((ue,ui,im),(ve,vi,jm))=(σ_e*∫(∇(ue)⋅∇(ve))dΩe + ∫((vi-ve)*im)dΓ
    + σ_i*∫(∇(ui)⋅∇(vi))dΩi  + ∫((ui-ue)*jm)dΓ -  ∫((Cm^(-1)*Δt*jm*im))dΓ
    + g_h((ue,ui),(ve,vi))- s_h(im,jm))
g_h((ue,ui),(ve,vi))=(∫((γg*h^3)*jump(n_Γge⋅∇(ve))*jump(n_Γge⋅∇(ue)))dΓge
    +∫((γg*h^3)*jump(n_Γgi⋅∇(vi))*jump(n_Γgi⋅∇(ui)))dΓgi)
s_h(im,jm)=∫((Cm^(-1)*Δt+h)*jump(im)*jump(jm))dΓgc
l((ve,vi,jm)) = ∫(f*jm)dΓ + ∫(g_e*ve)dΩe + ∫(g_i*vi)dΩi
```

7.2 Convergence studies for the spatial formulations

The error estimates in Chapter 5 for the single-dimensional formulations showed that for a constant Δt, the approximation error is expected to converge as h in the energy norm and as h^2 in the L^2-norm. For the multi-dimensional formulation we were only able to derive expected convergence order in the energy norm as $h^{\frac{1}{2}}$ with $\frac{\Delta t}{C_m} \geqslant h$, and as h for $\frac{\Delta t}{C_m} \leqslant h$. In this section, we conduct numerical experiments to study the experimental convergence rates. We perform the test on three different geometries. First, a circular geometry which makes it possible to compare the fitted and unfitted implementations of the single-dimensional formulation. Then, we run an experiment on a more complex geometry, still in two dimensions, before presenting a case formulated in three dimensions.

To perform the convergence analysis we use the method of manufactured solutions. The problem is solved multiple times on decreasing mesh size h_j. For each iteration j, the error E_j between the analytical solution u and the numerical solution u_j is calculated in a chosen norm,

$$E_j = \|u - u_j\|.$$

The experimental rate of convergence (EOC) is given by

$$\text{EOC} = \frac{\log(E_{j-1}/E_j)}{\log(h_{j-1}/h_j)}.$$

We will use first order elements in all the following experiments and set the ghost penalty parameter γ_1 to 0.1.

7.2.1 Creating a manufactured solution

The main idea behind the method of manufactured solution is that we can choose a solution to our problem and then manufacture the problem by computing the corresponding boundary conditions and source terms. To be able to use the method of manufactured solutions, we add source terms to the EMI PDE systems, leading to the following system

$$
\begin{aligned}
-\nabla \cdot \sigma_i \nabla u_i &= g_i && \text{in } \Omega_i, && (7.1a)\\
-\nabla \cdot \sigma_e \nabla u_e &= g_e && \text{in } \Omega_e, && (7.1b)\\
\sigma_e \nabla u_e \cdot \boldsymbol{n_e} &= -\sigma_i \nabla u_i \cdot \boldsymbol{n_i} \equiv I_m && \text{on } \Gamma, && (7.1c)\\
u_i - u_e - \frac{\Delta t}{C_m} I_m &= f && \text{on } \Gamma, && (7.1d)\\
u &= g_{bc} && \text{on } \partial\Omega. && (7.1e)
\end{aligned}
$$

The chosen solution is required to satisfy (7.1c). Assuming we have a sufficiently smooth function $S(x, y)$, our manufactured solutions

$$\begin{aligned} u_i(x, y) &= \frac{1}{\sigma_i} S(x, y), \\ u_e(x, y) &= \frac{1}{\sigma_e} S(x, y), \\ I_m(x, y) &= \nabla S(x, y) \cdot \mathbf{n_e}. \end{aligned}$$

can be created by choosing values for σ_e and σ_i. The corresponding source terms are

$$\begin{aligned} g_i(x, y) &= g_e(x, y) = -\Delta S(x, y), \\ f(x, y) &= \Big(\frac{1}{\sigma_i} - \frac{1}{\sigma_e}\Big) S(x, y) - \frac{\Delta t}{C_m} \nabla S(x, y) \cdot \mathbf{n_e}, \end{aligned}$$

and outer Dirichlet condition $g_{bc} = u_e \mid_{\partial\Omega}$. Note that $\mathbf{n_e} = -\mathbf{n_i}$ is related to the geometry.

7.2.2 Convergence experiment 1

We first conduct convergence studies for the classical single-dimensional, the CutFEM single-dimensional and the CutFEM multi-dimensional formulation. Let the total domain be $\Omega = [-1, 1]^2$, and define the intracellular and extracellular domains as described earlier with the level set function

$$\varphi(x, y) = x^2 + y^2 - 0.7^2.$$

To create the manufactured solution we set

$$S(x, y) = \sin(\pi x) \cos(\pi y),$$

and let $\Delta t = 0.5, C_m = 1, \sigma_i = 1, \sigma_e = 2$.

The fitted mesh is created using GMSH [31], and thereafter the mesh is read into Gridap using GridapGmsh. We gradually decrease the maximal element size $h_{\max}$ 5 times, resulting in the $h_{\max}$ values $[0.1768, 0.0884, 0.0442, 0.0221, 0.0110]$. For the CutFEM formulations we create an uniform mesh, where N^2 is the number of elements. We gradually decrease the element size by setting $N = 2^{2+n}$, with $n = 2, \ldots, 6$.

Solutions to the problem in the first iterations for the single-dimensional formulations are depicted in Figure 10. The resulting errors in the L^2-norm and H^1-seminorm are depicted in Figure 11. For all formulations, we observe that the converge rate is 1 in the H^1-seminorm, and 2 in the L^2-norm. This is as expected for the single-dimensional formulations and better than we theoretically proved for the multi-dimensional formulation. We also observe convergence rate 1 for the current in the L^2-norm on the membrane.

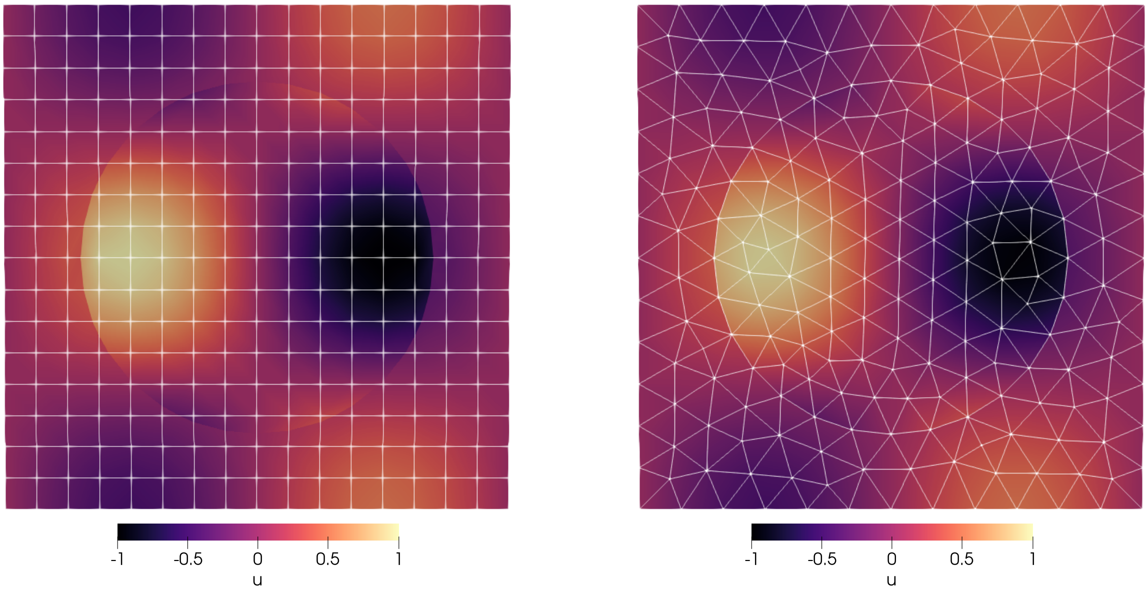

Figure 10: Solution plots for the single-dimensional formulations for the unfitted formulation (left) solved with N=16 and the fitted (right) formulation solved with $h_{\max} = 0.1768$.

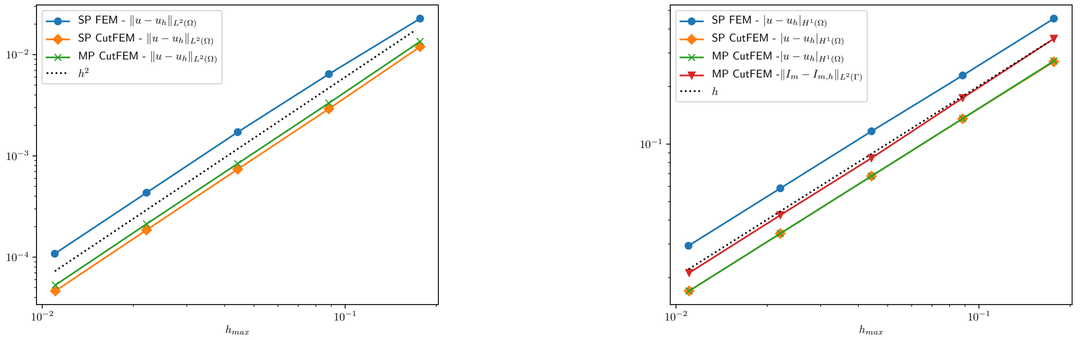

Figure 11: Convergence rates for the fitted single-dimensional and unfitted single and multi-dimensional in L^2-norm (left) and H^1-norm (right) as a function of the maximal element size $h_{\max}$.

A numerical study of Δt

As stated above, our theoretical convergence rate for the single-dimensional formulation is dependent on if $\Delta t \geqslant h$. We now run two numerical convergence tests for both CutFEM formulations where we decrease Δt along with h. The domains, parameters, source terms, and mesh sizes are all as above, except that in the first experiment $\Delta t = 0.001h$ and in the second experiment $\Delta t = 0.001h^2$. The resulting errors and experimental convergence rates can be found in Tables 2 - 5. As expected we see that for the single-dimensional case when Δt is refined together with h we still have optimal convergence in both norms. When Δt is refined faster than h the optimal convergence breaks down. For the multi-dimensional case, the corresponding changes in Δt still give optimal convergence.

7.2.3 Convergence experiment 2

Next, we run a convergence study for both of the CutFEM formulations on a more complex geometry. Let the total domain be defined by $\Omega = [-1.75, 1.75] \times [-2, 1.5]$, and the level set function by

$$\varphi(x, y) = x^2 + y^2 + y \sin((x+1)^2) - 1.5.$$

The manufactured solution is created with

$$S(x, y) = \sin(0.5\pi x)\cos(0.5\pi y),$$

with $\Delta t = 0.2, C_m = 1, \sigma_i = 1.5, \sigma_e = 1$. Both formulations are solved on the same uniform mesh where N^2 is the number of elements. We gradually decrease the element size by setting $N = 2^{2+n}$, with $n = 2, \ldots, 6$. The solutions for both formulations for $N = 128$ is depicted in Figure 12. The resulting errors and convergence rates are given in Table 6 for the single-dimensional formulation, and in Table 7 for the multi-dimensional formulation. We see that the convergence rates are optimal and the same as for the circular geometry. In addition, the values of the errors are very much alike for the single-dimensional and multi-dimensional formulation.

Table 2: Error and convergence rates for the CutFEM single-dimensional formulation with $\Delta t = 0.001h$.

N	$\|u - u_h\|_{\Omega_1 \cup \Omega_2}$	EOC	$\|u - u_h\|_{1,\Omega_1 \cup \Omega_2}$	EOC
16	1.11e-02	–	2.87e-01	–
32	2.82e-03	1.98	1.38e-01	1.06
64	7.02e-04	2.00	6.84e-02	1.01
128	1.76e-04	1.99	3.41e-02	1.00
256	4.42e-05	2.00	1.71e-02	1.00

Table 3: Error and convergence rates for the CutFEM single-dimensional formulation with $\Delta t = 0.001h^2$.

N	$\|u - u_h\|_{\Omega_1 \cup \Omega_2}$	EOC	$\|u - u_h\|_{1,\Omega_1 \cup \Omega_2}$	EOC
16	1.31e-02	-	3.76e-01	-
32	2.83e-03	2.21	1.46e-01	1.37
64	1.04e-03	1.44	8.66e-02	0.75
128	3.30e-04	1.66	5.24e-02	0.72
256	1.00e-04	1.72	2.29e-02	1.19

Table 4: Error and convergence rates for the CutFEM multi-dimensional formulation with $\Delta t = 0.001h$.

N	$\|u - u_h\|_{\Omega_1 \cup \Omega_2}$	EOC	$\|u - u_h\|_{1,\Omega_1 \cup \Omega_2}$	EOC	$\|I_m - I_{m,h}\|_\Gamma$	EOC
16	2.09e-02	-	2.86e-01	-	4.65e-01	-
32	3.59e-03	2.55	1.37e-01	1.07	1.98e-01	1.23
64	7.61e-04	2.24	6.81e-02	1.01	9.01e-02	1.14
128	1.79e-04	2.09	3.41e-02	0.99	4.40e-02	1.03
256	4.42e-05	2.02	1.70e-02	0.99	2.23e-02	0.97

Table 5: Error and convergence rates for the CutFEM multi-dimensional formulation with $\Delta t = 0.001h^2$.

N	$\|u - u_h\|_{\Omega_1 \cup \Omega_2}$	EOC	$\|u - u_h\|_{1,\Omega_1 \cup \Omega_2}$	EOC	$\|I_m - I_{m,h}\|_\Gamma$	EOC
16	2.09e-02	-	2.86e-01	-	4.65e-01	-
32	3.59e-03	2.55	1.37e-01	1.07	1.98e-01	1.23
64	7.61e-04	2.24	6.81e-02	1.01	9.01e-02	1.14
128	1.79e-04	2.09	3.41e-02	0.99	4.40e-02	1.03
256	4.42e-05	2.02	1.70e-02	0.99	2.23e-02	0.97

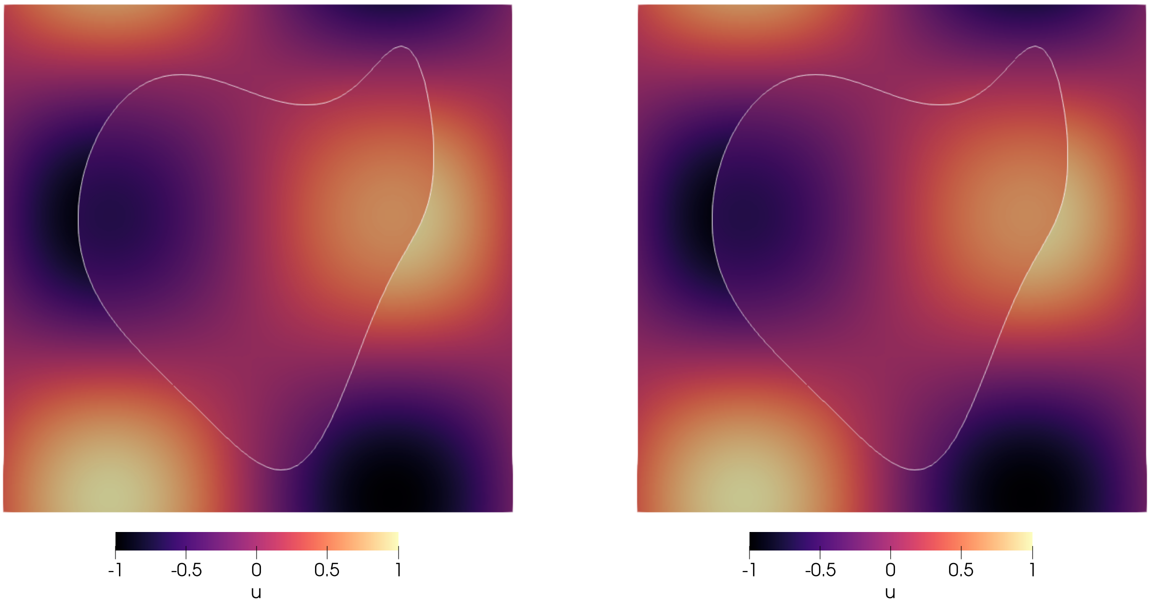

Figure 12: Solution plots for the CutFEM formulations of the single-dimensional (left), and the multi-dimensional (right) both solved on a mesh with 128 × 128 elements.

Table 6: Error and convergence rates for the CutFEM single-dimensional formulation in convergence study 2.

N	$\|u - u_h\|_{\Omega_1 \cup \Omega_2}$	EOC	$\lvert u - u_h \rvert_{1,\Omega_1 \cup \Omega_2}$	EOC
16	2.51e-02	-	4.47e-01	-
32	6.35e-03	1.98	2.25e-01	0.99
64	1.59e-03	2.00	1.13e-01	0.99
128	3.97e-04	2.00	5.65e-02	0.99
256	9.96e-05	2.00	2.83e-02	0.99

Table 7: Error and convergence rates for the CutFEM multi-dimensional formulation in convergence study 2.

N	$\|u - u_h\|_{\Omega_1 \cup \Omega_2}$	EOC	$\lvert u - u_h \rvert_{1,\Omega_1 \cup \Omega_2}$	EOC	$\|I_m - I_{m,h}\|_\Gamma$	EOC
16	2.39e-02	-	4.55e-01	-	3.10e-01	-
32	6.16e-03	1.95	2.27e-01	1.00	1.62e-01	0.94
64	1.59e-03	1.95	1.13e-01	1.00	8.67e-02	0.90
128	4.01e-04	1.99	5.66e-02	1.00	4.01e-02	1.11
256	1.02e-04	1.98	2.83e-02	1.00	2.00e-02	1.00

Table 8: Error and convergence rates for the CutFEM single-dimensional formulation in convergence study 3.

N	$\|u - u_h\|_{\Omega_1 \cup \Omega_2}$	EOC	$\|u - u_h\|_{1,\Omega_1 \cup \Omega_2}$	EOC
12	2.20e-02	-	4.46e-01	-
16	1.22e-02	2.05	3.34e-01	1.00
24	5.46e-03	1.99	2.22e-01	1.00
32	3.06e-03	2.01	1.67e-01	1.00
48	1.36e-03	1.99	1.11e-01	1.00
64	7.67e-04	2.00	8.34e-02	1.00

Table 9: Error and convergence rates for the CutFEM multi-dimensional formulation in convergence study 3.

N	$\|u - u_h\|_{\Omega_1 \cup \Omega_2}$	EOC	$\|u - u_h\|_{1,\Omega_1 \cup \Omega_2}$	EOC	$\|I_m - I_{m,h}\|_\Gamma$	EOC
12	2.95e-02	-	4.49e-01	-	6.57e-01	-
16	1.72e-02	1.87	3.36e-01	1.01	4.89e-01	1.03
24	7.90e-03	1.92	2.23e-01	1.01	3.24e-01	1.01
32	4.48e-03	1.97	1.67e-01	1.00	2.43e-01	1.01
48	2.01e-03	1.97	1.11e-01	1.00	1.61e-01	1.01
64	1.13e-03	2.01	8.34e-02	1.00	1.20e-01	1.03

7.2.4 Convergence experiment 3

In the last convergence study, we extend to three-dimensions. Define $\Omega = [-1, 1]^3$, and let the level set function defining an ellipsoidal be

$$\varphi(x, y, z) = \frac{x^2}{0.8^2} + y^2 + \frac{z^2}{0.9^2} - 0.8^2$$

To create a manufactured solution, set

$$S(x, y, z) = \sin(\pi x)\cos(\pi y)\exp(0.5z)$$

and let $\Delta t = 0.5, C_m = 1, \sigma_i = 1, \sigma_e = 3$. The uniform mesh has N^3 cubical elements. We gradually decrease the element size by setting $N = [12, 16, 24, 32, 48, 64]$. The resulting errors and experimental convergence rates are listed in Table 8 for the single-dimensional formulation, and Table 9 for the multi-dimensional formulation. The experiment shows that the convergence rates are the same as for the two-dimensional geometries. In addition we notice that for all three cases, the errors are practically identical for both CutFEM formulations.

7.3 Condition number studies

7.3.1 Scaling

In Section 5.4, we showed that a theoretical bound for the condition number of the stiffness matrix related to the CutFEM single-dimensional formulation was

$$\kappa(A) \lesssim \mathcal{O}(h^{-2}) + \mathcal{O}(h^{-1}(\Delta t)^{-1}),$$

where the hidden constant depends on C_m, σ_e and σ_i. The next numerical experiment is performed to investigate the scaling of the condition number. This is done by refining the mesh and computing the condition numbers of the associated stiffness matrix. This experiment is performed for the CutFEM single-dimensional and multi-dimensional formulations. Let the domains and parameters be as in convergence test 1 for the two-dimensional circular domain, except that $\Delta t = 0.1$. We refining the mesh with mesh sizes corresponding to $N = [12, 16, 24, 32, 48]$. The resulting scaled convergence numbers are listed in Table 10 and show that the convergence numbers indeed scale like h^2.

Next, we perform a study to check the bound concerning Δt for the CutFEM single-dimensional formulation. We run two experiments with all parameters and mesh sizes as before, except that in the first experiment $\Delta t = 0.1/N$ and in the second $\Delta t = 0.1/N^2$. Table 11 lists the resulting scaled condition numbers of the stiffness matrix. As expected we see that for the first experiment the condition numbers scale as h^{-2}, and for the second the condition numbers scale as h^{-3}.

7.3.2 Sensitivity analysis

The theoretical bound of the condition number is geometrically robust, i.e. independent of how the background mesh is cut by the domains. We perform a sensitivity analysis to check how cut configurations affect the condition number. This is done by repeatedly moving Ω_i while assembling the stiffness matrix and computing the associated condition number, such that the stiffness matrix is computed on different cut configurations. Let Γ_δ be a circle with radius 0.5, and the center of the circle for step m be defined by

$$S = \delta \left(\frac{1}{N}, \frac{1}{N} \right), \quad \delta = \frac{m}{M}, \tag{7.2}$$

where M is the number of steps, and N is the mesh size. Figure 13 shows how the circle is moved from the first iteration to the last iteration.

Set $N = 32, M = 500, \Delta t = 0.5, \sigma_e = 2, \sigma_1 = 1, C_m = 1$. For both the CutFEM single-dimensional and multi-dimensional we run the experiment twice, with and without the stabilization terms. The resulting condition numbers are depicted in Figure 14. The non-stabilized formulations are very sensitive to the particular cut configurations, in contrast to the stabilized formulations where the condition numbers are practically constant. Notice also that the condition numbers of the two formulations are very much alike.

Table 10: Scaled condition numbers for the single-dimensional (left) and the multidimensional formulation (right) with Δt constant

N	$\kappa(A)N^{-2}$
12	9,98
16	9,76
24	9,50
32	10,64
48	10,38

N	$\kappa(A)N^{-2}$
12	10.04
16	9,75
24	9,51
32	10,65
48	10,38

Table 11: Scaled condition numbers for the single-dimensional formulation with $\Delta t = 0.1/N$ (left) and $\Delta t = 0.1/N^2$ (right)

N	$\kappa(A)N^{-2}$
12	44,65
16	37,67
24	36,05
32	44,32
48	38,81

N	$\kappa(A)N^{-3}$
12	41,32
16	35,68
24	30,56
32	41,81
48	33,95

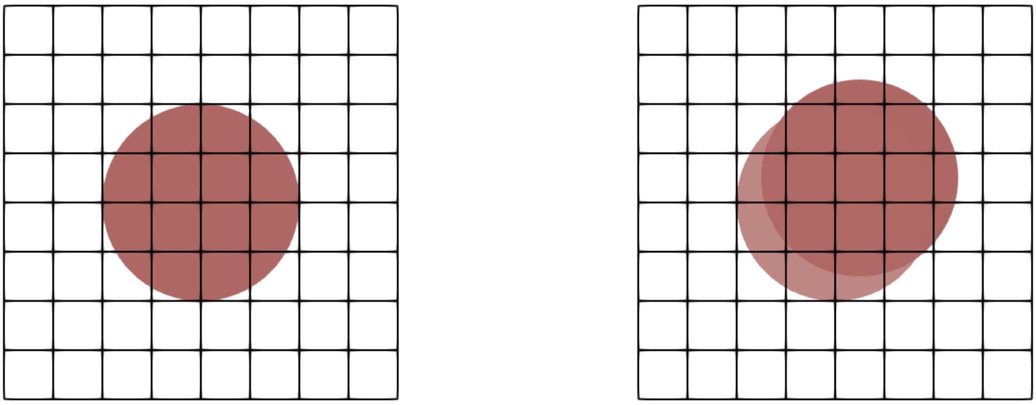

Figure 13: Illustration of how the sensitivity analysis is performed, with the position of the intracellular domain for the first (left) and last (right) iteration.

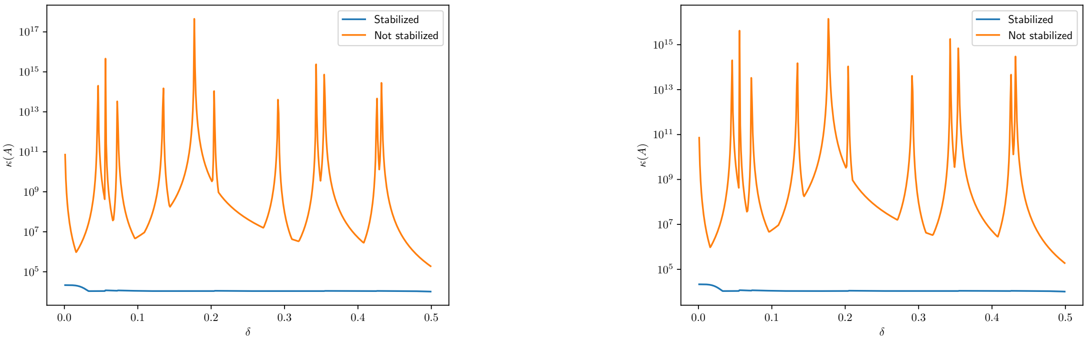

Figure 14: The condition numbers of the stiffness matrix plotted against the translation parameter δ with and without stabilization for the single-dimensional (left) and multi-dimensional formulation (right).

7.4 Solving the EMI PDEs on complex geometries

One main motivation behind this thesis was to solve the EMI model using an unfitted finite element formulation, which allows us to utilize complex geometries. To demonstrate the applicability of the proposed framework to more complex geometries we now replace the analytically defined level set function with a surface mesh of the membrane. Thanks to the Gridap Extension package STLCutters, STL surface mesh can be used to represent the interface Γ, for more details see [7].

After the intracellular domain is given as the inside of the membrane, the total domain is defined as a cuboid surrounding the intracellular domain. Let

$$f(x, y, z) = \sin(0.05x + 0.06y + 0.04z),$$

and $\sigma_e = 2, \sigma_i = 1, \Delta t = 1, C_m = 1$. We are now solving with the CutFEM single-dimensional formulation.

We start with a model where the intracellular domain is represented as a deer head found at [56]. The mesh is created by 30^3 elements. Figure 15 gives an illustration of the deer head together with the meshes used. The solution on the membrane is depicted in Figure 16.

The final experiment is to test the framework on an idealized reconstruction of a neuron. The reconstruction is found under ID: ”NMO_76781” [41] at NeuroMorpho.org [5] and is postproced using [48] by Miroslav Kutcha into a STL format. This experiment is purely meant as a demonstration of how the framework can be used to solve the model on complex cellular geometries. The total mesh consists of $180 \times 180 \times 20$ elements, and the solution of the intracellular potential on the surface of the domain is depicted in Figure 17. The thin structure of parts of the neural cells is illustrated in the figure, and we would assume that the spatial resolution is too coarse to get a good approximation in these regions.

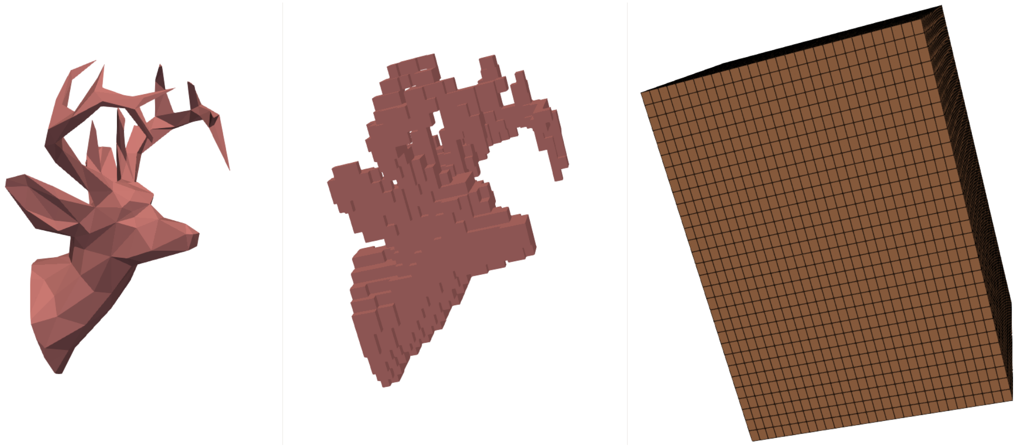

Figure 15: Illustration of the STL-mesh of the deer head together with an illustration of the intracellular mesh and the total domain.

Figure 16: Numerical solution of the intracellular potential on the membrane surface for the EMI PDES solved with a deer head as the intracellular domain.

Figure 17: Numerical solution of the intracellular potential on the membrane surface for the EMI PDES solved with a representation of an idealized neuron.

7.5 Numerical experiments with ODEs on an unfitted surface*

Next, we conduct two numerical experiments to test the convergence rates for the discretization of ODEs on the surface. In both cases let the structured background mesh over the domain $\Omega = [-1, 1]^2$ consist of square elements, where N^2 is the total number of elements set to $N = 64$. The surface embedded into the background mesh is defined by $\Gamma = \{(x, y) : x^2 + y^2 = 0.6^2\}$. The stabilization parameter is set to $\gamma_b = 0.1$. We have only found theoretical results to support the face based stabilization (4.9) for triangular elements but is still employed here since we have not observed any numerical problems. The time intervals are uniformly distrubted, where the number of time intervals is set to $M = 2^{n+1}$ with $n = 1, \dots, 6$. In the first ODE test case we use the test system,

$$\begin{aligned} v_t(x, y, t) &= -s(x, y, t) \\ s_t(x, y, t) &= v(x, y, t), \end{aligned}$$

with exact solutions,

$$\begin{aligned} v(x, y, t) &= (x + y) \sin(t), \\ s(x, y, t) &= -(x + y) \cos(t). \end{aligned}$$

We solve the system on the time interval $[0, 2]$.

In the second experiment, we use the method of manufactured solutions on the reparameterized FitzHugh-Nagumo model (2.11), with parameters $v_{rest} = -85\,\text{mV}$, $v_{peak} = 40\,\text{mV}$ and the rest as listed in Table 1, all found in [55]. We assume the following exact solutions for the FitzHugh-Nagumo model,

$$\begin{aligned} v(x, t) &= e^{Dt}, \\ s(x, t) &= e^{-b_1 c_3 t}, \end{aligned}$$

where $D = \frac{c_1}{v_{\text{amp}}^2}(v_{\text{th}} v_{\text{peak}} + v_{\text{rest}} v_{\text{peak}} + v_{\text{th}} v_{\text{rest}})$, leading to the equations

$$\begin{aligned} v_t = {} & \frac{c_1}{v_{\text{amp}}^2}(v - v_{\text{rest}})(v - v_{th})(v_{\text{peak}} - v) - \frac{c_2}{v_{\text{amp}}}(v - v_{\text{rest}})s \\ & - \frac{c_1}{v_{\text{amp}}^2}(-e^{3Dt} + (v_{\text{peak}} + v_{\text{rest}} + v_{\text{th}})e^{2Dt} + v_{\text{rest}} + v_{\text{peak}} + v_{\text{amp}}) \qquad (7.3a) \\ & + \frac{c_2}{v_{\text{amp}}}(e^{Dt} - v_{\text{rest}})e^{-b_1 c_3 t}, \\ s_t = {} & b(v - v_{rest} - c_3 s). \qquad (7.3b) \end{aligned}$$

which we will refer to as the test FitzHugh-Nagumo system. We solve this system on the time interval $[0, 50]$. We define the discrete $L^\infty L^2$- and $L^\infty H^1$-norms by

$$\begin{aligned} \|u\|_{L^\infty L^2(\Omega)} &= \max_{m \in [0, \dots, M]} \|u(\cdot, t_m)\|_\Omega \\ \|u\|_{L^\infty H^1(\Omega)} &= \max_{m \in [0, \dots, M]} \|u(\cdot, t_m)\|_{1,\Omega}. \end{aligned}$$

Table 13: Error and convergence rates for the first ODE test case in $L^\infty L^2$-norm when refining temporal resolution.

M	$\|v - v_h\|_{L^\infty L^2(\Gamma)}$	EOC	$\|s - s_h\|_{L^\infty L^2(\Gamma)}$	EOC
4	$6.88 \cdot 10^{-1}$	–	$2.44 \cdot 10^{-1}$	–
8	$3.14 \cdot 10^{-1}$	1.13	$1.03 \cdot 10^{-1}$	1.24
16	$1.45 \cdot 10^{-1}$	1.11	$5.16 \cdot 10^{-2}$	1.00
32	$6.95 \cdot 10^{-2}$	1.07	$2.83 \cdot 10^{-2}$	0.86
64	$3.39 \cdot 10^{-2}$	1.03	$1.15 \cdot 10^{-2}$	0.95
128	$1.67 \cdot 10^{-2}$	1.02	$7.45 \cdot 10^{-3}$	0.98

Table 14: Error and convergence rates for the test FitzHugh-Nagumo system in $L^\infty L^2$-norm when refining temporal resolution.

M	$\|v - v_h\|_{L^\infty L^2(\Gamma)}$	EOC	$\|s - s_h\|_{L^\infty L^2(\Gamma)}$	EOC
4	$4.95 \cdot 10^{-1}$	–	$2.97 \cdot 10^{-1}$	–
8	$2.18 \cdot 10^{-1}$	1.19	$1.42 \cdot 10^{-1}$	1.06
16	$1.02 \cdot 10^{-1}$	1.10	$6.89 \cdot 10^{-2}$	1.04
32	$4.93 \cdot 10^{-2}$	1.05	$3.39 \cdot 10^{-2}$	1.02
64	$2.43 \cdot 10^{-2}$	1.02	$1.68 \cdot 10^{-2}$	1.01
128	$1.20 \cdot 10^{-2}$	1.01	$8.37 \cdot 10^{-3}$	1.01

The resulting errors in $L^\infty L^2$-norm for each of the two experiments are listed in Table 13 and Table 14. It shows that the experimental convergence rates are around 1, which is expected since explicit Euler was used as time discretization.

7.6 Numerical experiments with the passive membrane model*

Consider the EMI model together with the passive membrane model (2.2). As this model is linear, the ODE-step of the operator splitting can be omitted, and we only need to solve the PDE-step. In both the convergence study and the simulation, let the structured background mesh over the total domain $\Omega = [-1, 1]^2$ consist of square elements such that the number of elements along one side of the domain is N with element size $h = 2\sqrt{2}/N$. The stability parameter for the PDE , defined in (5.22), is set to $\gamma_1 = 0.1$, and we use the CutFEM single-dimensional formulation.

7.6.1 Convergence study using a manufactured solution

For the convergence study we set $R_m = 1$ and $v_{rest} = 0$, such that $I_{\text{ion}} = v$. Let $\Omega_i = \{(x, y) : x^2 + y^2 < 0.5^2\}$, $\Omega_e = \Omega \setminus \Omega_i$, and set $\sigma_e = \sigma_i = C_m = 1$. Using the method of manufactured solutions, we define the analytical solutions by

$$\begin{aligned} u_e(x, y, t) &= \cos(\pi(x^2 + y^2 - 0.5^2)), \\ u_i(x, y, t) &= (1 + e^{-t}) \cos(\pi(x^2 + y^2 - 0.5^2)), \\ v(x, y, t) &= e^{-t} \cos(\pi(x^2 + y^2 - 0.5^2)). \end{aligned}$$

We refine both the spatial and temporal resolution. Let $N = 2^{n+3}$ and $M = 2^{n+2}$,where M is the number of uniformly distributed time intervals, with $n = 1, \ldots, 5$. The experiment is run on the time interval $[0, 1]$. While the theoretical analysis of the fully discretized scheme is subject to future research, we intuitively expect that

$$\|u - u_h\|_{L^\infty L^2(\Omega)} \lesssim h^2 + \tau,$$

since first-order elements typically gives second-order convergence for Poisson type problems in space in the L^2-norm and since the explicit Euler method is first-order accurate in time. Similarly we expect that

$$\|u - u_h\|_{L^\infty H^i(\Omega)} \lesssim h + \tau,$$

as first-order elements typically gives first-order convergence for these problems in the H^1-norm.

The resulting errors and convergence rates are listed in Table 15. Here we see that the experimental convergence rate in the $L^\infty H^1$-norm is 1, which is as expected. We would also expect the rate in the $L^\infty L^2$-norm to be first-order since the time discretization used is only first order. However, numerically we get second-order convergence. This indicates that the spatial error contribution dominates the total error for the discrete solution. We perform an additional convergence study with only temporal refinements to explore this further. Let the spatial resolution be high with $N = 256$, and let $M = 2^{n+1}$ with $n = 1, \ldots, 6$. The results is shown in Table 16. Here we see that in the L^2-norm the rate is around 1. However, in the H^1-norm the error is practically constant. We assume this to be because the error in H^1-norm is still dominated by the error in space, even with a fine mesh.

Table 15: Error and convergence rates for the passive test case in $L^\infty L^2$-and $L^\infty H^1$-norm when refining both temporal and spatial resolution.

N/M	$\|u-u_h\|_{L^\infty L^2(\Omega)}$	EOC	$\|u-u_h\|_{L^\infty H^1(\Omega)}$	EOC
16/8	$7.66 \cdot 10^{-2}$	–	$1.29 \cdot 10^{0}$	–
32/16	$1.78 \cdot 10^{-2}$	2.10	$6.63 \cdot 10^{-1}$	0.96
64/32	$4.09 \cdot 10^{-3}$	2.13	$3.35 \cdot 10^{-1}$	0.97
128/64	$1.05 \cdot 10^{-3}$	2.06	$1.67 \cdot 10^{-1}$	0.99
256/128	$4.22 \cdot 10^{-4}$	2.04	$8.43 \cdot 10^{-2}$	1.00

Table 16: Error and convergence rates for the passive test case in $L^\infty L^2$-and $L^\infty H^1$-norm when refining only temporal resolution with constant high spatial resolution.

M	$\|u-u_h\|_{L^\infty L^2(\Omega)}$	EOC	$\|u-u_h\|_{L^\infty H^1(\Omega)}$	EOC
4	$1.86 \cdot 10^{-2}$	–	$8.36 \cdot 10^{-2}$	–
8	$9.50 \cdot 10^{-3}$	0.97	$8.40 \cdot 10^{-2}$	-0.01
16	$4.70 \cdot 10^{-3}$	1.01	$8.42 \cdot 10^{-2}$	0.00
32	$2.25 \cdot 10^{-3}$	1.06	$8.43 \cdot 10^{-2}$	0.00
64	$1.02 \cdot 10^{-3}$	1.14	$8.43 \cdot 10^{-2}$	0.00
128	$4.22 \cdot 10^{-4}$	1.27	$8.43 \cdot 10^{-2}$	0.00

7.6.2 Simulation with the passive membrane model

Next, we run a simulation solving the EMI model with the passive membrane model, as given in (2.2). Let $\Omega_i = \{(x, y) : x^2 + y^2 < 0.6^2\}$, $\Omega_e = \Omega \setminus \Omega_i$, $\sigma_e = 20\,\mathrm{mS/cm}$, $\sigma_i = 5\,\mathrm{mS/cm}$,$R_m = 1\,\mathrm{k\Omega cm^2}$ and $C_m = 1\,\mathrm{mF/cm^2}$. We run the simulation to $T = 6$ with time resolution $M = 300$ and spatial resolution $N = 64$. The mean value of the membrane potential is defined as

$$v_{\text{mean}} = \frac{\int_\Gamma v\; ds}{\int_\Gamma\; ds}.$$

Let the resting potential be $v_{rest} = -85\,\mathrm{mV}$. As initial value we set $v(x, y, 0) = 30\,\mathrm{mV}$, which corresponds to a depolarized cell [55].

The resulting v_{mean} from the simulation is depicted in Figure 18. Also u_e and u_i for several timesteps is depicted in Figure 19. Here we see that the cell repolarizes until the potential in the intracellular space reaches the resting potential.

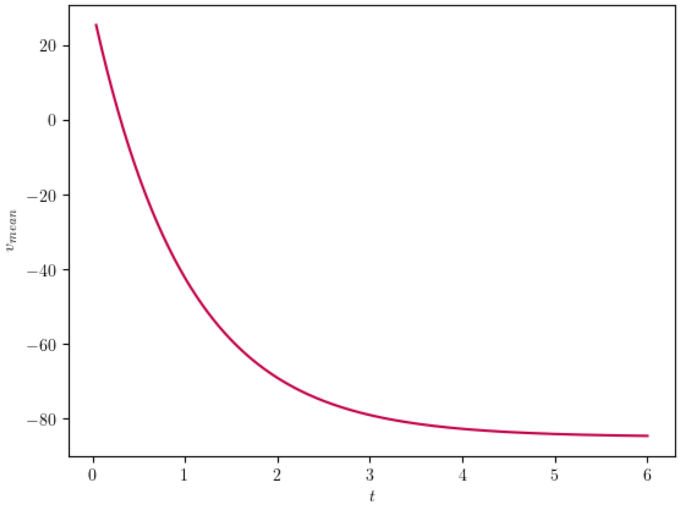

Figure 18: Numerical solution for the average of the membrane potential for a depolarized cell being repolarized from a passive membrane model.

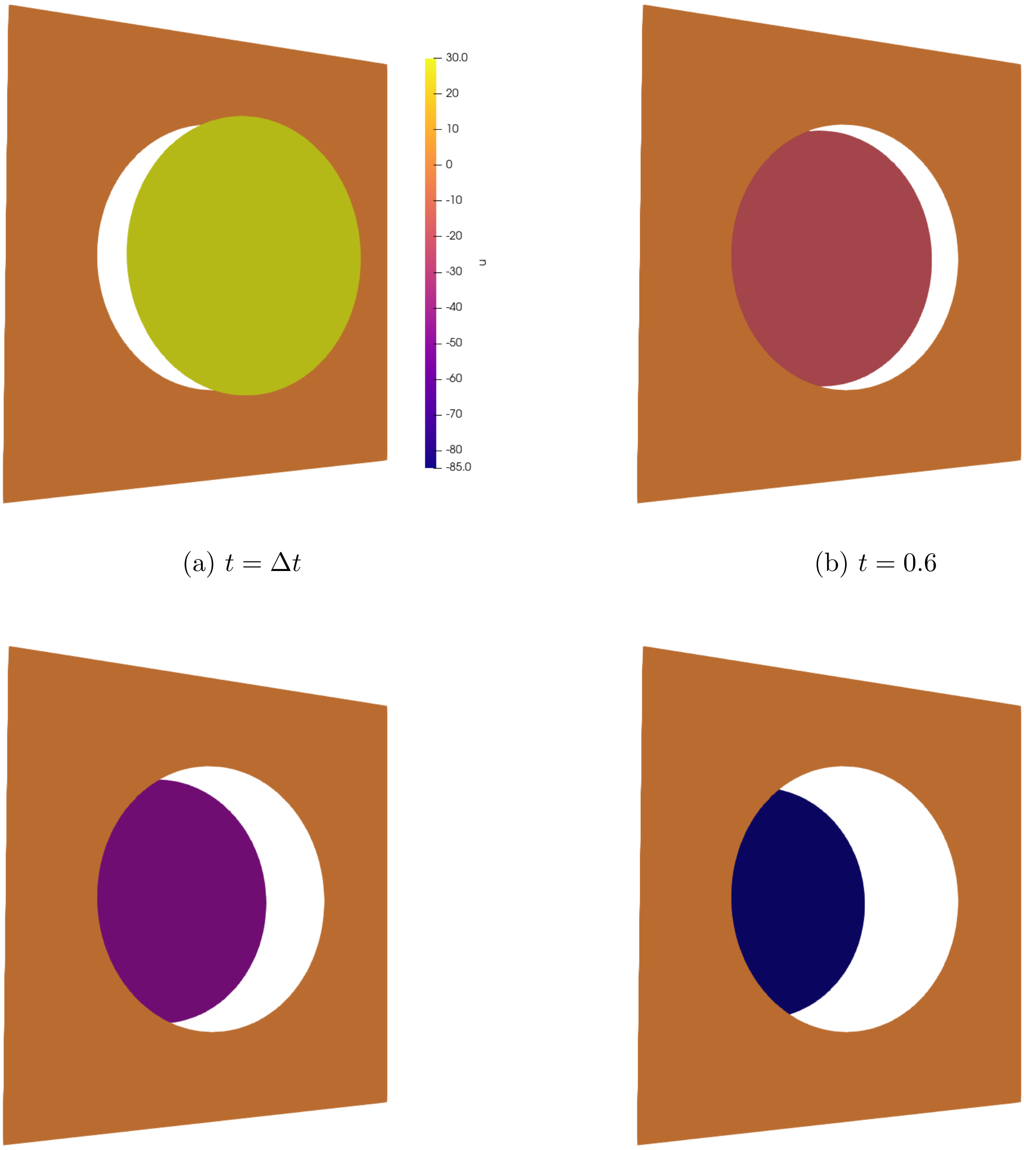

(a) $t = \Delta t$

(b) $t = 0.6$

(c) $t = 1.2$

(d) $t = 6$

Figure 19: Snapshots of the numerical solution in the extra/intracellular domain for a depolarized cell being repolarized from a passive membrane model.

7.7 Numerical experiments with the active membrane model*

In the next numerical experiments, we consider an active membrane model, so that we need to solve both the ODE and the PDE step of the operator splitting scheme introduced in Section 4.2. Here we conduct two convergence studies and conclude with a simulation. For all the experiments the total domain is $\Omega = [-1, 1]$, the structured background mesh over Ω consist of square elements such that the number of elements along one side of the domain is N with element size $h = 2\sqrt{2}/N$. The intracellular domain is defined as $\Omega_i = \{(x, y) : x^2 + y^2 < 0.6^2\}$, and the extracellular domain as $\Omega_e = \Omega \setminus \Omega_i$. Both the PDE stability parameter (5.22) and the ODE stability parameter (4.9) is set to $\gamma_1 = \gamma_b = 0.1$. The CutFEM single-dimensional formulation is employed for the PDE step.

7.7.1 Convergence study with manufactured solutions

In this section we consider two different ODE systems for the EMI model. Let $\sigma_e = \sigma_i = C_m = 1$. Let the first ODE system be

$$
\begin{aligned}
v_t &= -s, \\
s_t &= v.
\end{aligned}
$$

Using the method of manufactured solutions, define the analytical solutions by

$$
\begin{aligned}
u_e(x, y, t) &= \cos(\pi(x^2 + y^2 - 0.6^2)), \\
u_i(x, y, t) &= (1 + \sin(t)) \cos(\pi(x^2 + y^2 - 0.6^2)), \\
v(x, y, t) &= \sin(t) \cos(\pi(x^2 + y^2 - 0.6^2)), \\
s(x, y, t) &= -\cos(t) \cos(\pi(x^2 + y^2 - 0.6^2)).
\end{aligned}
$$

We will refer to this system as splitting test case, and solve it on the time interval $[0, 1]$.

In the second case, let the ODE system be as in (7.3), i.e the modified Fitz-Hugh Nagumo system. Using the method of manufactured solutions let the analytical solutions be

$$
\begin{aligned}
u_e(x, y, t) &= \cos(\pi(x^2 + y^2 - 0.6^2)), \\
u_i(x, y, t) &= (1 + \sin(t)) \cos(\pi(x^2 + y^2 - 0.6^2)), \\
v(x, y, t) &= e^{Dt} \cos(\pi(x^2 + y^2 - 0.6^2)), \\
s(x, y, t) &= e^{-b_1 c_3 t} \cos(\pi(x^2 + y^2 - 0.6^2)).
\end{aligned}
$$

We will refer to this system as the Fitz-Hugh Nagumo test case, and solve it on the time interval $[0, 50]$. For both cases, the temporal and spatial resolution is refined simultaneously, where the number of uniformly distributed time steps is set to $M = [12, 18, 24, 36, 48, 64]$

and the spatial resolution to $N = 8M$. The convergence rates are expected to be first-order in both $L^\infty L^2$- and $L^\infty H^1$-norm, with the same arguments as in Section 7.6.1.

The results are listed in Table 17 and 18. We see that for the splitting test case the experimental $L^\infty L^2$- and $L^\infty H^1$-norm are 1. For the Fitz-Hugh Nagumo test case the $L^\infty H^1$-norm is 1, as expected. The $L^\infty L^2$-norm varies, but all values are over 1. A possible reason could be the same as in the passive case, that the contribution from the spatial error is larger and dominates.

Table 17: Error and convergence rates for the splitting test case in $L^\infty L^2$-and $L^\infty H^1$-norm when refining both temporal and spatial resolution.

N/M	$\|u-u_h\|_{L^\infty L^2(\Omega)}$	EOC	$\|u-u_h\|_{L^\infty H^1(\Omega)}$	EOC
96/12	$3.32 \cdot 10^{-2}$	–	$2.22 \cdot 10^{-1}$	–
144/18	$2.32 \cdot 10^{-2}$	0.89	$1.48 \cdot 10^{-1}$	0.99
192/24	$1.77 \cdot 10^{-2}$	0.94	$1.11 \cdot 10^{-1}$	1.00
288/36	$1.20 \cdot 10^{-2}$	0.95	$7.42 \cdot 10^{-2}$	1.00
384/48	$9.09 \cdot 10^{-3}$	0.97	$5.57 \cdot 10^{-2}$	1.00
512/64	$6.86 \cdot 10^{-3}$	0.98	$4.18 \cdot 10^{-2}$	1.00

Table 18: Error and convergence rates for the FitzHugh-Nagumo test case in $L^\infty L^2$-and $L^\infty H^1$-norm when refining both temporal and spatial resolution.

N/M	$\|u-u_h\|_{L^\infty L^2(\Omega)}$	EOC	$\|u-u_h\|_{L^\infty H^1(\Omega)}$	EOC
96/12	$2.99 \cdot 10^{-1}$	–	$2.24 \cdot 10^{-1}$	–
144/18	$1.59 \cdot 10^{-1}$	1.56	$1.50 \cdot 10^{-1}$	0.99
192/24	$1.04 \cdot 10^{-1}$	1.48	$1.12 \cdot 10^{-1}$	1.00
288/36	$5.34 \cdot 10^{-2}$	1.64	$7.50 \cdot 10^{-2}$	1.00
384/48	$3.11 \cdot 10^{-2}$	1.88	$5.62 \cdot 10^{-2}$	1.00
512/64	$1.57 \cdot 10^{-2}$	2.36	$4.22 \cdot 10^{-2}$	1.00

7.7.2 Simulation with FitzHugh-Nagumo

In the last numerical experiment an active membrane model is considered. Let the membrane model be the reparametrized FitzHugh-Nagumo model as written in (2.11) for I_{ion} and let the rest of the EMI model be as in (2.10). The parameters are set as $\sigma_e = 20\,\mathrm{mS/cm}$, $\sigma_i = 5\,\mathrm{mS/cm}$, $C_m = 1\,\mathrm{mF/cm}^2$ $v_{rest} = -85\,\mathrm{mV}$, $v_{peak} = 40\,\mathrm{mV}$, and the rest of the parameters as listed in Table 1. We set $N = 64$, $M = 800$ and run to $T = 400$. We apply a stimulus current from time $t = 50$ to $t = 60$ with intensity $I_{app} = 0.05v_{amp}$, set the initial conditions to be $v(x, y, 0) = -85\,\mathrm{mV}$, and $s(x, y, 0) = 0\,\mathrm{mV}$.

The results from the simulation are depicted with the average for the membrane potential in Figure 20 and snapshots in Figure 21. Here we see that until $t = 50$, the membrane potential is constant. Then the cell depolarizes from the applied stimulus before it gradually repolarizes until it reaches the resting potential.

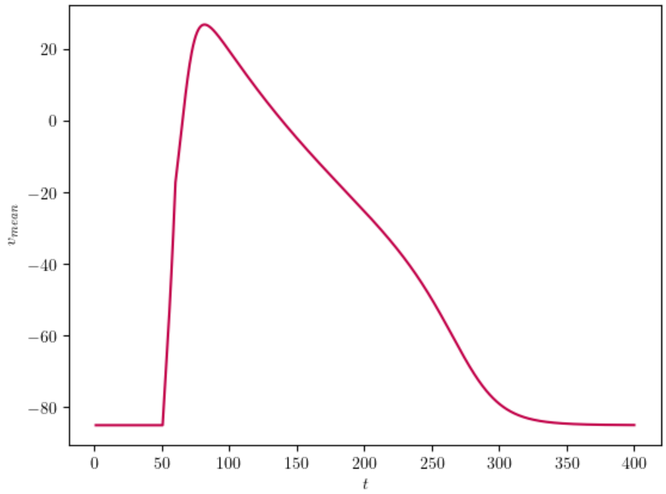

Figure 20: Numerical solution for the average of the membrane potential for a polarized cell being depolarized and repolarized with the FitzHugh-Nagumo membrane model.

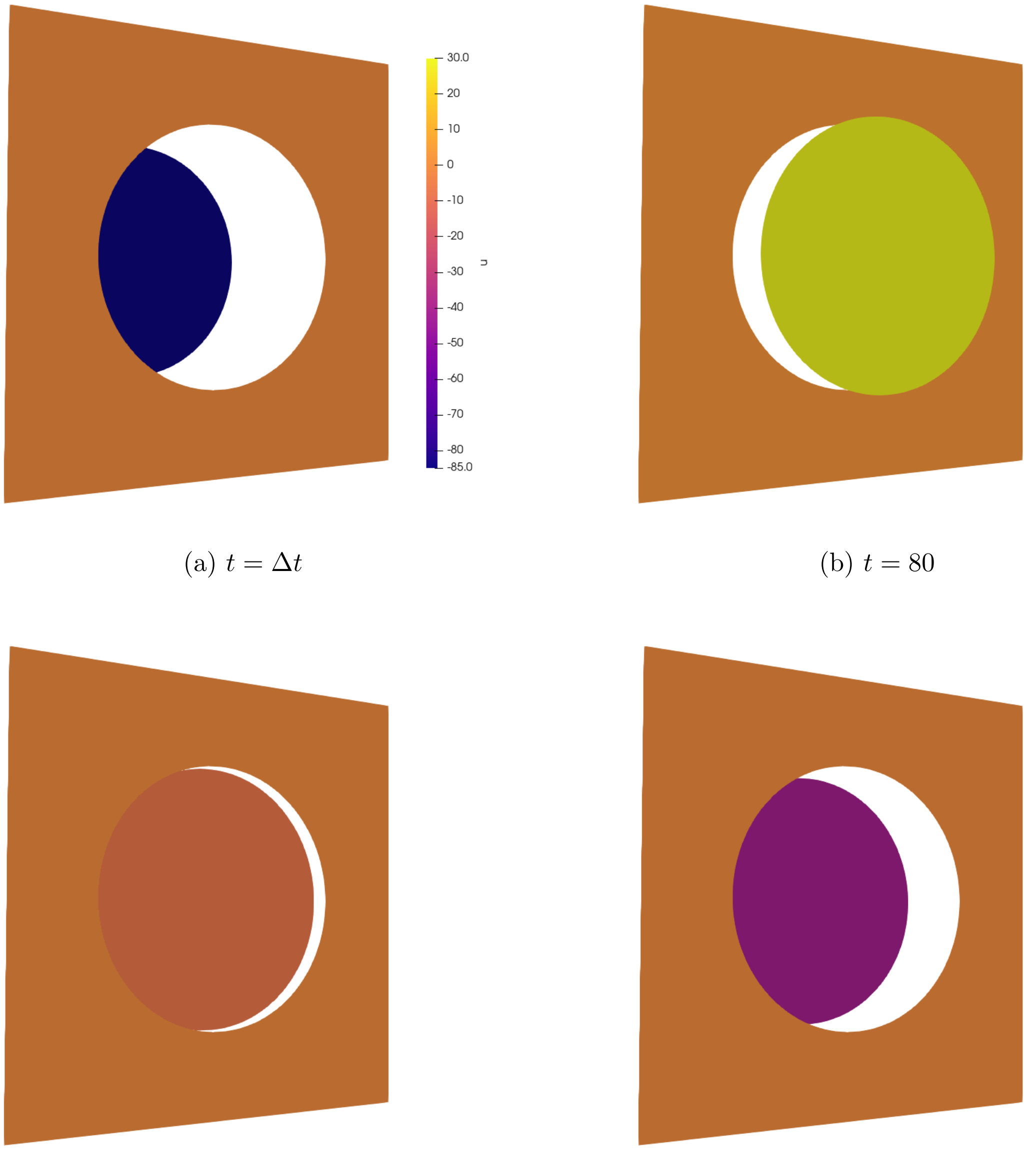

(a) $t = \Delta t$

(b) $t = 80$

(c) $t = 160$

(d) $t = 240$

Figure 21: Snapshots of the numerical solution in the extra/intracellular domain of a polarized cell being depolarized and repolarized with the FitzHugh-Nagumo membrane model.

Chapter 8

Conclusions and outlook

In this thesis, we have developed a novel computational framework for solving the complete EMI model using unfitted finite element technologies, which allows for a simplified and more flexible handling of complex cell geometries. By circumventing the time-consuming and CPU-intense generation of high-quality 3D volume meshes the framework gives new possibilities to short-cut and accelerate current simulation pipelines for simulating electrical activity in neural cells.

Based on a Godunov splitting scheme, the model's PDE-ODE system was decoupled into a PDE step and an ODE step. We have proposed two different CutFEM formulations for the PDE step, and provided a detailed theoretical and numerical analysis showing favorable stability and optimal convergence properties. An important characteristic trait of the presented methods is their geometrical robustness assuring that all derived properties do not depend on how the embedded cell geometry cuts the background mesh. Moreover, we also introduced a new approach to discretize the membrane bound ODEs in an unfitted setting by employing a stabilized L^2 surface projection. Finally, we did extensive numerical testing for both the individual steps and the complete solution scheme, including a series of convergence and robustness tests and as well as showcasing applications to complex cell geometries.

The main difference we found between the two proposed CutFEM formulations is their robustness with respect to the relationship between the spatial and temporal resolution, where the multi-dimensional formulation was preferable for small timesteps, while the single-dimensional formulation performed best for the case of smaller spatial than temporal resolution. The multi-dimensional formulation is also more flexible, but its saddle point structure requires the computation of a larger linear system and makes the design of efficient preconditioners more challenging. Therefore, the choice of formulation would depend on the desired resolution and computational resources. Also, [60] formulated a $H(\text{div})$-based formulation of the EMI PDEs. Based on the recent idea of CutFEM for $H(\text{div})$ formulations [29], we suggest looking further into a $H(\text{div})$ CutFEM formulation for the EMI PDEs.

The theoretical analysis in this thesis focused on the spatial discretization of the PDE step arising from the employed Godunov splitting scheme. Thus, a natural next step would be to conduct a theoretical analysis of the time-discretization methods as well as the whole splitting scheme. We also suggest extending the first-order Godunov scheme to a second-order Strang splitting, which would require extending the time discretization of the ODE and PDE step to second-order methods. Furthermore, while the membrane bound ODEs are pointwise defined in the EMI model, our proposed unfitted discretization method results in an artificially spatial coupling caused by the application of a weak formulation of the ODE system. For a possible remedy, we suggest exploring lumping techniques.

As stated in the introduction, the EMI model is computationally very demanding. To employ the proposed CutFEM framework to larger scale problems involving realistic cell and network geometries, we plan to improve the method's performance and scalability properties by means of parallelization and preconditioning. Moreover, to obtain a holistic simulation pipeline, we need to investigate user-friendly approaches to feed imaging data of cells directly into our current simulation toolkit. Finally, we suggest adaptive mesh refinement for better simulations concerning the thin structure of the neural cells.

Bibliography

[1] A. Agudelo-Toro. *Numerical Simulations on the Biophysical Foundations of the Neuronal Extracellular Space*. PhD thesis, Georg-August-University Göttingen, 2013.

[2] A. Agudelo-Toro and A. Neef. Computationally efficient simulation of electrical activity at cell membranes interacting with self-generated and externally imposed electric fields. *Journal of Neural Engineering*, 10(2):026019, Apr. 2013.

[3] J. Ahrens, B. Geveci, and C. Law. ParaView: An End-User Tool for Large-Data Visualization. In *Visualization Handbook*, pages 717–731. Elsevier, 2005.

[4] M. Amar, D. Andreucci, P. Bisegna, and R. Gianni. Existence and uniqueness for an elliptic problem with evolution arising in electrodynamics. *Nonlinear Analysis: Real World Applications*, 6(2):367–380, Apr. 2005.

[5] G. A. Ascoli, D. E. Donohue, and M. Halavi. NeuroMorpho.Org: A Central Resource for Neuronal Morphologies. *Journal of Neuroscience*, 27(35):9247–9251, Aug. 2007.

[6] I. Babuška. The finite element method with Lagrangian multipliers. *Numerische Mathematik*, 20:179–192, June 1973.

[7] S. Badia, P. A. Martorell, and F. Verdugo. Geometrical discretisations for unfitted finite elements on explicit boundary representations. *Journal of Computational Physics*, 460:111162, July 2022.

[8] S. Badia and F. Verdugo. Gridap: An extensible Finite Element toolbox in Julia. *Journal of Open Source Software*, 5(52):2520, Aug. 2020.

[9] R. Becker, P. Hansbo, and R. Stenberg. A finite element method for domain decomposition with non-matching grids. *ESAIM: Mathematical Modelling and Numerical Analysis*, 37(2):209–225, Mar. 2003.

[10] J. Bergh and J. Löfström. *Interpolation Spaces: An Introduction*, volume 223 of *Grundlehren der mathematischen Wissenschaften*. Springer Berlin Heidelberg, Berlin, Heidelberg, 1976.

[11] J. Bezanson, A. Edelman, S. Karpinski, and V. B. Shah. Julia: A fresh approach to numerical computing. *SIAM review*, 59(1):65–98, 2017.

[12] D. Braess. Stability of saddle point problems with penalty. *ESAIM: Mathematical Modelling and Numerical Analysis*, 30(6):731–742, 1996.

[13] D. Braess. *Finite Elements: Theory, Fast Solvers, and Applications in Elasticity Theory.* Cambridge University Press, 2007.

[14] J. H. Bramble and J. T. King. A finite element method for interface problems in domains with smooth boundaries and interfaces. *Advances in Computational Mathematics*, 6(1):109–138, Dec. 1996.

[15] S. C. Brenner and L. R. Scott. *The Mathematical Theory of Finite Element Methods*, volume 15 of *Texts in Applied Mathematics.* Springer New York, New York, NY, 2008.

[16] E. Burman. Ghost penalty. *Comptes Rendus Mathematique*, 348(21-22):1217–1220, Nov. 2010.

[17] E. Burman. Projection stabilization of Lagrange multipliers for the imposition of constraints on interfaces and boundaries. *Numerical Methods for Partial Differential Equations*, 30(2):567–592, Nov. 2014.

[18] E. Burman, S. Claus, P. Hansbo, M. G. Larson, and A. Massing. CutFEM: Discretizing geometry and partial differential equations. *International Journal for Numerical Methods in Engineering*, 104(7):472–501, Dec. 2015.

[19] E. Burman and P. Hansbo. Fictitious domain finite element methods using cut elements: I. A stabilized Lagrange multiplier method. *Computer Methods in Applied Mechanics and Engineering*, 199(41-44):2680–2686, Oct. 2010.

[20] E. Burman and P. Hansbo. Fictitious domain methods using cut elements: III. A stabilized Nitsche method for Stokes' problem. *ESAIM: Mathematical Modelling and Numerical Analysis*, 48(3):859–874, May 2014.

[21] E. Burman, P. Hansbo, M. G. Larson, and A. Massing. Cut finite element methods for partial differential equations on embedded manifolds of arbitrary codimensions. *ESAIM: Mathematical Modelling and Numerical Analysis*, 52(6):2247–2282, Nov. 2018.

[22] P. Clément. Approximation by finite element functions using local regularization. *Revue française d'automatique, informatique, recherche opérationnelle. Analyse numérique*, 9(R2):77–84, 1975.

[23] A. A. Cuellar, C. M. Lloyd, P. F. Nielsen, D. P. Bullivant, D. P. Nickerson, and P. J. Hunter. An Overview of CellML 1.1, a Biological Model Description Language. *SIMULATION*, 79(12):740–747, Dec. 2003.

[24] A. J. Ellingsrud, A. Solbrå, G. T. Einevoll, G. Halnes, and M. E. Rognes. Finite Element Simulation of Ionic Electrodiffusion in Cellular Geometries. *Frontiers in Neuroinformatics*, 14:11, Mar. 2020.

[25] L. C. Evans. *Partial differential equations*, volume 19 of *Graduate Studies in Mathematics*. American Mathematical Society, Providence, RI, second edition, 2010.

[26] S. Farina, S. Claus, J. S. Hale, A. Skupin, and S. P. A. Bordas. A cut finite element method for spatially resolved energy metabolism models in complex neuro-cell morphologies with minimal remeshing. *Advanced Modeling and Simulation in Engineering Sciences*, 8(1):5, Dec. 2021.

[27] S. Farina, V. Voorsluijs, S. Claus, A. Skupin, and S. Bordas. A cutfem method for a mechanistic modelling of astrocytic metabolism in 3d physiological morphologies. The 8th European Congress on Computational Methods in Applied Sciences and Engineering, June 2022.

[28] R. FitzHugh. Impulses and Physiological States in Theoretical Models of Nerve Membrane. *Biophysical Journal*, 1(6):445–466, July 1961.

[29] T. Frachon, P. Hansbo, E. Nilsson, and S. Zahedi. A divergence preserving cut finite element method for Darcy flow, May 2022.

[30] P. C. Franzone and G. Savaré. Degenerate Evolution Systems Modeling the Cardiac Electric Field at Micro- and Macroscopic Level. In A. Lorenzi and B. Ruf, editors, *Evolution Equations, Semigroups and Functional Analysis*, pages 49–78. Birkhäuser Basel, Basel, 2002.

[31] C. Geuzaine and J.-F. Remacle. Gmsh: A 3-D finite element mesh generator with built-in pre- and post-processing facilities. *International Journal for Numerical Methods in Engineering*, 79(11):1309–1331, Sept. 2009.

[32] P. Grisvard. *Elliptic Problems in Nonsmooth Domains.* Society for Industrial and Applied Mathematics, 2011.

[33] C. Gürkan and A. Massing. A stabilized cut discontinuous Galerkin framework for elliptic boundary value and interface problems. *Computer Methods in Applied Mechanics and Engineering*, 348:466–499, May 2019.

[34] A. Hansbo, P. Hansbo, and M. G. Larson. A finite element method on composite grids based on Nitsche's method. *ESAIM: Mathematical Modelling and Numerical Analysis*, 37(3):495–514, May 2003.

[35] P. Hansbo. Nitsche's method for interface problems in computa-tional mechanics: Nitsche's method for interface problems in computa-tional mechanics. *GAMM-Mitteilungen*, 28(2):183–206, Nov. 2005.

[36] Helse- og omsorgsdepartementet. Nasjonal hjernehelsestrategi (2018–2024), 2017.

[37] A. L. Hodgkin and A. F. Huxley. A quantitative description of membrane current and its application to conduction and excitation in nerve. *The Journal of Physiology*, 117(4):500–544, Aug. 1952.

[38] K. H. Jæger, A. G. Edwards, W. R. Giles, and A. Tveito. Arrhythmogenic influence of mutations in a myocyte-based computational model of the pulmonary vein sleeve. *Nature Scientific Reports*, 12:7040, Apr. 2022.

[39] K. H. Jæger, A. G. Edwards, A. D. McCulloch, and A. Tveito. Properties of cardiac conduction in a cell-based computational model. *PLoS Computational Biology*, 15(e1007042), May 2019.

[40] K. H. Jæger and A. Tveito. Derivation of a cell-based mathematical model of excitable cells. In A. Tveito, K.-A. Mardal, and M. E. Rognes, editors, *Modeling Excitable Tissue: The EMI Framework*, volume 7, chapter 1, pages 1–13. Springer International Publishing, Cham, Oct. 2021.

[41] B. C. Jongbloets, S. Lemstra, R. Schellino, M. H. Broekhoven, J. Parkash, A. J. Hellemons, T. Mao, P. Giacobini, H. van Praag, S. D. Marchis, G. M. Ramakers, and R. J. Pasterkamp. Stage-specific functions of semaphorin7a during adult hippocampal neurogenesis rely on distinct receptors. *Nature Communications*, 8, Mar. 2017.

[42] M. Kuchta, K.-A. Mardal, and M. E. Rognes. Solving the EMI equations using finite element methods. In A. Tveito, K.-A. Mardal, and M. E. Rognes, editors, *Modeling Excitable Tissue: The EMI Framework*, page 56–69. Springer International Publishing, Cham, Oct. 2021.

[43] B. P. Lamichhane and B. I. Wohlmuth. Mortar Finite Elements for Interface Problems. *Computing*, 72(3-4), June 2004.

[44] A. Massing, M. Larson, A. Logg, and M. E. Rognes. A Nitsche-based cut finite element method for a fluid-structure interaction problem. *Communications in Applied Mathematics and Computational Science*, 10(2):97–120, Sept. 2015.

[45] H. Matano and Y. Mori. Global existence and uniqueness of a three-dimensional modelof cellular electrophysiology. *Discrete & Continuous Dynamical Systems - A*, 29(4):1573–1636, Oct. 2011.

[46] MICrONS Explorer. www.microns-explorer.org.

[47] A. Motta, M. Berning, K. M. Boergens, B. Staffler, M. Beining, S. Loomba, P. Hennig, H. Wissler, and M. Helmstaedter. Dense connectomic reconstruction in layer 4 of the somatosensory cortex. *Science*, 366(6469), Nov. 2019.

[48] K. Mörschel, M. Breit, and G. Queisser. Generating Neuron Geometries for Detailed Three-Dimensional Simulations Using AnaMorph. *Neuroinformatics*, 15(3):247–269, July 2017.

[49] J. C. C. Nitsche. Über ein variationsprinzip zur lösung von dirichlet-problemen bei verwendung von teilräumen, die keinen randbedingungen unterworfen sind. *Abhandlungen aus dem Mathematischen Seminar der Universität Hamburg*, 36:9–15, May 1971.

[50] A. Quarteroni. *Numerical Models for Differential Problems.* Springer Milan, Milano, 2014.

[51] J. A. Roĭtberg and Z. G. Šeftel'. A theorem on homeomorphisms for elliptic systems and its applications. *Mathematics of the USSR-Sbornik*, 7(3):439–465, Apr. 1969.

[52] B. Schott, U. Rasthofer, V. Gravemeier, and W. A. Wall. A face-oriented stabilized Nitsche-type extended variational multiscale method for incompressible two-phase flow. *International Journal for Numerical Methods in Engineering*, 104(7):721–748, Nov. 2015.

[53] L. R. Scott and S. Zhang. Finite Element Interpolation of Nonsmooth Functions Satisfying Boundary Conditions. *Mathematics of Computation*, 54(190):483–493, Apr. 1990.

[54] D. Sterratt, B. Graham, A. Gillies, and D. Willshaw. *Principles of Computational Modelling in Neuroscience.* Cambridge University Press, 2011.

[55] J. Sundnes, G. T. Lines, X. Cai, B. F. Nielsen, K.-A. Mardal, and A. Tveito. *Computing the Electrical Activity in the Heart.* Springer, Berlin Heidelberg, 2006.

[56] Thingiverse. Low poly deer head, 2013. https://www.thingiverse.com/thing:145237.

[57] V. Thomée. *Galerkin finite element methods for parabolic problems*, volume 25 of *Springer Series in Computational Mathematics.* Springer-Verlag, Berlin, second edi-

tion, 2006.

[58] L. Tung. *A bi-domain model for describing ischemic myocardial d-c potentials.* PhD thesis, Massachusetts Institute of Technology, Cambridge, MA, USA, 1978.

[59] N. L. Turner, T. Macrina, J. A. Bae, R. Yang, A. M. Wilson, C. Schneider-Mizell, K. Lee, R. Lu, J. Wu, A. L. Bodor, A. A. Bleckert, D. Brittain, E. Froudarakis, S. Dorkenwald, F. Collman, N. Kemnitz, D. Ih, W. M. Silversmith, J. Zung, A. Zlateski, I. Tartavull, S.-c. Yu, S. Popovych, S. Mu, W. Wong, C. S. Jordan, M. Castro, J. Buchanan, D. J. Bumbarger, M. Takeno, R. Torres, G. Mahalingam, L. Elabbady, Y. Li, E. Cobos, P. Zhou, S. Suckow, L. Becker, L. Paninski, F. Polleux, J. Reimer, A. S. Tolias, R. C. Reid, N. M. d. Costa, and H. S. Seung. Reconstruction of neocortex: Organelles, compartments, cells, circuits, and activity. *Cell*, 185(6):1082–1100, 2022.

[60] A. Tveito, K. H. Jæger, M. Kuchta, K.-A. Mardal, and M. E. Rognes. A cell-based framework for numerical modelling of electrical conduction in cardiac tissue. *Frontiers in Physics, Computational Physics*, 5, Oct. 2017.

[61] A. Tveito, K. H. Jæger, G. T. Lines, Ł. Paszkowski, J. Sundnes, A. G. Edwards, T. Mäki-Marttunen, G. Halnes, and G. T. Einevoll. An evaluation of the accuracy of classical models for computing the membrane potential and extracellular potential for neurons. *Frontiers in Computational Neuroscience*, 11:27, Apr. 2017.

[62] M. Veneroni. Reaction–diffusion systems for the microscopic cellular model of the cardiac electric field. *Mathematical Methods in the Applied Sciences*, 29(14):1631–1661, Apr. 2006.

Nanna Berre

Cut finite element methods for modeling excitable cells

NTNU
Norwegian University of
Science and Technology